

PRIP-TR-86

August 27, 2003

3D mosaicing of fractured surfaces

Martin Kampel

Abstract

A major obstacle to the wider use of 3D object reconstruction and modeling is the extent of manual intervention needed. Such interventions are currently massive and exist throughout every phase of a 3D reconstruction project: collection of images, image management, establishment of sensor position and image orientation, extracting the geometric detail describing an object, merging geometric, texture and semantic data.

This work aims to develop a solution for automated documentation of archaeological pottery, which also leads to a more complete 3D model out of multiple fragments. Generally the 3D reconstruction of arbitrary objects from their fragments can be regarded as a 3D puzzle. In order to solve it we identified the following main tasks: 3D data acquisition, orientation of the object, classification of the object and reconstruction.

3D acquisition with respect to archaeological requirements is described by four different methods, designed for the recording of fragments, complete vessels, profile sections and color. The range and pictorial information of the objects is the input for further classification and reconstruction. In the so-called documentation step the processing of the recorded data leads to orientation and the profile sections. The following classification step produces a systematic view and order of the material recorded and identifies possible candidates for subsequent fragment assembling. Reconstruction of pottery refers not only to the reconstruction of a pot from its fragments, but also to the reconstruction of a pot or fragment out of its profile section.

This thesis describes a complete system for automated documentation and reconstruction of archaeological pottery. The main contributions are 3D scanning of pottery, pairwise registration of views, a scheme for automatic classification of pottery, and an approach for solving 3D jigsaw puzzles of fragmented surfaces. In order to evaluate the system, experiments and results are given on both synthetic and real data. The selected approaches are cross-checked with the associated archaeologists.

Acknowledgments

This thesis would not have been possible without the guidance, advice and support of numerous people in our PRIP (Pattern Recognition and Image Processing) laboratory at the Vienna University of Technology. I particularly wish to thank:

- **Robert Sablatnig**, my thesis supervisor, who demonstrated to me what it means to work scientifically. His valuable suggestions and criticism have influenced this thesis to a large extent and made the completion of this work possible.
- **Hubert Mara** and **Srdan Tosovic**, for their hard work on our 3D scanner and their support on doing the experiments.
- **Katarina Schindler**, for many thorough suggestions regarding mathematical problems.
- Our Archaeologists, especially **Kristina Adler**, **Martin Penz** and **Raimund Kastler** for their advice and support. Thank you Kristina for convincing me that results -in addition to accuracy- have to be “nice”.
- **Allan Hanbury**, for carefully proof-reading this thesis.

Furthermore I would like to thank my colleagues for their contribution and good sense of humor providing an excellent working atmosphere: *Michael Reiter, Thomas Melzer, Horst Wildenauer, Paul Kammerer* and *Ernestine Zolda*.

During the writing of my thesis, I spent one month at the Computer Vision Laboratory, ETH-Zurich, Switzerland. I thank Luc van Gool for his support and the productive atmosphere.

I am grateful to several foundations and institutions for direct and indirect financial support of my studies: Austrian Science Foundation (FWF) under grant P13385-INF, the European Union under grant IST-1999-20273, the Austrian Federal Ministry of Education, Science and Culture and the innovative project “3D technology” of Vienna University of Technology.

Last, but not least, special thanks to **Brigitta** for her constant support during the time of writing the thesis and for “bearing up” with somebody who definitely spends too much time in front of a computer.

Contents

1	Introduction	1
1.1	Problem Statement	2
1.2	Motivating Application: Archaeology	3
1.3	Previous Work	8
1.4	Overview	12
2	Data Acquisition	15
2.1	Acquisition of Fragments	16
2.1.1	Two Laser Method	17
2.1.2	LCD-Projector	19
2.1.3	Minolta Vivid 900	20
2.1.4	ShapeCam Technology	21
2.1.5	Results and Accuracy	22
2.2	Acquisition of Complete Vessels	28
2.2.1	Acquisition	29
2.2.2	Modeling	29
2.2.3	Results and Accuracy	31
2.3	Color Acquisition	33
2.4	Chapter Summary	34
3	Data Processing for Fragments	36
3.1	Orientation	36
3.1.1	Determination of the Axis of Rotation	37
3.1.2	Determination of the Orifice Plane	43
3.2	Registration	45
3.3	Profile Generation	49
3.4	Results	52
3.5	Chapter Summary	57

4	Classification	58
4.1	Determination of Shape Characteristics	58
4.2	Curvature-based Segmentation	61
4.2.1	Cubic Splines	62
4.2.2	Interpolation by Cubic B-Splines	63
4.2.3	Approximation by Cubic B-Splines	65
4.3	Generation of Primitives	67
4.4	Results	69
4.5	Chapter Summary	74
5	Mosaicing	75
5.1	Determination of Description	77
5.2	Fragment Retrieval	80
5.3	Fragment Matching	84
5.4	Chapter Summary	88
6	Reconstruction Results	89
6.1	Reconstruction of Profiles	89
6.2	Reconstruction of Fragments out of their Profile	92
6.3	Reconstruction of Vessels out of Mutliple Fragments	95
6.3.1	Synthetic Data	95
6.3.2	Flowerpot	97
6.3.3	Archaeological Fragments	99
6.4	Archaeological Point of View	103
6.5	Chapter Summary	104
7	Conclusion and Outlook	105
7.1	Feasibility of the Approach	105
7.2	Thesis Summary	107
7.3	Future Work	107
	Bibliography	109

Chapter 1

Introduction

*I know these pieces fit cuz I watched them falling away
mildewed and smoldering, Fundamental differing.*

Tool, Schism

Archaeology is at a point where it can benefit greatly from the application of computer vision methods, and in turn provides a large number of new, challenging and interesting conceptual problems and data for computer vision [82]. In particular, a major obstacle to the wider use of 3D object reconstruction and modeling is the extent of manual intervention needed. Such interventions are currently massive and exist throughout every phase of a 3D reconstruction project: collection of images, image management, establishment of sensor position and image orientation, extracting the geometric detail describing an object, and merging geometric, texture and semantic data. Improvements in rangefinder technology, together with algorithms for combining and processing 3D data allow us to accurately digitize the shape and surface characteristics of physical objects.

Every archaeological excavation must deal with a vast number of ceramic fragments. The documentation of archaeological findings is a problem, that could benefit greatly from computerized assistance, because the process of documentation and classification can be carried out by computerized methods in both a faster and a more objective way [118].

We begin this chapter by defining a set of subproblems within the greater framework of computer vision and archaeology. Then we give the archae-

ological background, followed by a discussion of relevant work that most influenced the research described in this thesis. The chapter concludes with an overview of the thesis.

1.1 Problem Statement

The problems specifically addressed in this thesis are:

- How can we acquire 3D data of small artifacts found on archaeological excavations using a camera and structured light?

With the help of 3D data, the profile (a cross section in the three dimensional model) of the fragment is constructed. The profile serves as a basis for any subsequent classification and reconstruction.

- How can we accurately express recorded data in a single object centered coordinate system?

In order to compute a complete 3D model of an object two or more views of an object from a scene, in our case the front and the back view of the fragment have to be aligned. By using the 3D model archaeologists are able to perform 3D measurements on the surface of the objects interactively.

- How can we manipulate the surface description so that it better approximates the input data in order to allow robust classification?

The purpose of classification is to get a systematic view of the material found [89], to recognize types, and is used to relate a fragment to existing parts in the archive.

- How can we solve the 3D jigsaw puzzle of putting fragmented surfaces together?

Reassembly of fragmented objects from a collection of thousands randomly mixed fragments is a problem that arises in several applied disciplines, such as archaeology, failure analysis, paleontology, art conservation, and so on. Solving such jigsaw puzzles by hand may require

years of tedious and delicate work, consequently the need for computer aided methods is obvious [73].

- How can we speed up the archival- and documentation process in archaeology? How can we decrease the amount of human intervention needed for 3D scanning of small artifacts?

At excavations a large number (up to 80.000) of ceramic fragments are found. These fragments are photographed, measured, drawn (called *documentation*) and classified. Up to now documentation and classification have been done manually which means a lot of routine work for archaeologists and a very inconsistent representation of the real object [113].

- How can we improve the benefit of using computer vision methods applied to archaeology?

Recent advances in rangefinder technology, together with algorithms for combining and processing 3D data allow us to propose new strategies to archaeology and in turn archaeology provides a large number of new, challenging and interesting conceptual problems and data for computer vision [82].

- How can we make documentation in archaeology more objective?

Whereas the results of the conventional documentation by different archaeologists may differ [90], this system should serve the archaeologist as a powerful tool for reducing the amount of routine work and for getting an objective, reproducible acquisition of the material.

In order to clarify the problem statement from an archaeological point of view the next section describes the archaeological background of the thesis.

1.2 Motivating Application: Archaeology

Ceramics are one of the most widespread archaeological finds and are a short-lived material. This property helps researchers to document changes of style

and ornaments. Therefore, ceramics are used to distinguish between chronological and ethnic groups. Furthermore, ceramics are used in economic history to show trading routes and cultural relationships [90]. In particular ceramic vessels, where shape and decoration are exposed to constantly changing fashion, not only allow a basis for dating the archaeological strata, but also provide evidence of local production and trade relations of a community as well as the consumer behavior of the local population [90].

The documentation, administration and scientific processing of these fragments represents a temporal, personnel and financial problem [19]. Various excavation projects have been completed many years ago, but due to these problems their findings have yet to be published (see [38]). Scientific evaluation in archaeological practice often suffers due to extensive amounts of time required for the documentation and classification of ceramic finds [90]. Many publications do little more than present the drawings, descriptions and determinations of the objects found [118]. Thus it is frequently the case that several hundred pages of catalogs and illustrations are accompanied by only a few pages of analysis [25].



Figure 1.1: Boxes filled with ceramics stored in archives.

Figure 1.1 shows boxes filled with ceramics stored in an archive. If one

asks archaeologists what they use pottery for (or why excavated fragments of pottery are kept) they will probably reply 'for dating evidence'. This dating evidence furthermore splits into three different types of evidence that is obtained from excavated pottery or its fragments [90]:

- Dating
- Distribution relating to trade
- Function and/or status

These are based on the fact that every pot was made or used at a certain time, made at a certain place, and used for a certain purpose. Therefore, every fragment or pot holds the information about when, where, and what it was made for. This fact places a heavy burden on excavators and primary processors or recorders of the material since the primary task of pottery research is comparison [90]. This means that pottery must be grouped and recorded in a way that facilitates a comparison.

The recording of fragments consists of:

1. Photographing
2. Measuring
3. Drawing
4. Grouping

Up to now all this has been done manually which means a lot of routine work for archaeologists and a very inconsistent representation of the real object [90]. First, there may be errors in the measuring process, diameter or height may be inaccurate, second, the drawing of the fragment should be in a consistent style, which is not possible since a drawing of an object without interpreting it is very hard to do. The third process, grouping or classifying, is also a very difficult task. There have been several attempts to develop a reliable method of classification [11, 94, 25, 16, 1, 117], none of which is widely accepted. A graphic documentation done by hand additionally

raises the possibility of errors. This leads to a lack of objectivity in the documentation of the material found. To give an example, a vessel was drawn by four different illustrators resulting in four different vessels as shown in Figure 1.2. Note the different shape and decoration, the rim and the thickness for instance are significantly different.

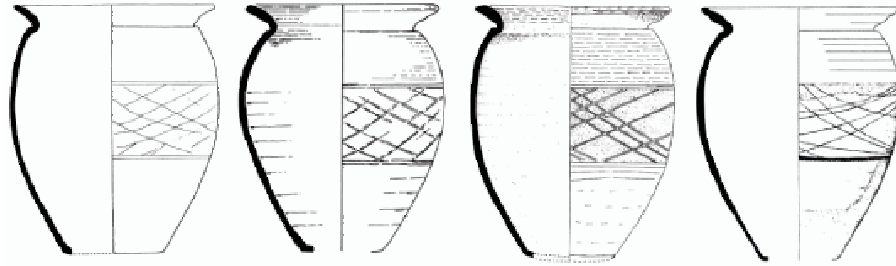


Figure 1.2: The limits of objective recording: The same vessel drawn by four different illustrators (from [90]).

At excavations most of the finds are in form of fragments, with only a few are still complete. It would be ideal to have one acquisition system that covers both sorts of objects, however, they do have different properties like dimensions, color, and geometry. Furthermore, the acquisition time for fragments has to be short, for complete vessels, since they are rare, the acquisition time is not critical but the output should be accurate in all dimensions.

A very important property of archaeological pottery is color [90]. Archaeologists determine the specific color of a fragment by matching it to the Munsell color patches [86, 131]. Since this process is done "manually" by different archaeologists and under varying light conditions, the results differ from each other. In general, photos of fragments are taken in order to have color representations in the archive. Due to different camera characteristics and changing light conditions the color of a fragment in images varies. Archaeologists need digital color images of fragments for archivation purposes, thus the color information which is normally achieved with a color measurement instrument can be gained directly from the digital image for each pixel in the entire image.

Traditional archaeological classification and reconstruction is based on the so-called profile of the object, which is the cross-section of the fragment in the

direction of the rotational axis of symmetry. This two-dimensional plot holds all the information needed to perform archaeological research. The correct profile and the correct axis of rotation are thus essential to reconstruct and classify archaeological ceramics. Figure 1.3 shows the inner side of a fragment on the left and its left side (broken surface) on the middle, and the profile section on the right (Figure 2.7d shows the same fragment drawn by hand).

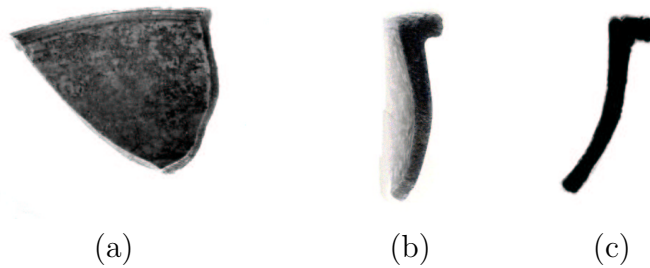


Figure 1.3: (a) Archaeological fragment (b) site of fracture (c) profile section.

The purpose of classification is to get a systematic view of the material found (if every piece would be treated as unique, this would immediately lead to the wood-for-the-trees syndrome due to the vast amount of information), to recognize types, and to add labels for additional information as a measure of quantity. In order to standardize the classification, which is based on the fragment's structure, it can be divided into two main parts, shape features and properties. The *classification of shape* defines the process by which archaeologists distinguish between various features such as the profile and the dimensions of the object like diameter and type of surface, whereas the *classification of material* copes with different characteristics of a fragment like the clay, color and surface properties.

Archaeological classification is traditionally done by typology [30]: defined forms are identified to possess certain significance and then addressed as "types". These "types" can be used as a sort of "label", which simplifies comparative studies and communication within the scientific field [101, 1, 117, 9, 23]. The drawing in Figure 1.4 for instance is a repre-

sentative for many other examples. Furthermore, with the recognition of vessel types, chronological, topographical, etc. patterns can be recognized. Hence, classification provides the basis for statistical analysis.

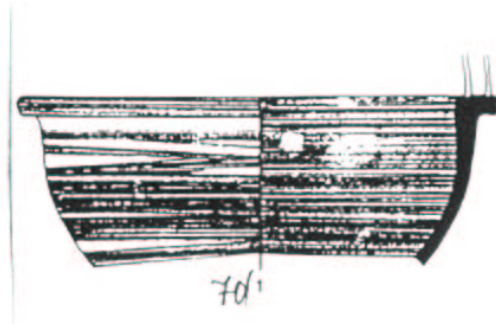


Figure 1.4: Drawing of a complete pot (from [65]).

Archaeologists often leave their typologies at an "impressionistic" or indefinite level, because their main task is to present new material. There have been many attempts to objectify and standardize shape description and classification - also in connection with systems for automated recording [61, 119, 96] - , but in practical archaeological research most of the consequent formal and mathematical classification schemes did not find a wider reception or application because they are often too vague, abstract, reductionistic or inpracticable [90].

1.3 Previous Work

The documentation of archaeological finds is a problem that could benefit greatly from computerized assistance, because the process of documentation and classification can be carried out by computerized methods in both a faster and a more exact way [118]. The search for possible solutions began early [31, 75, 119, 63, 128, 32]. More recently, improvements in rangefinder technology, together with algorithms for combining and processing 3D data allow us to accurately digitize the shape and surface characteristics of many physical objects. Three larger projects are selected and illustrated which

thereby should represent further ongoing initiatives:

Within *The Digital Michelangelo Project* [28], M. Levoy and his group from Stanford University describe a hardware and software system for image acquisition, segmentation, reconstruction and visualization of large fragile objects. The goal of the project is to produce a set of 3D models (statue, architectural settings, fragments) to create a long-term digital archive of important cultural artifacts. They digitized 10 statues by Michelangelo (largest dataset contains 2 billion polygons and 7000 color images), two building interiors, and all 1,163 fragments of the Forma Urbis Romae, a giant marble map of Rome. The challenge of the project was the size of the datasets, which made the invention of new methods for representing, aligning, merging and viewing necessary. K. Pulli describes in his Ph.D. thesis [99] the methods used for post-processing this data. The integration of these large datasets into a surface model is estimated by a robust hierarchical space carving method [100].

Putting together the fragments of the Forma Urbis Romae is one of the great unsolved problems of archaeology. The Stanford Group is currently assembling the pieces to create 3D models of each map fragment and solving the map with 3D matching based on features like thickness, marble veining, straight borders or clamp holes. A further goal is a web-accessible relational database giving description and bibliographic information about each fragment [43].

The *SHAPE Project* [27] from Brown University is an interdisciplinary effort for scientific research in the analysis of archaeological finds and artifacts. In particular they are concerned with the assembly or reconstruction of pottery vessels from a collection of fragments. The fragments in this collection may come from one or more vessel whose design and construction are not known. The goal is to develop methods for completing the process in an efficient and automatic fashion. Cooper et. al. [14] present an approach to a largely automated estimation of polynomial models in order to assemble virtual pots from 3D measurements of their fragments. The estimation of mathematical models for matching of fragments is based on matching break-

curves, which are curves on a pot surface separating fragments. Fragment matching based on a Bayesian approach using break curves, estimated axis and profile curves is presented in [26]. Kong et. al. [67] try to solve the jigsaw problem in two stages: first, potsherds are joined automatically in two dimensions by using an efficient joint detection algorithm. Next in finding a global solution, ambiguous results from local shape matching are resolved and the pieces are merged together.

The Canadian *National Research Council (CNRC) laboratory* has developed 3D digitizing and modeling technologies since 1981. Their main objective is the integration of technologies for the development of a 3D digitizing system in order to allow the monitoring of precise dimensional (geometry) and photometric (color) information over time and its visualization. Within the digital Michelangelo Project NRC's high resolution scanner was used to provide images of several areas on different sculptures which represent a variety of tool marks, surface finishes and types of marble for the project [102]. Two projects have been undertaken to demonstrate a system for rapid response to remote heritage recording applications [7]: the goal of the 'Biris in Padova' project was to digitize a sculpture, bas reliefs and deteriorating architectural elements and the goal of the 'Biris in Ferrara' project was to digitize building elements of the 8th century. Further projects dealt with 3D imaging of paintings [5], remote access to museums [123] and large view laser scanners [102].

The *3D MURALE Project* [108, 15] contributes to new developments in recording, cataloging, conserving, restoring and presenting archaeological artifacts, monuments and sites. It focuses on two aspects: firstly putting new technologies in the hands of the archaeologists themselves rather than creating multimedia content after the excavations, and secondly, presenting the site not as a static entity from a long-gone past, but as a vibrant place that underwent a lot of changes throughout its existence. A first goal of the project is to register in situ all stratigraphical evidence (an archaeological site is excavated layer by layer so-called stratas resulting in a sequence of strata), as archaeological fieldwork by its nature destroys this kind of in-

formation. The 3D recording techniques replace present techniques of 2D recording which offer only a piecemeal representation and are both time consuming and labor intensive. Secondly, techniques are developed to build 3D models of artifacts, mainly for cataloging and visualization, and of sculptures and buildings, mainly for restoration and visualization. Thirdly, the terrain of the site is modeled in 3D as such topographic data yield important information for the archaeologists and is vital for a realistic visualization. Finally, an integrated model is built of the landscape, the buildings, and the artifacts, this being done for different eras, showing reconstructions for these periods or the current state. Recording and reconstruction of small artifacts are of major concern of our group at the Vienna University of Technology in the ongoing project. Engaged results comprise the recording of complete vessels in respect to archaeological needs and the virtual reconstruction of complete objects out of fragments [SM96].

Motivated by the current requirements of archaeological research our group develops an automated archival system for archaeological fragments [56]. Within the project *Bildhafte Keramikerfassung* (P09954-SPR) [110] a computer based acquisition system for archaeological fragments was developed. This prototype carries out an automated object surface acquisition with respect to archaeological requirements [48]. The following project *Computer Aided Classification of Ceramics* (P13385-INF) [2, 54] describes a system for automatic classification and reconstruction of archaeological fragments. With the help of this system and the knowledge of an expert an automated classification of archaeological finds is achieved [53]. It is intended to develop both an objective classification tool and an objective classification standard that fulfill defined classification criteria with specific emphasis on the classification possibility of object types not known a-priori.

Further descriptions of related work to each subtopic can be found in Chapters 2, 3, 4 and 5.

1.4 Overview

This thesis presents a complete system for scanning and reconstructing pottery found in archaeological excavations. The main goal is to find

1. a solution for automatic documentation of archaeological pottery, which leads to
2. a complete 3D model of a vessel out of multiple fragments.

Here is a summary of the contributions in this thesis:

- We have constructed a 3D scanning device for pottery with hardly any human intervention needed. The main innovations are automatic orientation of fragments and fully automatic recording of complex shapes.
- We have developed a method for pairwise registration of two views based on a model-based approach.
- We have developed a classification scheme for automatic classification of pottery.
- We have developed a macro geometric approach for solving 3D jigsaw puzzles of fragmented surfaces. It is based on the profile sections of the pottery.

The chapters in this thesis are written as a sequence of stages that represent the workflow of the approach. Figure 1.5 summarizes the workflow of the thesis, giving an overview of the technical research aims. Using the acquired data of a fragment, the data is processed in order to compute its profile section. With the help of this profile, measurements like volume, area, percentage of complete vessel, height, width and so on are computed automatically. Next a mosaicing process tries to find different fragments belonging to the same vessel based on attributes stored in the archive database. After the segmentation and classification of the profile of the fragment, the profile can be used to reconstruct the complete vessel which leads to a virtual 3D Model of the original vessel.

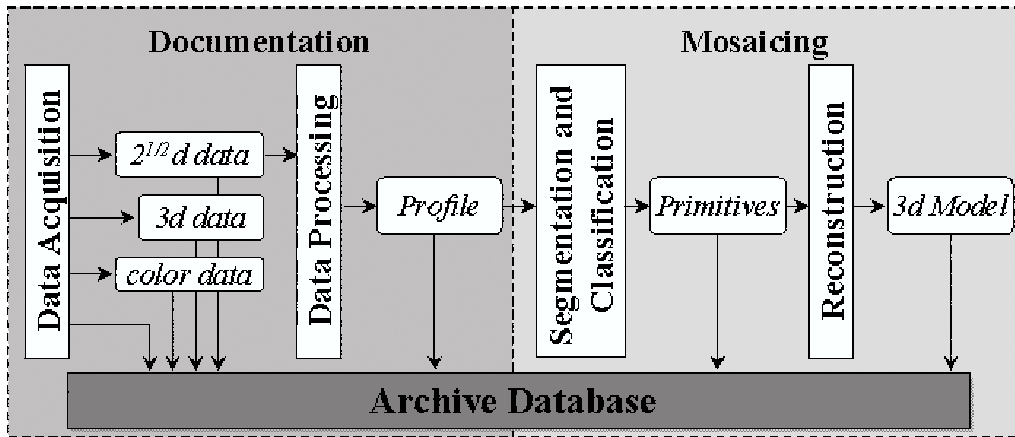


Figure 1.5: Workflow of the thesis.

In the introductory chapter the motivation and the contributions of the thesis were described. It discussed the archaeological background by presenting the manual archivation of pottery. In order to present ongoing initiatives in the field of 'Computer Aided Archaeology' three larger projects were described. In Chapter 2 3D data acquisition with respect to archaeological requirements is outlined. Four different methods, designed for the recording of fragments, complete vessels, profile sections and color are described. Prototype systems as well as commercially available 3D scanners are presented. This chapter is intended for readers who are not familiar with the general concepts of 3D scanners based on structured light. Chapter 3 addresses the processing of the recorded fragment data in order to compute their profile sections. Algorithms for finding the orientation of a fragment, aligning two views of a fragment and the computation of the profile section are presented. Chapters 2 and 3 describe the so-called documentation step, which is followed by the classification step. An approach for automatic classification of pottery based on profile sections is presented in Chapter 4. A curvature based segmentation technique is described in order to identify characteristic pottery types like plate, bowl, etc. This chapter is intended for readers who are mostly interested in the applied classification strategy. The reconstruction out of classified fragments is described in Chapter 5. A concept for the comparison of pottery shapes is outlined and an algorithm for finding matching

pairs of candidate fragments is introduced. Reconstruction results for profiles, fragments and pots on synthetic and real data are shown in Chapter 6. Finally Chapter 7 concludes this thesis and gives an outlook on future research. Each chapter starts with a brief introduction and is concluded with a short summary. Results are shown at the end of each chapter.

Chapter 2

Data Acquisition

Data acquisition is the first and the most important task in a chain of 3D reconstruction tasks, because the data quality influences the quality of the final results [8]. El. Hakim specifies in [24] the quality of the data by a number of requirements: high geometric accuracy, capturing all details, photo-realism, full automation, low cost, portability, flexibility in applications, and efficiency in model size. It would be ideal to have one single acquisition system that satisfies all requirements, but this is still the future. F. Blais gives in [12] an overview on state of the art of range scanners by describing the last 20 years on range sensor development. The order of importance of the requirements depends on the application, for example cost is a major concern in the field of archaeology.

For the acquisition of archaeological pottery we identified the following four applications:

- **Profile acquisition** [45, 46]. The goal is to provide data in real time for the manual classification done by archaeologists.
- **Fragment acquisition** [48, 51]: Computation of a range image of two views of a fragment. The data acquired is used for the documentation and archival of the fragment, thus it is the data to be assembled into one object.
- **Recording of complete objects** [111, 58]: Data is used as virtual representation of the real object.

- **Color acquisition** [50, 49]: On the one hand the data is used as texture of the fragments recorded, on the other hand it serves as an attribute for the automatic classification of the finds.

This chapter describes a selection of acquisition devices designed or adapted to facilitate the recording of pottery. It is organized as follows: In Section 2.1 we describe the recording of fragments. The four devices presented meet the requirements of the task in different ways. Since we focus on the processing of fragments, a method for the acquisition of complete vessels is briefly described in Section 2.2. Furthermore the estimation of accurate color information is shown in Section 2.3. Each section concludes with results and shows the accuracy of the approach. A chapter summary is given at the end of this chapter.

2.1 Acquisition of Fragments

The acquisition method for estimating the 3D shape of a fragment is *Shape from structured light* (SfSL) [20], which is based on active triangulation [10]. SfSL is a method which constructs a surface model of an object based on projecting a sequence of well defined light patterns onto the object. The patterns can be in the form of coded light stripes [44] or a ray or plane of laser light [74]. For every pattern an image of the scene is taken. This image, together with the knowledge about the pattern and its relative position to the camera are used to calculate the coordinates of points belonging to the surface of the object. In the process of calibration the parameters to describe the position of the sensors in a reference co-ordinate system and the sensor characteristics of the camera are estimated [44]. If the geometry between the light plane and the image is known, then each 2D image point belonging to the laser line corresponds to exactly one 3D point on the surface of the object [66, 114]. This process is also called *active triangulation* [10, 20], illustrated in Figure 2.1.

The volume of the fragments to be processed ranges from $3 \times 3 \times 3cm^3$ to $30 \times 30 \times 50cm^3$.

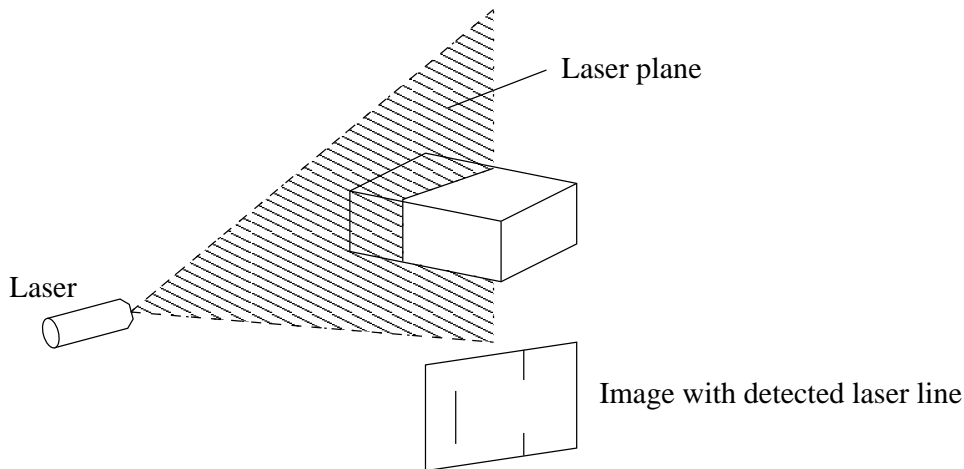


Figure 2.1: Active triangulation.

2.1.1 Two Laser Method

In order to generate a profile section in real time we use a two laser technique resulting in a two dimensional image of the profile [79]. The acquisition system consists of the following devices:

- two monochrome CCD-cameras with a focal length of $16mm$ and a resolution of 768×576 pixels.
- two red lasers with a wavelength of $670nm$ and a power of $10mW$. The lasers are equipped with a prism in order to span a plane out of the laser beam.

The acquisition system is illustrated schematically in Figure 2.2: Laser 1 and laser 2 are mounted in one plane on both sides of the fragments, so that camera 1 takes the picture of the laser-plane projected on the outer side (Figure 2.3a) and camera 2 on the inner side of the sherd as seen in Figure 2.3b. These images are combined manually, so that a profile line containing the inner and outer profile is generated. The resulting image is filtered by an adaptive threshold that separates the background from the laser. Afterwards the laser line is thinned, so that a profile line - similar to the lines drawn by hand from archaeologists - is extracted [79].

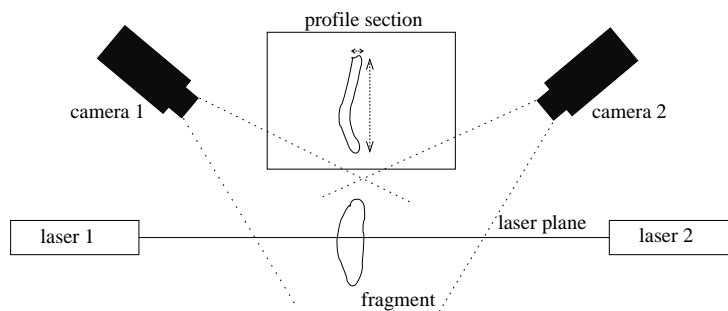


Figure 2.2: Profile section using two lasers.

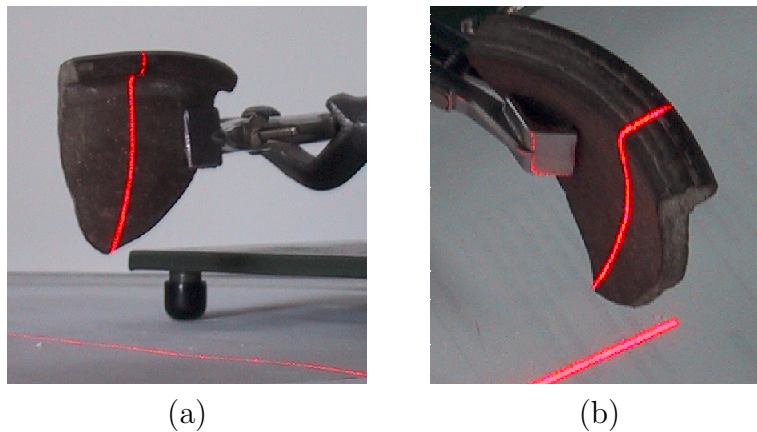


Figure 2.3: 2D-acquisition with two lasers and two cameras: (a) Camera 1 acquires laserline 1, (b) Camera 2 acquires laserline 2.

The method has some drawbacks for using it in an automated system:

1. The sherd has to be oriented manually, because no axis of orientation can be estimated from the recorded data.
2. The diameter of the whole object has to be determined manually.
3. The position of the fragment, laser and camera in the acquisition system has to be selected, so that there are a minimum of occlusion effects of the laser plane and that the longest profile line is recorded.

2.1.2 LCD-Projector

In order to overcome the limits from the two laser method, a system for the automated acquisition of the profile line was developed. The acquisition system consists of the following devices:

- one monochrome CCD-camera with a focal length of $16mm$ and a resolution of 768×576 pixels.
- a Liquid Crystal Display (LCD640) projector¹).

Figure 2.4 illustrates the acquisition system. The LCD projector is mounted at the top in order to illuminate the whole acquisition area. The angles between the optical axis of the LCD projector and the camera are chosen to minimize camera and light occlusions (approximately 20°).

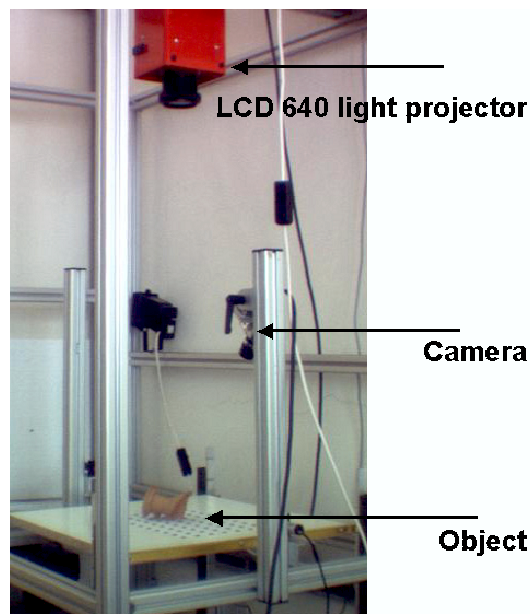


Figure 2.4: Acquisition System.

The projector projects stripe patterns onto the surface of the objects. In order to distinguish between stripes they are binary coded [66]. The camera

¹ABW GMBH, Siemenstrasse 3, D-72636 Frickenhausen, Germany, www.abw-3d.de.

grabs gray level images of the distorted light patterns at different times. The image obtained is a 2D array of depth values and is called a range image [66].

Fragments of vessels are thin objects, therefore 3D data of the edges of fragments are not accurate, and this data cannot be acquired without placing and fixing the fragment manually which is time consuming and therefore not practicable. Ideally, the fragment is placed in the measurement area, a range image is computed, the fragment is turned and again a range image is computed. This step consists of sensing the front and backsides of the object (in our case a rotationally symmetric fragment) using the calibrated 3D acquisition system. The resulting range images are used to estimate the axes of rotation, in order to reconstruct the fragment.

There is no manual orientation of the fragment necessary, because it is computed automatically (see Section 3.1). Since this acquisition system is not portable and therefore not usable outside the laboratory, we used the “Minolta Vivid 900” Technology, presented in the next section for recording fragments outside.

2.1.3 Minolta Vivid 900

The *Vivid 900* 3D Scanner developed by MINOLTA²) in our setup consists of the following devices:

- one CCD-camera with a focal length of $14mm$ and a resolution of 640×480 pixels, equipped with a rotary filter for color separation.
- one red laser with a wavelength of $670nm$ and a maximal power of $30mW$. The laser is equipped with a galvanometer mirror in order to open loop control the laser beam scanning motion.

Figure 2.5 illustrates the acquisition setup consisting of the Vivid 900 Scanner connected to a PC and the object to be recorded. Optionally the object is placed on a turntable with a diameter of $40cm$, whose desired position can be specified with an accuracy of 0.1° . The 3D Scanner works on the principle of laser triangulation combined with a colour CCD image. It

²MINOLTA Austria GMBH, Amalienstrasse 59-61, 1131 Vienna, Austria, www.minoltaeuropa.com.

is based on a laser-stripe but a galvanometer mirror is used to scan the line over the object.



Figure 2.5: The Minolta VIVID 900 scanner.

Vivid 900 is a portable device, that does not require a host computer. The optional rotating table is used to index the scanned part and capture all sides in one automated process. Due to its weight (11kg) and size ($213 \times 413 \times 271mm^3$) it cannot be used as handheld device which complicates the acquisition process on the excavation site. In order to record fragments on site, we therefore used the “ShapeCam” Technology, presented in the next section.

2.1.4 ShapeCam Technology

The *ShapeCam Technology* developed by Eyetronics³) consists of the following devices:

- a Sony TVR-900E digital camera
- a Leica slide projector

³Eyetronics HQ, Kapeldreef 60, 3001 Heverlee, Belgium, www.eyetronics.com.

Figure 2.6 illustrates the ShapeCam: a digital camera and a specially designed flash device are mounted on a lightweight frame. The flash device projects a predefined grid or pattern onto an object or a scene which is viewed by a camera from a (slightly) different point of view. The camera also grabs the texture information which can be mapped on the resulting 3D geometry of the object.

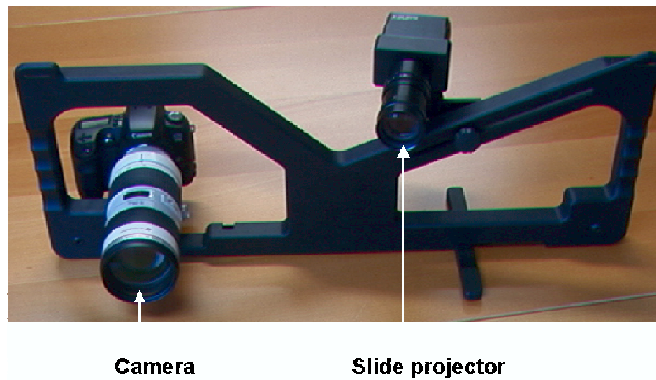


Figure 2.6: Eyetronic’s ShapeCam.

The ShapeCam technology is a commercially available technique that allows the generation of 3D models based on the use of a single image taken by an ordinary camera.

As this system is a handheld device, the shapes can be recorded in situ. Within the 3D MURALE project we carried out on site tests to capture 3D pot sherds and other finds from the excavation site in Sagalassos [15]. The ShapeCam hardware has been adapted to facilitate such work.

2.1.5 Results and Accuracy

In order to demonstrate the output of the presented acquisition systems, examples for each method are given below. Acquisition speed and accuracy of each system are compared to each other at the end of this section. The range accuracy describes the measurement uncertainty along the depth axis, i.e. Z axis. It is estimated by comparing measurements of known objects

with measurements of the recorded object: the average deviation along the Z axis gives the range accuracy.

- Two lasers

Five examples are given (see Figure 2.7 to Figure 2.11) in order to show the applicability of the approach. Each figure contains the data acquired (a), the thinned profile and final presentation of the profile section (c). In order to visually compare the computer aided results with the manual results, a manual drawing of the same fragment is given (d).

The results achieved visually correspond to the manual drawing of the fragment, showing the feasibility of the approach. Since the images are combined and orientated manually, the precision of the final profile section depends on the resolution of the camera and on the experience of the user [85], consequently the results are not objective. The profile is acquired in real time, because acquisition takes only the time necessary to grab an image. Experiments have shown that the actual speed for the acquisition of a profile section by an experienced archaeologist lies between 10 and 30 seconds, because time is spent for the manual orientation of the fragment.

- LCD projector

Applying the non portable acquisition system, two views of 40 fragments from the late Roman burnished ware of Carnuntum [33] have been recorded. The data was mainly used for testing the classification tasks, because these fragments have been available in the laboratory, which has simplified the evaluation of the automatic classification. Non of these fragments belongs to the same vessel. See Figure 2.12 for two resulting range images of one fragment. The front view contains 37176 points and the back view contains 31298 points.

Experiments on the acquisition device are thoroughly described in [44]. Range accuracy is specified between 0.68mm to 1mm. Most of the acquisition time (5sec; ± 0.5 sec) is needed for the projection of the

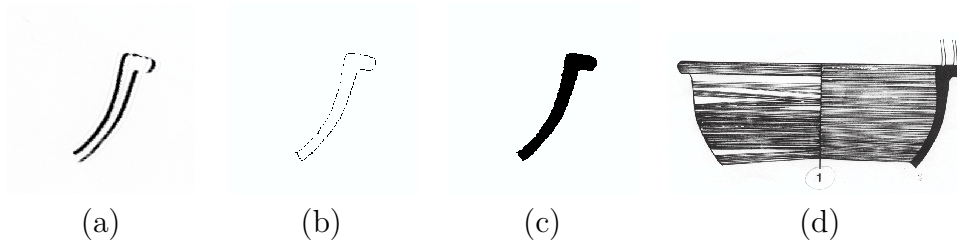


Figure 2.7: Profile acquisition of fragment 70-1.

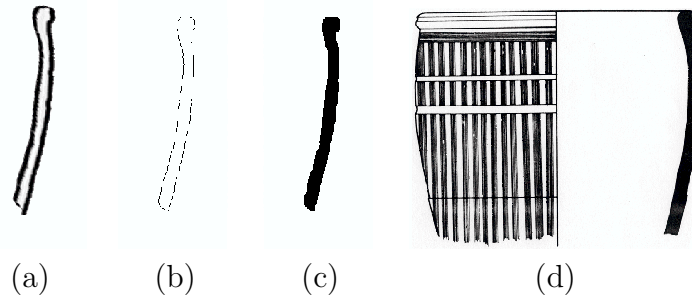


Figure 2.8: Profile acquisition of fragment 78-2.

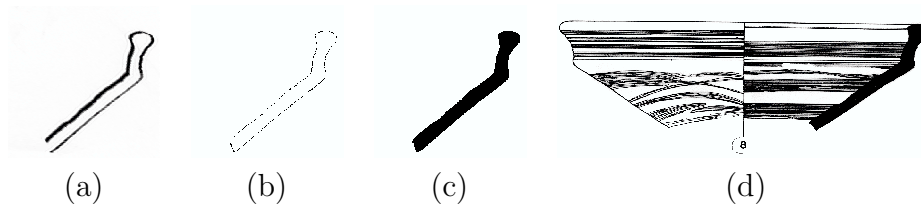


Figure 2.9: Profile acquisition of fragment 72-8.

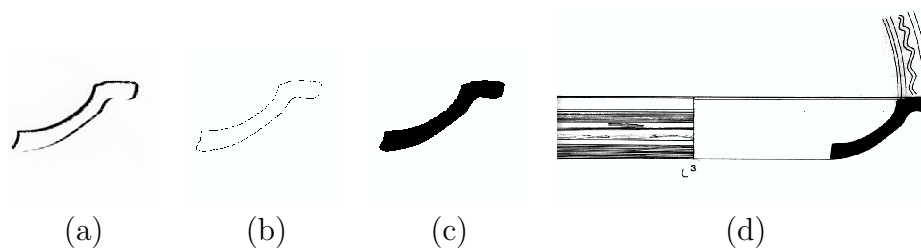


Figure 2.10: Profile acquisition of fragment 75-3.

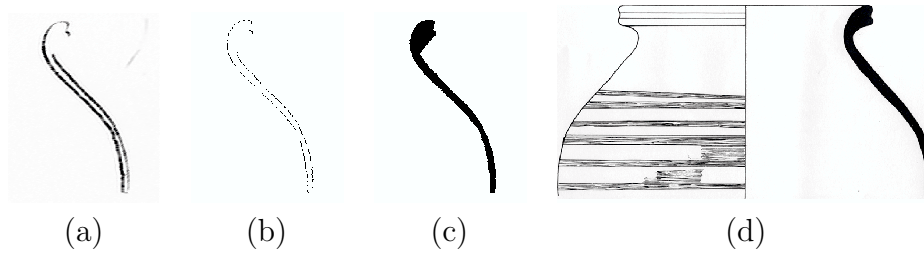


Figure 2.11: Profile acquisition of fragment 81-1.

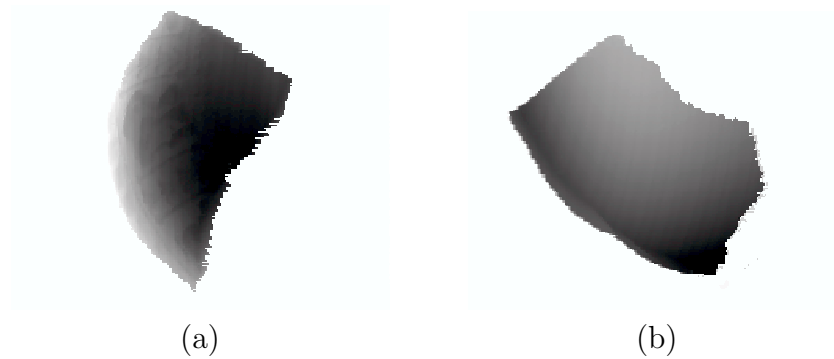


Figure 2.12: Range Image of two views of a fragment, (a) front view (b) back view.

light patterns. Total acquisition time is around 5.5 sec (± 0.5 sec) on a Pentium 233MMX with 256 MB RAM using non-optimized code.

- Minolta VIVID 900

Using the VIVID 900 we have recorded 2 to 15 views of 10 archaeological fragments. The number of data points ranges from 3.000 to 150.000 points. Figure 2.13 shows a decorated fragment with 17781 points and 33981 triangles. The acquisition time depends on the number of range points (size of the object), for 150.000 points it is approximately 1.5 sec. The achieved range accuracy lies between 0.2mm and 0.7mm.

- ShapeCam Technology

Using the ShapeCam Technology we have recorded four different boxes of sherds from the common wares of Sagalassos [19]. Table 2.1 gives an

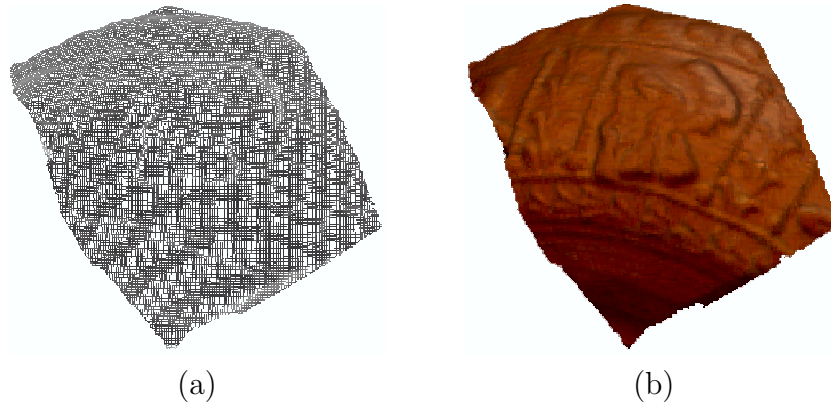


Figure 2.13: (a) Wireframe representation and (b) textured representation of a fragment using the VIVID 900.

overview of the data collected. These fragments serve as test material for assembling a complete vessel. Box1 and Box2 contain fragments from different vessels, whereas some fragments of Box3 and Box4 are from one and the same vessel. Knowing that fragments belong together will simplify the evaluation of the assembly. Two views from each fragment have been recorded, except for Box4 multiple views have been taken. The views of the fragments of Box4 have been registered manually. The pottery dataset contains 70 pieces in total.

	BOX 1	BOX 2	BOX 3	BOX 4
Nr. of fragments	21	12	28	9
Format	VRML 2	VRML 2	VRML 1	VRML 2
Nr. of views	2	2	2	multiple
Nr. of vertices	3000 – 9000	4000 – 9000	3000 – 8000	15000 – 80000
Preregistered	No	No	No	Yes

Table 2.1: Pottery dataset.

Figure 2.14a shows the wire frame model of the recorded front view (a) containing 3538 points with 6774 triangles and (b) shows the same view with its texture.

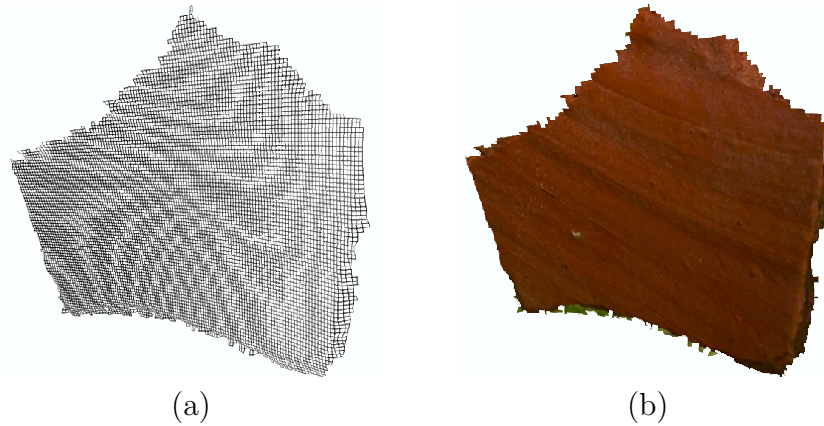


Figure 2.14: (a) Wire frame representation of the front view (b) and a textured representation of fragment 18 box 1.

The range accuracy lies between 0.7mm to 1mm which matches the specification of the manufacturer. The acquisition time depends on the number of range points (size of the object), for 30.000 points it is approximately 2sec.

- Comparison of the systems

In order to compare the acquisition systems presented Table 2.2 summarizes the results. For each technique the type of the computed results, the underlying measuring method, the precision in terms of range accuracy, portability and acquisition speed is given. The result of the two laser method is a 2D plot of the profile line, consequently no range accuracy is given. The most accurate and fastest system is the VIVID 900, but it is also the most expensive one which makes it difficult to use at archaeological excavations. The advantage of the ShapeCam is its portability, efficiency in model size and flexibility in applications. The use of LCD projector which is not a portable system allows full automation from the acquisition until the reconstruction.

Device	output	Measuring Method	Precision [mm]	portable	Speed	Cost
Two Laser	2D Profile Line	Laser Scanner	–	No	real time	Prototype
LCD	Range Image	Pattern projection	0.65 – 1	No	50.000 pts in 5.5sec	10.000EUR
Shape-Cam	3D-Geometry	Pattern projection	0.7 – 1	Yes	30.000 pts in 2sec	20.000EUR
Vivid-900	3D-Geometry	Laser Triangulation	0.2 – 0.7	Yes	150.000 pts in 1.5sec	50.000EUR

Table 2.2: Comparison of the acquisition devices used.

2.2 Acquisition of Complete Vessels

For complete objects we use a combination of the *Shape from Silhouette* (SfS) method [125] with the SfSL method. The output of both algorithms is then used to construct a single 3D model.

SfS is a method for automatic construction of a 3D model of an object based on a sequence of images of the object taken from multiple views, in which the object’s silhouette represents the only interesting feature of the image [121, 97]. The object’s silhouette in each input image corresponds to a conic volume in the object real-world space. A 3D model of the object can be built by intersecting the conic volumes from all views, which is also called *Space Carving* [69]. SfS can be applied on objects of arbitrary shapes, including objects with certain concavities (like a handle of a cup), as long as the concavities are visible from at least one input view. This condition is very hard to hold since most of the archaeological vessels do have concavities. To discover these concavities we use SfSL. Images for both algorithms are acquired by rotating the object on a turntable in front of a stationary camera. Then an octree representation [125] of the object is built incrementally, by performing limited processing of all input images for each level of the octree. Beginning from the root node a rough model of the object is obtained quickly and is refined as the processed level of the octree increases. The method is described in full detail in [124].

2.2.1 Acquisition

The acquisition system (Figure 2.15) consists of the following devices:

- a turntable (Figure 2.15a) with a diameter of 50cm , whose desired position can be specified with an accuracy of 0.05° . The turntable is used to obtain multiple views of the object observed.
- two monochrome CCD-cameras (Figure 2.15b and 2.15c) with a focal length of 16 mm and a resolution of 768×576 pixels. One camera (*Camera-1* in Figure 2.15) is used for acquiring the images of the object's silhouettes and the other one (*Camera-2* in Figure 2.15) for the acquisition of the images of the laser light projected onto the object.
- a red laser (Figure 2.15d) used to project a light plane onto the object. The laser is equipped with a prism in order to span a plane out of the laser beam.
- a lamp (Figure 2.15e) used to illuminate the scene for the acquisition of the silhouette of the object. The object should be clearly distinguishable from the background independent of the object's shape or the type of its surface. For that reason back-lighting [37] is used. A large (approx. $50 \times 40\text{cm}^2$) rectangular lamp is placed behind the turntable (as seen from the camera).

The size of objects to be processed ranges from $10 \times 10 \times 20\text{cm}^3$ to $40 \times 40 \times 50\text{cm}^3$. Prior to any acquisition, the system is calibrated in order to determine the inner and outer orientation of the camera and the rotational axis of the turntable. The calibration method used was exclusively developed for the SfS algorithm presented and is described in detail in [59].

2.2.2 Modeling

Our approach builds a 3D model of an object by performing the following steps [60]: First, both of the input images (SfS and SfSL) are binarized so that the black image pixels *possibly* belong to the object and the white pixels *undoubtedly* belong to the background. Then, the initial octree containing

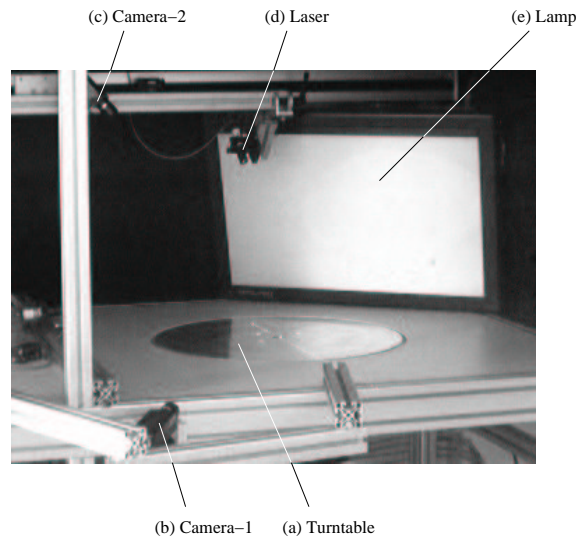


Figure 2.15: Acquisition system for complete objects.

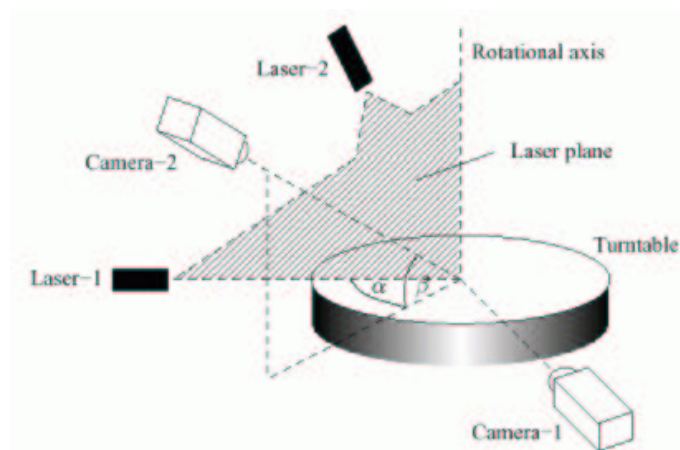


Figure 2.16: Geometrical setup of acquisition system.

one single root node marked "black" is built. Black nodes are subsequently checked by projecting the nodes into all SfS binarized input images and intersecting them with the image silhouettes of the object. As the result of the intersection the node can remain "black" (if it lies within the object) or be set to "white" (it lies outside the object) or "grey" (it lies partly within and partly outside the object). If the resulting node is not white, it is projected

into the binarized SfSL image representing the nearest laser plane to the node and again intersected. All grey nodes are divided into 8 child nodes all of which are marked "black" and the intersection test is performed in each of the black nodes. This subdivision of grey nodes is done until there are no grey nodes left or a subdivision is not possible (voxel size), which results in the final model.

2.2.3 Results and Accuracy

The reconstruction of complete vessels was tested on synthetic and real objects: For tests with synthetic objects we can build a model of a virtual camera and create input images which fit perfectly into the camera model. In a test we built models using 360 views with the constant angle of 1° between two views, while increasing octree resolution. It turned out that the SfS method performed best with an octree resolution of 128^3 , where the approximation error was $+0.83\%$ of the actual volume. In the second test we built models with constant octree resolution of 256^3 and an increasing number of views. The models computed are shown in Figure 2.17. It turned out that the use of 20 views instead of 360 views was sufficient to create models which differed by less than 1% from the models built using 360 views.

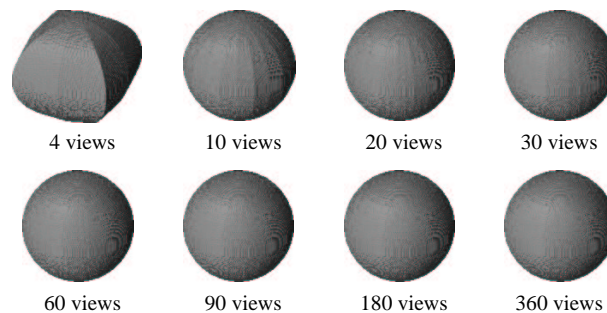


Figure 2.17: 3D models of a synthetic sphere with an increasing number of views.

For tests with real objects we used 5 objects: a metal cuboid, a wooden cone, a coffee mug, and two archaeological vessels. The cuboid and the cone have known dimensions so we can calculate their volumes analytically and compare them with the volumes of their reconstructed models. Using

these two objects we can also measure the impact of ignoring camera lens distortion on the accuracy of the models. All models shown in this section are built using 360 views, with a constant angle of 1° between two neighboring views. Table 2.3 summarizes the results. The resulting models, shown from three views, are depicted in Figure 2.18. All models are built with an octree resolution of 256^3 and using 360 views.

<i>object</i>	<i>voxel size</i>	<i>measured dimensions (mm)</i>	<i>volume(mm³)</i>	<i>calculated dimensions (mm)</i>
cuboid	-	$100.0 \times 70 \times 60$	384 678 (-8.41%)	$101 \times 71 \times 60$
cone	-	$156.0 \times 156 \times 78$	435 180 (-12.43%)	$150.1 \times 149.4 \times 77.5$
vessel #1	0.74 mm	$141.2 \times 84.8 \times 93.7$	336 131	$139.2 \times 83.2 \times 91.4$
vessel #2	0.53 mm	$114.2 \times 114.6 \times 87.4$	263 696	$113.0 \times 111.9 \times 86.4$
cup	0.66 mm	$113.3 \times 80.0 \times 98.9$	276 440	$111.6 \times 79.0 \times 98.3$

Table 2.3: Reconstruction of cuboid, cone, two vessels, and a cup.

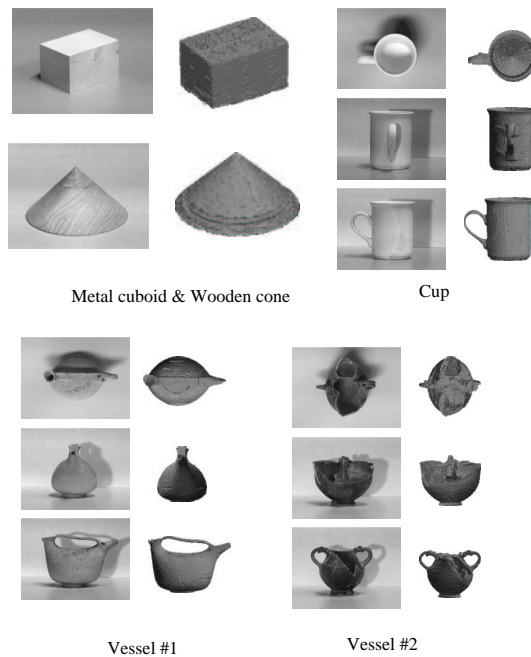


Figure 2.18: 3D models of cuboid, cone, two vessels, and a cup

2.3 Color Acquisition

In order to allow automated color estimation we use a solution to color constancy assuming that the spectral reflectance [78] of archaeological fragments varies slowly in the visible spectrum [50]. Our approach is based upon R. Lee’s method and assumes that spectral illumination is known [71]. This means that small changes of RGB values should lead to small changes in reflectance. Prior knowledge about the illuminant leads to chromaticity and luminance information. The algorithm is described in detail in [49] and [50]. The following experiments show the feasibility of the approach.

Two experiments are presented: the first example with MacBeth Colors [84] and the second with real fragments. In the first experiment we use the measured reflectance of 12 MacBeth color patches as reference and try to estimate the reflectance of the other 12 patches using the reference set. The resulting reflectance is compared to previous measured values.

The computed reflectances of the 12 color patches correlated between 0,85 and 0,98 to their corresponding measured reflectances with an average correlation of 0,92 (see Table 2.4). Lower correlation may be caused by the purely statistical representation of the underlying variables by the characteristic vector analysis [116].

patchnr	corr	patchnr	corr
1	0.98	7	0.97
2	0.97	8	0.95
3	0.93	9	0.96
4	0.98	10	0.91
5	0.86	11	0.85
6	0.92	12	0.89

Table 2.4: Correlation between measured and calculated spectral reflectances of 12 Macbeth ColorChecker patches.

In the second experiment we grab an image of a fragment and specify two test regions A and B (Figure 2.19a). The reference set was chosen from the MacBeth color checker. The spectral reflectances of A and B are computed

and visualized in Figure 2.19b. For evaluation purposes we calculate CIE tristimulus values using a linear transformation and compare the achieved values with measured chromaticity coordinates from a Chroma Meter CR-200b.

Table 2.5 shows a comparison between measured and computed chromaticity coordinates. The final results are in the close neighborhood of the measured values which shows that the method correctly determines color values.

	Comp. A	Meas. A	Comp. B	Meas.B
x	0.48	0.33	0.49	0.40
y	0.39	0.34	0.41	0.37
Y	17.9	11.1	32.3	21.0

Table 2.5: Measured and computed chromaticity coordinates.

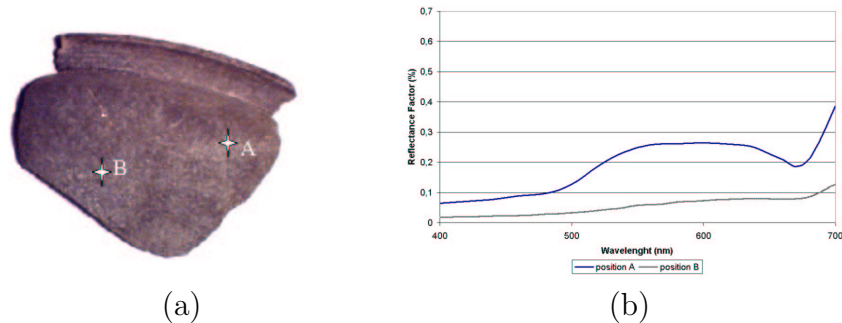


Figure 2.19: (a) Test regions A and B and (b) calculated spectral reflectance of positions A and B.

2.4 Chapter Summary

In this chapter a selection of acquisition devices which meet the requirements of pottery acquisition has been described. The setup of each acquisition system and its technical principles were shown. We differentiated between fragment acquisition in Section 2.1 and complete vessel acquisition in Section 2.2. Furthermore in Section 2.3 an approach for accurate color estimation

was presented. Results of the methods described show the accuracy and applicability of the selected approaches.

Chapter 3

Data Processing for Fragments

The range and pictorial information of a fragment provided by the acquisition system is the basis for the further classification and reconstruction process. In order to automate this process, the profile has to be determined in the same way as in the manual documentation. First the orientation of the fragment has to be estimated, which is described in Section 3.1. With the help of the 2.5D-range images [81] achieved from the acquisition system, a 3D object model has to be constructed in order to determine the profile. We developed a model-based approach, which performs the registration of the two surfaces of one fragment. The approach is presented in Section 3.2. The generation of the profile is shown in Section 3.3. The chapter concludes with results of each section.

3.1 Orientation

The term *orientation* describes the exact position of a fragment on the original vessel. Finding the proper orientation of a fragment is one of the main tasks of the archaeological classification process [90]. The basis for classification and reconstruction is the profile, which is the cross-section of the fragment in the direction of the rotational axis of symmetry. Hence the position of a fragment (orientation) on a vessel is important.

The manual process of making pottery with the potter's wheel is primarily based on the rotation of the potter's wheel and the forming through the potters own hands. The newly formed pot is built up vertically around

the axis of rotation. The upper part of the vessel, which is called the rim, terminates in the so called orifice plane. Based on the orifice plane the archaeologist first orientates the rim sherd according to its former position on the original vessel. If the fragment shows a section of the rim, the simplest way of manually establishing its orientation is by placing it upside down i.e. with the rim on a horizontal surface (see Figure 3.1).



Figure 3.1: Archaeological approach for finding the correct orientation of a rim fragment.

Next, the measured height of the orientated rim-sherd is used for drawing the sherd in its original position. Archaeologists use a horizontal surface like a ruler or a table etc. to orientate the fragment by aligning the fragment with the plane: they look for the position where a minimum gap exists between the plane of the rim fragment and the chosen horizontal plane. The gap is clearly shown by the amount of light coming through. Once the point of greatest resemblance is found, the height of the sherds is measured.

In order to find the correct orientation automatically we developed an approach for finding the axis of rotation of the fragment, which is described in Section 3.1.1. Additionally, we followed the archaeological approach and estimated the orientation by computing the orifice plane of the fragment, which is explained in Section 3.1.2.

3.1.1 Determination of the Axis of Rotation

The basis for this axis estimation is a dense range image provided by the range sensor. The estimation approach exploits the fact, that surface normals of rotationally symmetric objects intersect their axis of rotation. If we have an

object of revolution (like an archaeological vessel made on a rotation plate) we can suppose that all intersections of the surface normals n_i are positioned along the axis of symmetry R , which is schematically shown in Figure 3.2.

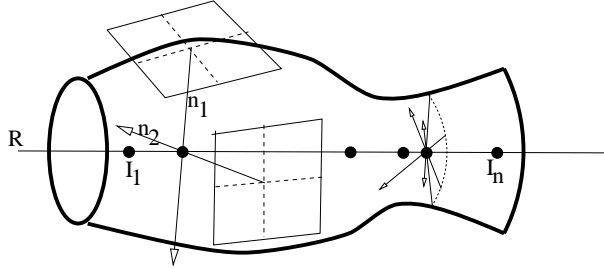


Figure 3.2: Axis determination using Hough-Space.

This assumption holds [35] for a complete object or even for its fragment. We try to extract a surface of revolution where the curvature of the surface is relatively small. A few approaches to extract volumetric shape descriptors of solids of revolution out of dense range images are reported in Yokoya and Levine [134] and a Hough-based approach to the problem is presented. The Hough transform is a robust and efficient tool for feature extraction [103, 39]. It is based on a voting principle: each point or element will vote for the set of features to which it could belong. This voting principle makes the Hough transform very robust toward noise or outliers [4]. Yokoya and Levine [134] use the center of the principal curvature from first and second partial derivatives of the surface, which construct the so-called focal surface (see [133]). Since our surfaces have a relatively small curvature we adopted this method by using a robust way for the determination of the surface normals, based on planar patches.

We consider a planar patch of size $s \times s$. The patch is fitted according to the following equation:

$$ax + by + cz + d = 0 . \quad (3.1)$$

This defines a planar patch with normal $\vec{\mathbf{n}} = (a, b, c)$. The fitting algorithm used is the Total Least Squares (TLS). Let $\mathbf{X} = \{ \mathbf{X}_1, \dots, \mathbf{X}_N \}$, where

$\mathbf{X}_i = (x_i, y_i, z_i)$. The TLS minimizes the following expression

$$E_n = \sum_{i=1}^N r_i^2, \text{ where } r_i = \frac{|ax_i + by_i + cz_i + d|}{\sqrt{a^2 + b^2 + c^2}}. \quad (3.2)$$

It was shown that this approach is equivalent to the MCA or Minor Component Analysis [132]: $\min_{\vec{\mathbf{n}}} E_n \equiv \mathbf{A} \cdot \vec{\mathbf{n}} = \lambda_{\min} \vec{\mathbf{n}}$, where \mathbf{A} is the covariance matrix of set \mathbf{X} and λ_{\min} is the smallest eigenvalue. The constant d is determined by

$$d = -\vec{\mathbf{n}} \cdot \frac{1}{N} \sum_{i=1}^N \mathbf{X}_i. \quad (3.3)$$

The main goal is to minimize the distances between the points of the surface and the planar patch. An iteratively re-weighted algorithm is used to compute the optimal value of the normal and to discard outliers. The objective of the algorithm is to achieve:

$$\Delta = \min_{\vec{\mathbf{n}}} \sum_{i=1}^{s^2} [ax_i + by_i + cz_i + d]^2. \quad (3.4)$$

In order to minimize the function, we use an iterative scheme. The points are weighted according to their residual [42], a point M_i at iteration k and with residual r_i has a weight ω_k defined by:

$$\omega_k = \begin{cases} 1 & \text{if } r_i \leq Sa \\ 0 & \text{otherwise} \end{cases} \quad (3.5)$$

where S is the Median Absolute Deviation and a is a tuning constant. The algorithm can be outlined with the initial state $k = 0$, $\omega_0 = [1\dots 1]$ as follows:

1. compute the surface normal $\vec{\mathbf{n}}_k$ using weights w_k .
2. compute the residuals r_i with the estimated parameters.
3. compute ω_{k+1} based on r_i .
4. iterate steps 1., 2., and 3 until convergence.

The algorithm uses all data points in the initial step, since it is assumed that there are only a few outliers in the data and the number of data-points within the patch is relatively low (around 20). If these conditions do not

hold this produces an incorrect surface normal that is eliminated by the subsequent axis determination.

Once the surface normals for all points are computed the rotation axis R can be estimated. For each point on the object, the surface normals $\vec{\mathbf{n}}_k$ are computed using Minor Component Analysis. In order to determine the axis of rotation R all surface normals $\vec{\mathbf{n}}_k$ are clustered in a 3D Hough-space: All the points belonging to a line $\vec{\mathbf{n}}_k$ are incremented in the accumulator. Hence the points belonging to a large number of lines (like the points along the axis) will have high counter values. All the points in the accumulator with a high counter value are defined as maxima. These maxima form the axis of rotation.

The accumulator maxima are taken as candidate points for the estimation of the rotation axis. For the set of points $\text{acc}(x, y, z)$ a Principal Component Analysis (PCA) [88] is used to find the optimal axis going through these set of points \mathcal{M} with

$$\mathcal{M} = \{P_i(x, y, z) | g_i = \text{acc}(x, y, z) > T_{acc}\} , \quad (3.6)$$

with

$$T_{acc} = s * \max(\text{acc}), \quad (3.7)$$

where T_{acc} defines a threshold accepting points in the accumulator. In order to estimate the axis the vector $\vec{\mathbf{v}}$ is determined by $\mathbf{A}\vec{\mathbf{v}} = \lambda_{max}\vec{\mathbf{v}}$, where \mathbf{A} is the covariance matrix of set \mathcal{M} and λ_{max} is the largest eigenvalue of \mathbf{A} .

A point \mathbf{G} on the axis is determined by using all points in \mathcal{M} with

$$G_{\mathcal{M}} = \frac{\sum_{i \in \mathcal{M}} \tilde{g}_i \mathbf{P}_i}{\sum_{i \in \mathcal{M}} \tilde{g}_i}, \text{ where } \tilde{g}_i = \begin{cases} g_i & d_i \leq T_d \\ 0 & \text{otherwise} \end{cases} \quad (3.8)$$

and the threshold $T_d = aS$. With the point \mathbf{G} and the vector $\vec{\mathbf{v}}$ the rotation axis is defined. Using this axis a robust version of the complete algorithm can be outlined by iteratively refining the position of the rotation axis. The sets \mathcal{I}_k and \mathcal{O}_k are respectively the inlier and outlier sets and the method starts with the initial condition $k=0$, $\mathcal{I}_k = \mathcal{M}$ and $\mathcal{O}_k = \{\}$.

1. compute surface normals $\vec{\mathbf{n}}$ for all points of the object.

2. cluster lines \mathcal{L}_i in $\text{acc}(x, y, z)$.
3. compute $\vec{\mathbf{v}}_k$ and $\mathbf{G}_{\mathcal{I}_k}$ using set \mathcal{I}_k .
4. determine the distances d_i of set \mathcal{M} to the axis defined by $\mathbf{G}_{\mathcal{I}_k}$ and $\vec{\mathbf{v}}_k$.
5. update $\mathcal{O}_{k+1}, \mathcal{I}_{k+1} = \mathcal{M} - \mathcal{O}_{k+1}$.
6. iterate steps 3., 4. and 5. until convergence or a maximum number of iterations is reached.

Using this technique, outliers introduced by noisy range data, due to bad calibration or discretization errors, can be avoided, since in the Hough-Space incorrect data points are in the minority and do not build a maximum. To evaluate this, synthetic range images are used where the axis of rotation is known and the images are disturbed by non symmetric object parts. Since there are some threshold parameters, the effect of changing these parameters was also taken into consideration.

The size of s of the planar patches depends on the geometry of the object and the accuracy of the range sensor: the more noise expected, the larger s should be to eliminate the outliers. However, since we are considering curved surfaces, s is also influenced by the minimal curvature we want to estimate in relation to the sensor resolution. In our tests using different sizes, it was shown to work best with $s = 5$, which ensures that there are at least 20 range points within the patch. The tuning constant was set to $a = 1$ (and therefore not used) and the threshold $T_{acc} = 0.7$ in all of the experiments. Both parameters were determined empirically based on our test data. The parameter space of the Hough space was set to $400 \times 400 \times 800$, which corresponds to the range image size of 400×400 and the maximal possible diameter of the fragment. The computation time depends on the number of range points (size of the object) and varies between 5 min and 15 min on a Pentium 233MMX with 256 MB RAM using non-optimized code.

In order to determine the error of the axis computation, the Mean Square Error (MSE) between the original and the computed axis is determined. The MSE is computed for all points of the axis inside the test object. The

MSE of all distances between the estimated and correct axis define the error. In Figure 3.3 test objects are visualized, where the estimated axis of rotation is drawn into the range image. For each test image the MSE is given according to the position of the original axis. It is instructive to compare our method to simple least square solutions, for which one incorrect surface normal which is sufficiently far away from the bulk of data can ruin the estimation completely. It can be shown that using our method, the axis can be determined even if there are large regions in the range image which are not rotationally symmetric, as can be seen in Figure 3.3b. In our tests we found out that on the average 15% of the surface normals were incorrect, which did not (or only slightly) influence the accuracy of the axis determination, since these normals were eliminated by the Hough method.

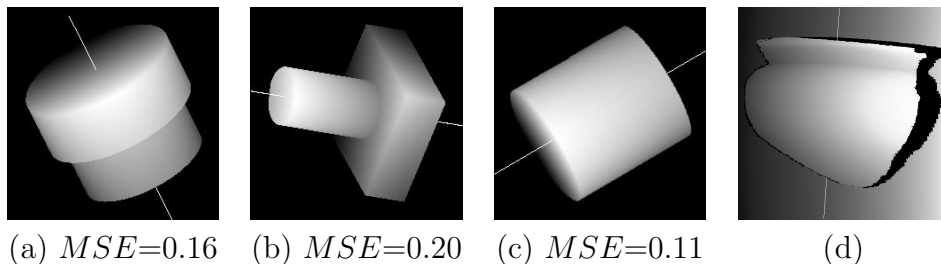


Figure 3.3: Axis determination for synthetic and real range data.

Problems that arise with real data are symmetry constraints, i.e. if the surface of the fragment is too flat or too small, the computation of the rotational axis is ambiguous (worst case: sphere) resulting in sparse clusters in the Hough-space, which indicate that the rotational axis is not determinable. Therefore, before we start our registration algorithm we first compute the Gaussian curvature for 20% of randomly selected surface points of one surface (back side, since there are usually no decorations on it). We determine whether the curvature is large enough to estimate the rotational axis, i.e. we look at curves determined by the intersection between the surfaces and planes perpendicular to the tangent plane at each surface point. All these curves have a single and well defined curvature at the point. The maximum and minimum of the normal curvature κ_1 and κ_2 at a given point on a surface are called the principal curvatures. The principal curvatures measure

the maximum and minimum bending of a regular surface at each point. The Gaussian curvature K and mean curvature H are related to κ_1 and κ_2 by: $K = \kappa_1 * \kappa_2$ and $H = 1/2(\kappa_1 + \kappa_2)$. We introduce two thresholds - a lower and an upper - to evaluate the results of the axis determination. If the average mean curvature of all selected surface points is below a lower threshold (0.2) the process is not started and the fragment is marked as incomputable. If it is above the lower threshold and below the upper threshold (0.8) it is marked as computable with a confidence weight, and if it is above the threshold it is again very unlikely to get good results since the surface is sphere - like (which is almost never the case in our test data). For both non-computing cases, other registration strategies have to be used, for flat fragments the surfaces are registered assuming that they are completely flat and should match to one another, for sphere-like fragments no registration is performed since these fragments do not hold any relevant archaeological information (they are not orientable manually either). Figure 3.3d shows the result for a front view of a fragment with the estimated rotational axis (black regions in Figure 3.3d indicate points where no range information is available due to occlusion).

3.1.2 Determination of the Orifice Plane

The determination of the orifice plane, on one hand, defines rim-fragments, which are the most important fragments for classification and reconstruction [90] (like the border pieces from a puzzle). On the other hand, due to the fact that the plane is orthogonal to the axis, it serves as additional information in the case of ambiguous computation of the curvature (i.e. the principal curvature is not uniquely determinable, see Section 3.1.1): the axis, which is orthogonal to the orifice plane is chosen. Furthermore it defines the top of a rim-fragment: the side fitting to the orifice plane is defined as top of the fragment.

Pottman et. al [98] describe the detection of planar faces reduced to the detection of point clusters on the Gaussian sphere. They improve the approach by using the Euclidian distance to detect point clusters. Kanazawa and Kanatani present in [62] a numerical scheme called renormalization for optimally fitting a planar surface to data points. Besides the optimal fit of

a planar surface, its reliability is automatically evaluated.

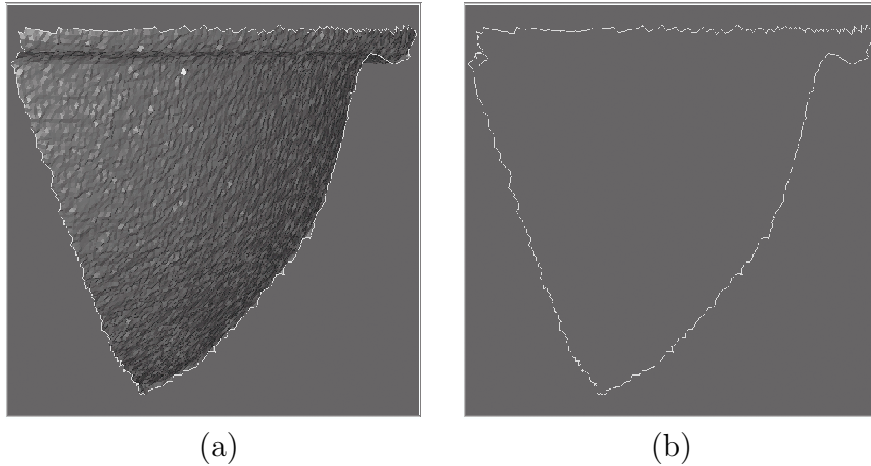


Figure 3.4: Projection of a fragment onto yz -plane: (a) Outline and triangles of the fragment, (b) Outline of the fragment.

We consider the problem in two dimensions, by projecting the outline of the orientated fragment onto the yz -plane (see Figure 3.4). Next we find the lines in the 2D point data using an Eigenspace approach based on the work of Leonardis et al. [120]. The algorithm can be outlined as follows:

1. First the axis of rotation is transformed into the z -axis of the coordinate system in order to simplify further computation.
2. The fragment's height is described as the difference between the maximum z -value and the minimum z -value of the fragment point data. Initialization of the plane E_{Ori_f} in the xz -plane of the coordinate system on the max. z -position.
3. The fragment is projected into yz -plane and the outline is computed.
4. Two random points of the outline are selected and a line is defined.
5. All points of the outline are investigated to determine, whether they lie on the line. If a point lies on the line, it supports the line and a counter is increased.

6. The next two points on the outline are chosen, the distance to the previous is typically around 30-40 points. Again a line is defined and the support is computed.
7. The previous step is continued until the whole outline has been processed.
8. The line, with maximal support is chosen for the estimation of the orifice plane.

Figure 3.5 shows the fragment (a) and the outline of the fragment together with its orifice plane.

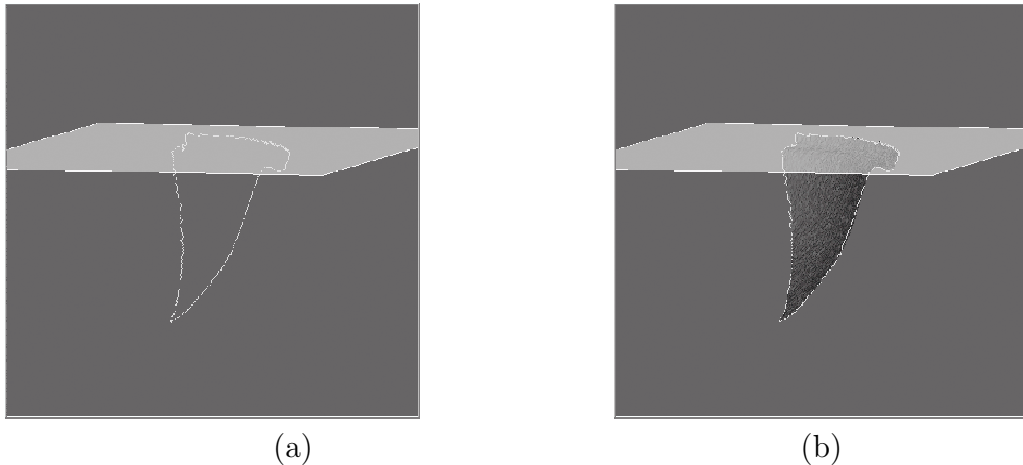


Figure 3.5: 3D View of (a) the outline and (b) the triangles of a fragment together with the orifice plane.

3.2 Registration

The task of building full 3D models of general objects is difficult, since there is no a-priori knowledge about the shape of the object. A simple method is to use a calibrated turntable upon which the camera is fixed, as described in [122]. Even though the turntable method described above is good at creating 3D models, there is still the problem of acquiring the bottom of the object sitting on the turntable. Hence the bottom and the top of the object needs

to be scanned in and then registered. In the case of thin ceramic fragments, the rotation table method does not solve the registration problem since one view of the fragment is always invisible (one solution would be to "glue" the fragment onto the plate in an upright position, however, this method is impractical and unthinkable for archaeologists [125]).

Fragments of vessels are thin objects, therefore 3D data of the edges of fragments are not accurate and this data cannot be acquired without placing and fixing the fragment manually. Ideally, the fragment is placed in the measurement area, a range image is computed, the fragment is turned and again a range image is computed. To perform the registration of the two surfaces, we use a-priori information about fragments belonging to a complete vessel: both surfaces have the same axis of rotation since they belong to the same object. Furthermore, the distance of the inner surface to the axis of rotation is smaller than the distance of the outer surface. Finally, both surfaces should have approximately the same profile; i.e. the thickness of the fragment measured on a plane perpendicular to the rotational axis should be constant on average. Note that this is only the case if the profile is taken perpendicular to the axis since this is induced by the manufacturing process. This condition holds for almost all fragments with the exception of relief decorated fragments. Still, the average distance perpendicular to the rotational axis is constant on most of the parts of the fragments since there are more undecorated than decorated parts. Therefore, this assumption is used to perform the "fine registration".

The most commonly used algorithm for registering is the Iterative Closest Point (ICP) algorithm [76]. ICP iteratively improves the registration of two overlapping surfaces by calculating the unique transformation that minimizes the mean square distances of the correspondences between the two surfaces. The algorithm starts with the selection of some point sets in one or both surfaces (which generally are triangulated surfaces), matches these point sets to one another, which gives a set of corresponding pairs, and weights the corresponding pairs. A rejection rule for pairs is applied to all pairs to determine outliers. To measure the fit, an error metric is used, which is minimized iteratively.

There are many different variants of the ICP Algorithm (see [106] for a

review) all based on local point correspondences. Therefore, it is very important to have a good rough alignment of the surfaces to be registered. Algorithms that do not use single pair of surface registration (no pre-alignment) are also called *global registration* algorithms (see [100], [22], or [130] for details).

Since we have a-priori knowledge about our surfaces and the rotational axis estimation we decided to use a computationally relatively inexpensive model-based approach [109, 47]. No point to point correspondences are required to determine the interframe transformation needed to express the points from each view in a common reference coordinate system [127]. We register the range images by calculating the axis of rotation of each view (Figure 3.6a and Figure 3.6b) and by bringing the resulting axes into alignment (Figure 3.6c). Knowing the surface normals of all surface patches we transform them into a common reference coordinate system. The first rough alignment is performed by aligning the two surfaces vertically. To do so we select the 10 uppermost points of each surface (we take the uppermost points since rim fragments are the most important fragments in archaeology and they have the property that all points of the rim lie in the plane perpendicular to the rotational axes) and align them vertically. Next we perform the horizontal alignment by rotating one surface relative to the other until both surfaces have a maximum number of points in a common projection normal to the fixed surface. Note that after the rough alignment (vertical and horizontal) due to inaccurate estimation of the rotational axis the two surfaces may intersect (Figure 3.6d).

In the next step we have to align the surfaces of the objects to avoid intersecting surfaces. The correct match is calculated using a slightly modified ICP algorithm [100]. The difference to the standard ICP is that we are calculating the unique transformation that minimizes the mean square distances of the correspondences between the two surfaces to a constant value instead of zero. This distance d_n is the distance of the two surfaces on a plane perpendicular to the rotational axis where n denotes the vertical position on the axis. Corresponding points of the two surfaces are estimated by computing the Euclidean distance of the candidate points on the inner surface to the normal on the rotational axis for the point on the outer surface. The point

with the minimal distance is taken as corresponding point.

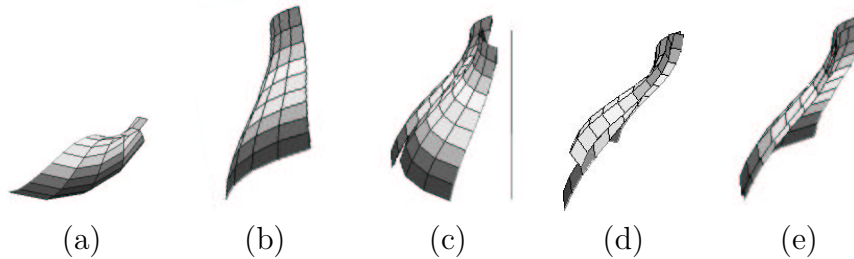


Figure 3.6: Registration steps using synthetic data.

The first estimation of all d_n is given by the range sensor. Since both range images are computed in the same environment and the fragments are placed on a plane, the range sensor computes the normal distance of the inner surface to the object plane on the lowest point of the surface - which is an estimation of the thickness of the fragment in a stable position.

Next the ICP starts by iteratively minimizing the error δ_i , which is the mean error of the local surface distances to d_n until all δ_i are positive (i.e. surfaces do not intersect). Then all d_n are updated to the mean distance of the surfaces in the direction of the rotational axis, the mean square error δ of the local surface distances are computed and the process is restarted. The algorithm ends if there are no significant improvements or the overall error increases. To sum up, the registration algorithm can be outlined as follows:

1. compute the axis of rotation for each view.
2. compute the vertical alignment by top points of each view.
3. compute the horizontal alignment until the maximum number of points in common projection is reached.
4. set all d_n to the same initial value given by the range sensor.
5. compute all actual distances d_n .
6. compute all errors δ_i .
7. iterate steps 5 and 6 until all δ_i are positive

8. update all d_n to new mean distance in direction of rotational axis.
9. iterate steps 5, 6, and 8 until all δ_i are minimal or MSE δ increases.

Figure 3.6e shows the result for synthetic range data with 50 surface points for each view and a distance of 2.9mm. The computed distance between the inner and the outer surface is 2.9mm. The registration error is $\delta=0.05$ mm, the mean square errors between the original and the computed axes are 0.26mm and 0.31mm respectively.

3.3 Profile Generation

The registration of front and back views together with the axis of rotation provide the profile used to reconstruct the vessel [55].

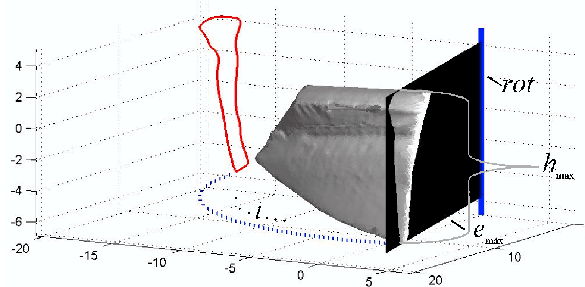


Figure 3.7: Orientated sherd, rotational axis rot , intersecting plane e_{max} and longest profile line.

Figure 3.7 shows the 3D model of a sherd and its rotational axis rot as a vertical line along the z -axis. The black plane represents the intersecting plane e_{max} at the maximum height h_{max} of the sherd. A profile line is the line formed by the intersection of the surface of the sherd and the intersecting plane. The longest profile line is the longest of these lines. The extracted profile line is shown in the xz -plane. Our algorithm for the estimation of the longest profile line consists of the following steps:

1. First the axis of rotation is transformed into the z -axis of the coordinate system in order to simplify further computation.

2. The fragment's size is estimated as described by its circular arc. Depending on the size we compute a number of intersecting planes e_i , which are used for the profile estimation. The number of planes e_i depends on the length of the perimeter of the fragment. Experiments have shown that 7 to 13 profile lines return the best ratio of exactness and performance. Figure 3.8 shows a sample of 4 planes e_i intersecting the 3D model and the plots of the extracted profile lines on the surface of the sherd.

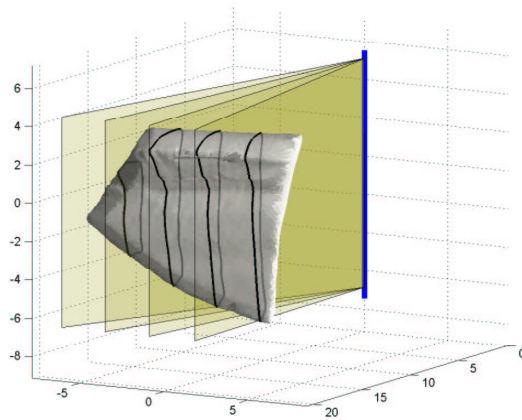


Figure 3.8: Sample of intersecting planes e_i .

3. A profile line is calculated by intersecting the 3D data of the fragment with planes e_i : First the distance of each vertex of the fragment to the plane e_i is calculated. All vertices are sorted by their distance to the plane. Then the nearest 1% of vertices are selected as candidates for the profile. For each of those vertices, all the patches to which they belong are filtered through a search in the patch list with their index number. In Figure 3.9 a sherd shaded by the value of distance to the intersecting plane is shown (lighter means nearer to the intersecting plane). Every patch is a triangle which consists of three points that are connected by three lines. Every pair of vertices that has a point on both sides of the plane is part of the profile line, because its connection intersects the plane. The coordinates of these pairs are rotated into

the xz -plane and the z -coordinate is removed. The result is a properly oriented profile line.

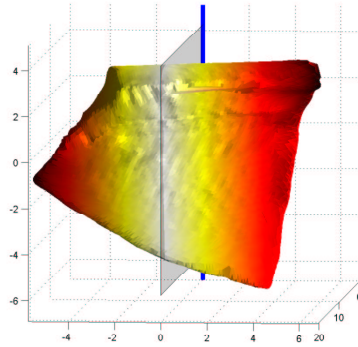


Figure 3.9: Properly oriented sherd and intersecting plane e_j . The greyvalues correspond to the distances. Lighter means nearer to the intersecting plane.

4. Next the longest profile line is determined: the difference between the maximum z -value and the minimum z -value of the profile line defines the height of the profile line. The remaining profile lines are used for evaluation of the estimate of the rotational axis.

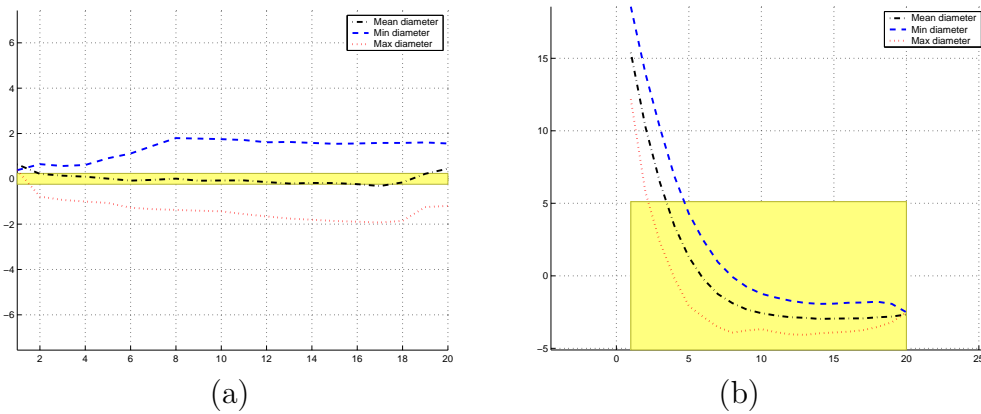


Figure 3.10: Maximum, mean and minimum diameters.

Figure 3.10 shows two plots of diameters based on the profiles from two different fragments. The y -axis is the difference of the diameters to the

overall mean diameter of all profiles in centimeter and the x-axis corresponds to the circular arc. The upper line shows the maximum diameter, the middle shows the mean diameter and the lower line shows the minimum diameter. The grey box allows the quality of the results to be visualized by showing the overall mean diameter of all profiles versus the standard deviation. If the standard deviation exceeds a certain threshold (for example 0.5 cm) the fragment is excluded from further reconstruction.

As seen in Figure 3.10a a correctly estimated rotational axis results in a mean diameter with a small standard deviation (smaller than 0.5 cm) along the perimeter of the sherd. Also the minimum and the maximum diameter are constant except on the left and right side, where the fracture of the fragment is located. In Figure 3.10b the mean diameter along the perimeter has a standard deviation of more than 0.5 cm (in this case 5 cm). This indicates that the estimate of the rotational axis is not accurate enough for further processing. In this case we plan to extend the algorithm for axis estimation by using additional information on the fragment e.g. 'rills' on the inner surface.

3.4 Results

In order to evaluate the results experiments with synthetic data have been performed. Figure 3.11 demonstrates the correctness of the algorithm by computing the axis of rotation of a cylinder with the parameters *cylinder radius* = 35 and *cylinder orientation* = [001]. The axis computed is described by $r = 35$, $v = [0, 000, 00 - 1, 00]$ showing a 100% theoretical accuracy of the approach.

Table 3.1 shows computed registration results for piece02 of box1: for each registered sherd the filename is given. The average outer diameter indicates the average distance of all data points of the outer surface to the axis of rotation. The inner diameter indicates the average distance of all data points of the inner view to the axis of rotation. Standard deviation is given for the outer and inner surface. A small standard deviation (< 0.1) indicates a smooth surface, no handles and correct orientation. The average thickness, given in cm is the difference between average outer diameter and average

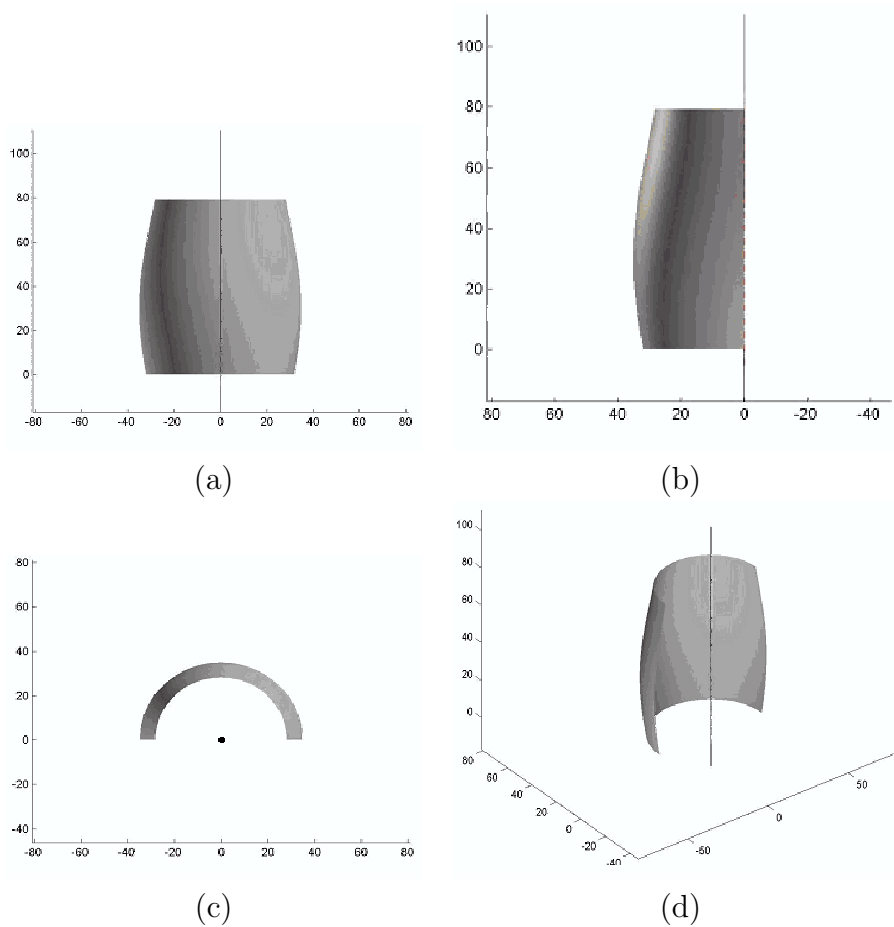


Figure 3.11: Evaluation of the axis computation using synthetic data.

inner diameter. Outer and inner angle range point out the proportion of the outer and inner surface on the whole pot based on the perimeter. This proportion is also given in percentage. The overlapping area shows the extend to which the two surfaces overlap.

Figure 3.12 shows registered views of piece02 from box1. It can be shown that the two recorded views are in alignment, which means that they have the same orientation.

As a second example Figure 3.13 shows registered views of a rather flat surface. Since the curvature is still non-ambiguously computed (see the top view), the registration could be performed.

The resulting 3D reconstruction of fragments depends on the correct ori-

Sherd #1: Files:	
box_01_piece_02_mvc0001 box_01_piece_02_mvc0003	
Average Outer Diameter:	19.7676
Standard deviation:	0.0593222
Average Inner Diameter:	13.8706
Standard deviation:	0.0153669
Average Thickness:	5.89702
Outer Angle-Range: (Total):	-8.75561deg to 9.1036deg 17.8592 - 4.96089%
Inner Angle-Range: (Total):	-9.51135deg to 8.27617deg 17.7875 - 4.94098%
Overlapping Area:	91.4951%

Table 3.1: Computed registration results.

entation of the profile section. The evaluation of the 3D representation is rather complicated since ground truth is not available due to the fact that there is no 3rd dimension in archaeological archive drawings, and that the object does not exist in reality. The description of shape is subject to the ideas of the archaeologists and is not standardized.

Experiments were done on all 40 fragments of our pottery database. The success rate for correct extraction of the profile line and consequently the percentage of sherds used for further reconstruction is around 50% of the data found at the excavation site. This should be compared to manual archivation done by archaeologists [90]: for coarse ware around 35% [19] and for fine ware around 50% [95] of the findings are used for further classification. It depends heavily on the shape of the fragment (e.g. handle, flat fragments like bottom pieces, small size, etc.). Eighteen fragments have been excluded from reconstruction due to incorrect estimation of the axis of rotation.

Table 3.2 shows samples of results for properly orientated fragments. Box and piece numbers are used for identification of the fragment. The radius r is the estimated mean radius of the whole object. The standard deviation of the radius was estimated along the perimeter of the fragment. The thickness of the fragment is the difference between the mean radius of the inner side and the outer side. The fragment size is the percentage of the perimeter of

Box Nr.	Sherd Nr.	Radius (<i>cm</i>)	Standard deviation (<i>cm</i>)	Mean thickness (<i>cm</i>)	Fragment size (%)
1	04	10,20	0,05	0,51	11,13
1	08	15,78	0,04	0,39	4,78
1	16	14,56	0,09	1,75	6,36
1	17	16,15	0,15	1,51	8,08
1	18	15,16	0,03	1,75	5,12
1	19	14,54	0,15	0,84	8,25
1	20	12,99	0,08	1,56	7,55
1	22	11,53	0,10	0,75	13,55
1	23	12,33	0,08	0,65	8,72
2	01	9,97	0,09	0,82	11,15
2	02	15,95	0,03	1,13	6,35
2	04	6,66	0,18	1,67	17,03
2	05	9,94	0,08	0,49	8,94
2	06	2,35	0,21	1,03	31,51
2	09	12,3	0,08	0,97	9,06
2	10	18,33	0,06	1,00	5,91
2	11	10,2	0,05	2,24	9,09
2	12	12,34	0,12	0,982	10,04
2	14	16,91	0,17	1,52	12,61
2	15	15,42	0,07	1,21	8,4
2	16	14,36	0,12	1,53	8,47
2	18	10.8	0,06	1,93	9,69

Table 3.2: Sample of Results.

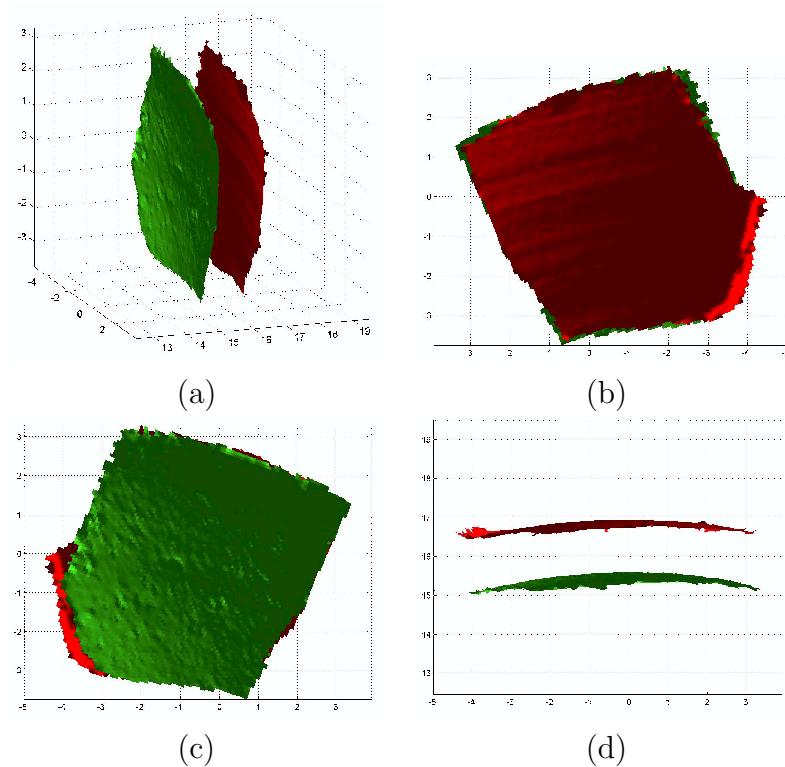


Figure 3.12: (a) registered views (b) registered inner view (c) registered view outer view (d) registered top view.

the sherd compared to the perimeter of the whole object.

Experiments with synthetic data have shown that the correctness of the reconstruction depends on the correct estimation of the axis of rotation (see [109] for a detailed survey) and on the resolution of the 3D scanner used. The number of vertices in the data used ranges between 4000 and 15000, leading to a profile line with 200 to 300 points. The execution time using a prototype written in Matlab running on a *Pentium III* 1 GHz is less than a minute per sherd. It depends heavily on the computation of the axis of rotation (70% to 80% of the execution time).

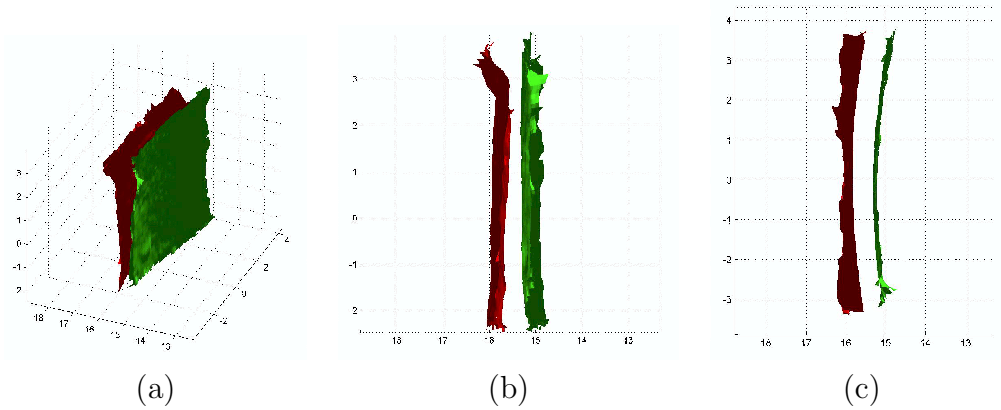


Figure 3.13: Box01, piece 14: registered views: (a) 3D view (b) side view and (c) top view.

3.5 Chapter Summary

In this chapter we described the processing of the fragment data in order to further automate archivation and reconstruction. The orientation, which defines the exact position of a fragment on the original vessel, was described by the axis of rotation. Rim fragments were detected by the computation of the orifice plane. In order to get a full 3D model, a front view and a back view of a fragment were registered. Registration was based on a model based approach. Out of the registered 3D model of the fragment, a profile section was computed. The profile section was the basis for the subsequent classification. In order to demonstrate the correctness of the processing tasks, experiments followed by a discussion were shown.

Chapter 4

Classification

The purpose of classification is not only to get a systematic view of the material found but also to find different fragments belonging to the same vessel based on attributes stored in an archive database. After that, the profile of the fragment can be used to reconstruct the original (complete) vessel. This includes the possibility of reconstructing missing parts of the vessel and the search for possible matches of other fragments already stored in the archive with the one that is under consideration (part-assembly).

This chapter is organized as follows. First we describe the determination of shape characteristics based on so-called characteristic points in Section 4.1. In Section 4.2 we take a closer look at the profile segmentation based on cubic splines. The generation of primitives is presented in Section 4.3. The chapter concludes with results (Section 4.4) of each section and a discussion of the selected concepts.

4.1 Determination of Shape Characteristics

By classifying the parts of the profile, the complete vessel is classified, and missing parts may be reconstructed. Following the manual strategy of the archaeologists, the profile should first be automatically segmented into its parts, the so-called *primitives*, [52]. Our approach to do so is a hierarchical segmentation of the profile into rim, wall, and base by creating segmentation rules based on expert knowledge of the archaeologists and the curvature

of the profile. These three segments of the profile are stored in a so-called **description** of the profile. Figure 4.1 shows an archive drawing of a fragment with its profile section divided into various primitives. If there is a corner point, that is a point at which the curvature changes “substantially”, the segmentation point is obvious. If there is no corner point, the segmentation point has to be determined mathematically [113, 1].

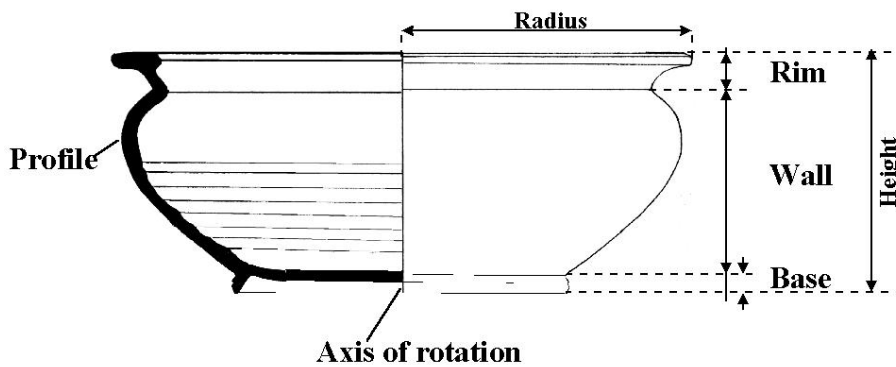


Figure 4.1: Profile with known primitives.

Up to now this segmentation has been done manually by archaeologists, and there are no segmentation standards in archaeology [1]. Figure 4.2 shows different shapes of manually segmented primitives.

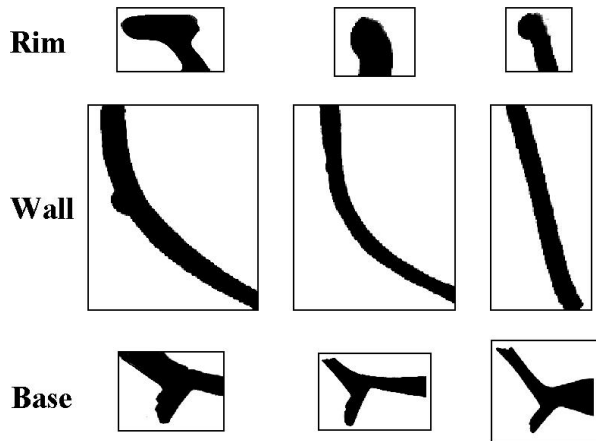


Figure 4.2: Different shapes of primitives.

The basis for the segmentation is the outer profile line, i.e. the profile line along the outside of the vessel. The segments of the profile are divided by so called characteristic points or segmentation points. Figure 4.3 shows the classification scheme applied to an “S-shaped vessel” as an example. The coordinate system has its origin at the intersection point of the axis of rotation and the orifice line.

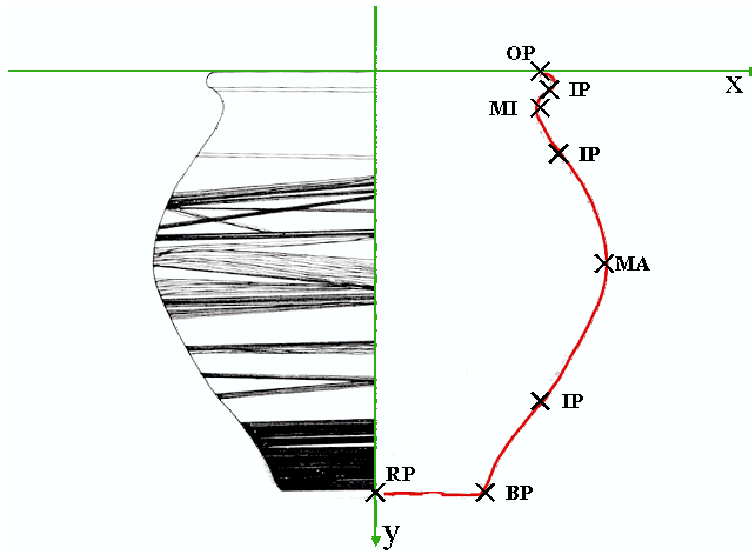


Figure 4.3: S-shaped vessel: profile segmentation scheme.

In order to allow proper segmentation, the following points have been identified.

- **SP starting point:** in the case of vessels with a horizontal rim: innermost point, where the profile line touches the orifice plane;
- **OP orifice point:** outermost point, where the profile line touches the orifice plane;
- **IP inflexion point:** point, where the curvature changes its sign, i.e. where the curve changes from a left turn to a right turn or vice versa;
- **MI local minimum:** point of vertical tangency; point where the x-value is smaller than in the surrounding area of the curve;

- **MA local maximum:** point of vertical tangency; point where the x-value is bigger than in the surrounding area of the curve;
- **CP corner point:** point where the curve changes its direction substantially;
- **BP base point:** outermost point, where the profile line touches the base plane;
- **RP point of the axis of rotation:** point where the profile line touches the axis of rotation; applied to non complete profile
- **EP end point:** point where the profile line touches the axis of rotation; applied to complete profiles

4.2 Curvature-based Segmentation

The profile determined has to be converted into a parameterized curve [115, 41] and the curvature has to be computed [6, 83]. Local changes in curvature [105] are the basis for rules required for segmenting the profile. The most formalized approach uses mathematical curves to describe the shapes of the vessels and more often their parts. The profile is thus converted into one or more mathematical curves. These approaches (i.e. the sampled tangent profile [77], the B-spline methods [36], the two-curve system [34]) provide the most precise representation so far, however no automatic comparison of complete profiles resulting from these methods has been published. The situation is complicated by the fact that ceramic vessels, produced by hand, do not have mathematically perfect surfaces which affects the application of the above mentioned methods. Consequently, the precision of the representation of the vessels is reduced [101].

In order to apply interpolation and approximation methods the profile is subdivided into sub-intervals by using corner points. Then the most appropriate interpolation and approximation methods are computed and selected for each of the intervals of the curve, the method with a smaller error (in case of ambiguity, the interpolation method is preferred) is selected for the interval. The approximation error of the representation over the whole curve

is computed via the sum of squares of the differences of the input value and the spline value. We apply four methods for interpolation and four methods for approximation by B -splines on the reconstruction of the vessel profiles [52], which we call multi-spline processing.

4.2.1 Cubic Splines

The following definitions were adopted from [21]. We suppose that the planar closed curve r to be fitted (interpolated or approximated) will be represented by parametric equations

$$\mathbf{r}(\mathbf{t}) = [\mathbf{x}(\mathbf{t}), \mathbf{y}(\mathbf{t})] \quad (4.1)$$

in an interval in the Cartesian coordinates of \mathcal{R}^2 and has continuous second derivatives. The curve is given by a set of points $P_i = [x(t), y(t)]$ together with the non decreasing sequence of knots $\{t_i, i = 1, \dots, n + 1\}$ of parameter t . Constructing a curve $S(t)$, which approximates the function given by the points can be done by a cubic spline with an adequate parameterization and external conditions. The curve must be initially divided into sub-intervals, where functional approximation and interpolation methods can be applied.

The support of a cubic spline is 5 intervals. Denote by B_i^4 a $k - th$ order spline ($k \leq 3$) whose support is $[t_i, t_{i+4}]$. Then it is possible to normalize these splines so that for any $x \in [a, b]$ equation 4.2 equals 1.

$$\sum_{i=-3}^{n+3} B_i^4(x) = 1 \quad (4.2)$$

Any cubic spline $S_n(x)$ with knots t_0, \dots, t_n and coefficients $a_{-3}, a_{-2}, \dots, a_n$ can be written in the form of equation 4.3.

$$S_n(x) = \sum_{i=-3}^n a_i B_i^4(x) \quad (4.3)$$

There are $n + 3$ coefficients a_i in equation 4.3 showing that the vector space of cubic splines has dimension $n + 3$, so that the $n + 1$ functional values will not determine $S_n(x)$ uniquely - two additional constraints must be supplied. Consequently, in evaluating $S(x)$ for any $x \in [a, b]$, only four terms at most in the sum (4.3) will be non-zero.

The basis cubic splines can be constructed by the following recurrent relationship:

$$B_i^n(x) = \frac{x - t_i}{t_{i+n-1} - t_i} B_i^{n-1}(x) + \frac{t_{i+n} - x}{t_{i+n} - t_{i+1}} B_{i+1}^{n-1}(x), \quad (4.4)$$

$i = -3, \dots, n - 1$ and $n = 1, 2, 3, 4$. A useful convention is to define the first-order splines as *right-continuous* so that

$$B_i^1(x) = \delta_i \text{ for } x \in [t_i, t_{i+1}), i = -3, -2, \dots, n + 3, \quad (4.5)$$

The method is of local character: the change of the position of one control vertex influences only 4 segments of the curve. The resulting curve is in particular coordinates a polynomial of 3rd degree for $t \in (t_j, t_{j+1})$ and all its derivatives are in continuous coordinates.

Since $B_i^n(x)$ is nonzero only on the interval $[t_i, t_{i+4}]$, the linear system for the B -spline coefficients of the spline to be determined, by interpolation or least-squares approximation, is banded, making the solving of this linear system particularly easy.

$$S^4(x_j) = \sum_{i=0}^n B_i^4(x_j) a_i = y_j, \quad j = 0, \dots, n \quad (4.6)$$

for the unknown B -spline coefficients a_i in which each equation has at most 4 nonzero entries.

4.2.2 Interpolation by Cubic B-Splines

For data point interpolation (i.e. an exact fitting of data points by a curve, see the Figure 4.4), we selected four methods which we empirically showed to be appropriate in our experiments:

- a) Cubic spline interpolation with Lagrange end-conditions (*cs1*) (i.e. the additional end-condition for the first and for the last data site matches endslopes to the slope of the cubic that matches the first four data at the respective end [18]).
- b) Cubic spline interpolation with not-a-knot end-condition (*cs2*), meaning that it is the unique piecewise cubic polynomial with two continuous

derivatives with breaks at all interior data sites except for the leftmost and the rightmost one).

- c) Spline interpolation with an acceptable knot sequence (*cs3*) (i.e. The knot sequence knots is acceptable for interpolation to data in the sense that there is exactly one spline of order k with knot sequence knots that matches given data at those sites).
- d) Spline interpolation with an optimal knot distribution (*cs4*). As 'optimal' knot sequence the optimal recovery theory of Micchelli, Rivlin and Winograd [87] is used for interpolation at data points $\tau(1), \dots, \tau(n)$ by splines of order k

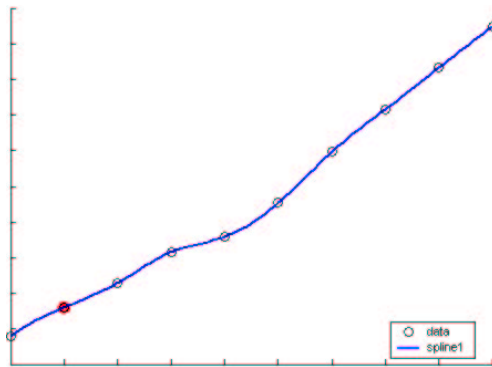


Figure 4.4: Interpolation by B-spline functions.

These methods are applied to each of the intervals of the curve, and their approximation error is evaluated on the given data set.

All the discussed interpolation methods satisfy the Schoenberg-Whitney conditions, i.e. the achieved representation is unique for the method, the given data and knot sequences. The selection of a unique interpolation representation of the curve in the particular interval is made using the following criteria in the respective order:

1. Minimal approximation error in the corresponding interval.
2. Minimal length of the knot sequence

3. Priority of the interpolation method based on the statistical observations

The priority of the methods was achieved experimentally on profiles and their particular intervals as follows: 1. Cubic spline interpolation with Lagrange end-conditions (*cs1*); 2. Cubic spline interpolation with not-a-knot end-condition (*cs2*); 3. Spline interpolation with an acceptable knot sequence (*cs3*); 4. Spline interpolation with an optimal knot distribution (*cs4*).

4.2.3 Approximation by Cubic B-Splines

Since the number of data pairs acquired to describe a vessel or its parts do not always suffice to represent the shape of the vessel reliably, interpolation is not always the appropriate method. For this reason, we compared the approximation methods to the interpolation methods in terms of how well they represent the overall shape of the whole curve. For data point approximation (i.e. an approximate fitting of data points by a curve with respect to a minimal approximation error over the interval from which the data points are taken, see Figure 4.5), we selected four methods which appeared as appropriate based on our experiments. As in the interpolation case, the approximation error is measured as the sum of squares of the differences of the input value and the spline value. The following approximation methods were applied and compared:

- a) Cubic smoothing spline with the smoothing parameter $p > 0$ (*cs5*);
This smoothing spline f minimizes $p \sum_{j=1}^n w_j (y_j - f(x_j))^2 + (1 - p) \int (f^{(2)}(t))^2$ with $w_j = 1, j = 1, \dots, n$, where n is the number of data points. (For $p = 0$, the smoothing spline is the least-squares straight line fit to the data, while, at the other extreme, i.e. for $p = 1$, it is the 'natural' or variational cubic spline interpolant).
- b) Smoothing spline with the smoothing parameter $tol > 0$ (*cs6*);
This function creates the smoothest function f in the sense that $F(f^{(2)}) = \int_{x_1}^{x_n} (f^{(2)}(t))^2$ is the smallest, for which $E(f) = \sum_{j=1}^n w_j (y_j - f(x_j))^2 \leq tol$, with the weights $w_j = 1$ and data points $x_j, j = 1, \dots, n$ (where n is the number of data points).

- c) Least squares spline approximation with the number of knots equal to a half of the number of data points (*cs7*).
- d) Least squares approximation with the number of knots equal to the number of data - degree of the spline in the particular interval (*cs8*).

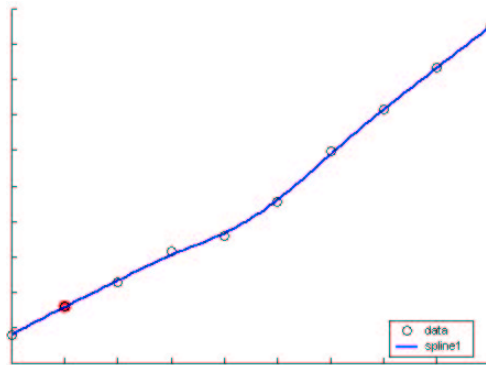


Figure 4.5: Approximation by B-spline functions.

The approximation errors of both smoothing spline methods *cs5* and *cs6* vary significantly, depending on the selection of the parameters $p > 0$ and $tol > 0$, respectively. A correct selection of p and tol can decrease the error over the interval, but there is no simple method known for such a selection which would in general guarantee that the approximation error of the corresponding functions is minimal. In the case of the cubic smoothing spline with parameter p (*cs5*), we used $p = 1$ to give a variational cubic spline interpolant (and thus 'low' errors with respect to the data). (As the setting of tol in the method *cs6* is more difficult, this method did not appear as appropriate for creating an automated system, part of which the selection of the curve representation is intended to be).

An 'optimal' (in the sense of the compared methods, given data and the applied criteria for selection) method is selected according to the same criteria as in the interpolation case and again, the priority ordering of the methods was achieved experimentally: 1. Cubic smoothing spline with the smoothing parameter $p > 0$ (*cs5*); 2. Smoothing spline with the smoothing parameter $tol > 0$ (*cs6*); 3. Least squares spline approximation with the

number of knots equal to a half of the amount of the data (*cs7*); 4. Least squares approximation with the number of knots equal to the number of data - degree of the spline (*cs8*).

4.3 Generation of Primitives

The attributes of a successful classification have been summarized by Orton and others [90, 95]:

- objects belonging to the same type should be similar (internal cohesion)
- objects belonging to different types should be dissimilar (external isolation)
- the types should be defined with sufficient precision to allow others to duplicate the classification
- it should be possible to decide to which type a new object belongs

In order to achieve these aims our classification scheme of the vessel form is based on two aspects [57]:

- absolute measurements and ratios
- segmentation of the profile line

The first step is the measurement of the following parameters: rim diameter, bottom diameter, height, x- and y- values of all segmentation points. With these measurements a variety of ratios can be calculated. A specific choice of these ratios is in each case characteristic for one vessel type; for example the ratio rim diameter to the height of the fragment.

The characteristic points together with the following measurements are used to define basic vessel forms and types [3]:

- **Rim-diameter** *rdm*: The diameter of the orifice plane
- **Wall-diameter** *wdm*: The maximum diameter of the object orthogonal to its rotational axis

- **Bottom-diameter** bdm : Diameter at the bottom of the object
- **Height** h : The overall height of the object
- **The characteristic ratio** r_{chr} : The ratio between height h and rim-diameter rdm : $h : rdm$

Together with archaeologists [2] three levels of hierarchical classification rules based on the work of R. Schreg [112], Andraschko et al. [3] and G. Webster [129] have been worked out. They consist of three consecutive levels *ware*, *basic form* and *basic type*, see Table 4.1. These rules were applied to the late Roman burnished ware of Carnuntum [33]. The first classification level defines the excavation site, where the objects were found.

I	ware	Late Roman Burnished Ware
II	basic form	beaker, plate, bowl, pot, jug
III	basic type	beaker1, beaker2, pot1, pot2, plate1-2, plate11-2, plate13-7 jug1, jug2-3, jug4

Table 4.1: 3 levels of classification.

Classification level II defines *basic forms* (see Table 4.2). The grouping follows functional aspects based on characteristic ratios and diameter. A variation of $\pm 15\%$ is taken into account. For example, a plate is defined by $r_{chr} = 1 : 8$ and rdm ranging from $16cm$ to $34cm$.

basic vessel form	$r_{chr}(+/- 15\%)$	rdm	wdm
plate	1:8	16-34 cm	-
bowl	1:2 - 1:4	10-16 cm 12-30 cm	- -
beaker	1:1	8-11 cm	5-14 cm
jug	4:1 - 2:1	6-14 cm	
pot	1:1 - 3:1	8-12 cm 12-16 cm	15-25 cm 18-21 cm

Table 4.2: Classification level II: specific vessel forms.

The forms are sub-divided into *basic vessel types* (see Table 4.3), which are defined in level III. The grouping follows the characteristic properties of

the profile section and the position of the characteristic points. Table 4.3 shows the rules and images of all vessel types which are taken into account. References of all forms to Grünewald [33] and representative images of the specific form are given. For example, a plate is further specified by not having an inflection point IP and no curvature point CP . In practice, basic forms have names or labels like “*Knickwandschüssel*”.

4.4 Results

First we show results of finding characteristic points using the multi-spline method. Next we present experiments on the segmentation of the characteristic points, which is followed by examples of automatic classification. The pottery dataset used for the experiments was already classified by archaeologists and published by Grünewald [33]. Besides the manual drawings of the fragments, the fragments themselves were available. In order to evaluate the classification results achieved, we randomly selected 8 fragments from the pottery dataset, classified them, and compared the results to manual classification results of the same fragments.

Four interpolation and four approximation methods were applied for every sub-interval of the curve after each run of the program. While the curve was generated gradually for each sub-interval of the curve, the overall approximation error was computed. As a result, the profile was constructed from the selected methods and was compared to the data set. Table 4.4 displays the approximation errors for all methods in all intervals of the vessel 70-1 [33], including the selected interpolation and approximation methods for the corresponding interval and the selected overall method for the whole profile. In our experiments the most frequently selected interpolation method was *cs1* and the most frequently selected approximation method was *cs6*. An interpolation method was preferred in the intervals where a sufficient number of data points with respect to the length of the interval was available. An approximation method was preferred in the intervals where there was a lack of data.

Spline interpolation with an acceptable knot sequence *cs3* in all inter-

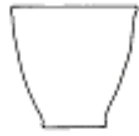
basic vessel types	charact. points	charact. properties of the profile	reference Grünewald [33]	image
Beaker1	1 IP, no CP	section $rdm \gg bdm$	78/1-4	
Beaker2	> 1 IP	$rdm \approx wdm$	78/6	
Plate1-2	1 IP, no CP	$f(x+1) > f(x)$	71/9; 75/1-4	
Bowl1-2	1 IP, no CP	$f(x+1) \geq f(x)$ $MA(y) < \frac{h}{10}$	70/1-6; 71/2	
Bowl3-7	CP, > 1 IP	$f(x+1) \gg f(x)$	72/5-8;73/1-3;74/4,6-8	
Pot1	> 1 IP	$rdm \ll bdm$ $rdm \ll wdm$ $MA(y) > \frac{h}{5}$	79/2; 81/2	
Pot2	1 IP, no CP	$rdm \ll wdm$ $MA(y) \cong \frac{h}{2}$	79/1,3	
Jug1	> 1IP	$rdm \approx wdm$ $wdm \gg bdm$	-	
Jug2-3	CP	$rdm \approx bdm$	84/10	
Jug4	> 1 IP or CP	$rdm < 12cm$	84/1-3,8; 85/2-7,9-11	

Table 4.3: Classification level III: basic vessel types.

vals of all profiles approximated the data with a smaller error than spline interpolation with optimal knot distribution.

method / interv.	1	2	3	4
cs1	0.2163	0	0.6047	0.0781
cs2	0.2163	0	0.5994	0.0782
cs3	0.2163	0	0.5994	0.0782
cs4	0.2163	0.6169	2.1080	0.0877
cs5 ($tol = 5$)	0.2163	2.3114	0.5994	1.1816
cs6 ($p = 1$)	0.1350	0	0.6229	0.07812
cs7	0.2163	5.9470	5.5298	0.5015
cs8	0.2163	0.0032	0.6014	0.1308
select. intp.	1	1	2	1
select. appr.	6	6	5	6
overall select.	6	1	2	1
method / interv.	5	6	7	8
cs1	1.1685	2.2497	1.1424	0.0884
cs2	1.1686	2.2514	0.1433	0.0884
cs3	1.1686	2.2514	0.1430	0.0883
cs4	1.4510	2.3485	0.1615	0.0991
cs5 ($tol = 5$)	2.9430	2.2514	2.2073	0.0884
cs6 ($p = 1$)	1.1687	2.2496	0.1646	0.0884
cs7	6.9127	6.2323	0.8617	1.0675
cs8	1.1850	3.8347	0.1430	0.2551
select. intp.	1	1	1	1
select. appr.	6	6	8	6
overall select.	1	6	1	6

Table 4.4: Approximation errors for all methods in all intervals.

We take the outer profile line as basis for the segmentation: Figure 4.6 shows two examples of automatically segmented pots with the characteristic points detected shown in (b), and the appropriate manual segmentation in (a).

Applying level II of the classification scheme to the curves computed gives a first indication of the group to which the object belongs. Table 4.5 summarizes results from 8 fragments. The most important measurement is the diameter of the rim rdm , because its estimation does not depend on whether

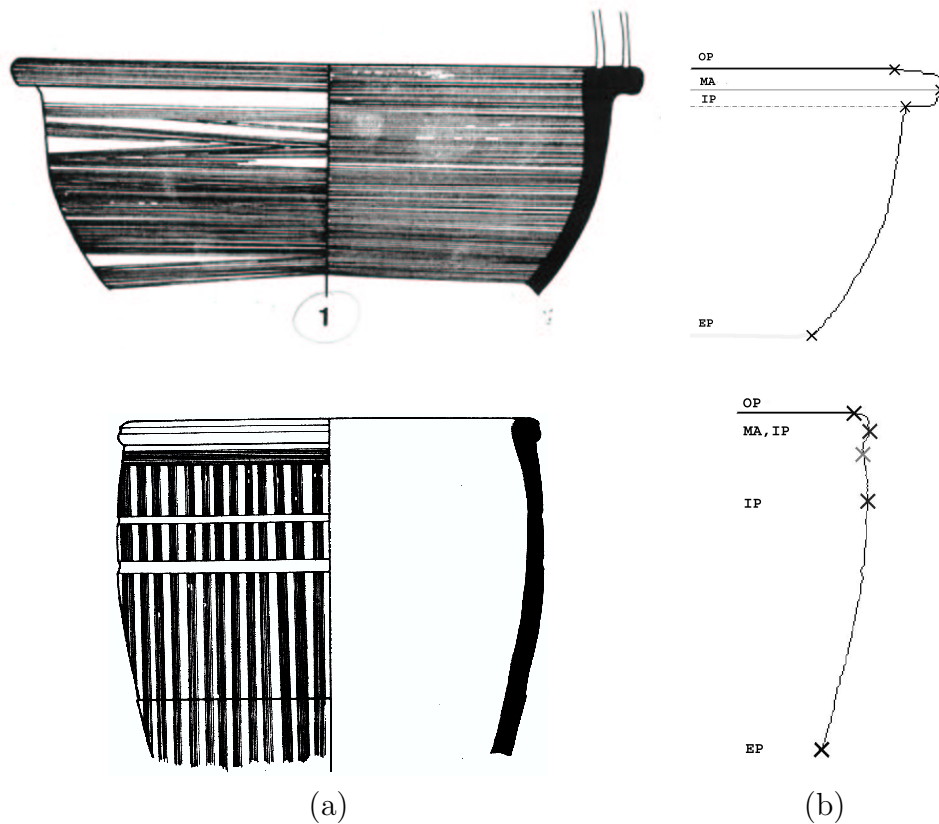


Figure 4.6: Classified pot 70/1: (a) manual drawing, (b) detected characteristic points

the object is a fragment or a vessel. On the contrary the diameter of the bottom bdm represents only a reliable indicator for vessels, because the bdm of a fragment is not the same as the bdm of the whole vessel.

For example, the rdm of fragment 70/1 is $15.6cm$, which allows the forms *plate*, *bowl* and *pot*. Its characteristic ratio $r_{chr} = 1 : 1.5$ excludes *plates*, leading to *bowl* and *pot* as indication. Ambiguities are resolved within classification level III.

Table 4.6 shows results of the estimation of characteristic points. Except for IP, where the number of IPs found is shown, the coordinates of the characteristic points are given. One of the most reliable indicators is the number of IPs, because it identifies S-shaped forms by simply counting points with-

ID [33]	rdm	wdm	bdm	h	r_{chr}	indication
70/1	15.6	19.2	9.2	10.2	1 : 1.5	bowl, pot
70/4	19.6	21.6	9.6	6.4	1 : 3.0	bowl
72/6	14.4	17.0	5.2	7.4	1 : 1.9	bowl,pot
72/8	22.2	24.2	7.2	10.0	1 : 1.2	bowl
75/3	29.6	32.4	16.2	5.6	1 : 5.3	plate
78/2	6.4	7.2	4.6	9.2	1.4 : 1	jug, pot, beaker
79/2	12	14.0	5.2	10.6	1 : 1.1	pot, beaker
81/1	12.4	15.4	4.8	11.3	1 : 1.1	beaker, pot

Table 4.5: Classification level II: Characteristic forms.

out requiring of their position. The y-position of the MA characterizes forms reliably, because its approximate position is sufficient.

To continue the previous example with fragment 70/1, the forms *bowl* and *pot* are further investigated: The position of MA indicates that it is not a pot, since it lies within the first 20% of the height h . Having 1 IP only gives priority to Bowl1-2, which actually is a correct classification [33].

ID	OP	MA	MI	$\#IP$	CP	BP	RP	EP
70/1	[7.8, 0.0]	[9.6, 0.8]	EP	1	-	-	-	[4.6, 10.2]
70/4	[9.8, 0.0]	[10.8, 0.8]	BP	1	-	[4.8, 6.4]	-	-
72/6	[7.2, 0.0]	[8.5, 1.0]	EP	3	-	-	-	[2.6, 7.4]
72/8	[11.1, 0.0]	[12.1, 0.9]	EP	3	-	-	-	[3.6, 10.0]
75/3	[14.8, 0.0]	[16.2, 0.8]	BP	1	-	[8.1, 5.6]	-	-
78/2	[3.2, 0.0]	[3.6, 0.5]	EP	2	-	-	-	[2.3, 9.2]
79/2	[6.0, 0.0]	[7.0, 1.5]	EP	1	-	-	-	[2.6, 10.6]
81/1	[6.2, 0.0]	[7.7, 1.8]	EP	1	-	-	-	[2.4, 11.3]

Table 4.6: Classification level III: Characteristic types.

Table 4.7 summarizes the results for the eight randomly selected fragments. The results achieved indicate the same basic vessel forms as published by [33], except for 79/2 and 81/1. The reason is that distinction between forms *pot1* and *pot2* is not possible for fragments, where the bottom is missing, because it depends only on the relative position of MA.

ID [33]	level II	classification rules applied	indication
70/1	bowl, pot	1 IP, $MA(y) < \frac{h}{5} (\cong 0.8 < 2.0)$	Bowl1-2
70/4	bowl	1 IP, $MA(y) < \frac{h}{5} (\cong 0.8 < 1.3)$	Bowl1-2
72/6	bowl, pot	3 IP, $MA(y) < \frac{h}{5} (\cong 1.0 < 1.5)$	Bowl3/7
72/8	bowl	3 IP, $MA(y) < \frac{h}{5} (\cong 0.9 < 2.0)$	Bowl3/7
75/3	plate	1 IP	Plate1-2
78/2	jug, pot	2 IP, $rdm > bdm$; $MA(y) < \frac{h}{5} (\cong 0.5 < 1.8)$	Beaker1
79/2	pot, beaker	1 IP, $MA(y) < \frac{h}{5} (\cong 1.5 < 2.1)$	Pot1, Pot2
81/1	pot, beaker	1 IP, $MA(y) < \frac{h}{5} (\cong 1.8 < 2.3)$	Pot1, pot2

Table 4.7: Final Classification

4.5 Chapter Summary

In this chapter we presented the classification of the profile section based on the manual approach of the archaeologists. In order to define shape characteristics, a classification scheme was defined. The profile was segmented based on local changes in curvature, therefore B-Splines have been applied to the profiles. Three levels of classification based on characteristic measurements and the segmentation of the profile allowed the grouping of the fragment into specific vessel forms and specific vessel types. Results were shown for each intermediate step. The classification scheme presented depends on the excavation site. In order to apply our algorithm to other fragment-fabrics we have to redefine the classification scheme based on the characteristics of the specific fabric.

Chapter 5

Mosaicing

The assembling of an object from pieces is called mosaicing [70]. In our case, mosaicing refers not only to the reconstruction of a pot from its fragments, but also to the reconstruction of a pot or fragment out of its profile section. It is similar to the automatic assembly of jigsaw puzzles, which among others has been addressed by [13]. In [68] a system for analyzing and assembling a 2D image of pieces of a jigsaw puzzle is presented. The matching method is based on the shape and color characteristics of the pieces. However these approaches rely on specific characteristics of the pieces like color, critical points, or no gaps between matching pieces.

More generally mosaicing can be seen as a special case of object recognition by approximate outline matching: The specific problem of identifying adjacent ceramic fragments by matching the shapes of their outlines was considered by Üçoluk and Toroslu [126]. They represent the 3D fragments by their boundary curves. From the 3D boundary curve data, curvature and torsion scalars are computed. A noise tolerant matching algorithm serves to find the best match of two such circular strings. Üçoluk and Toroslu disregard the interior of the broken surface and their method is therefore restricted to thin-walled objects. No experiments with real pottery data are reported.

Hori et. al. [40] propose a method for joint detection among two potsherds designed for pottery fragment outlines. They consider that 2D images instead of 3D shape data are applicable. Their approach is based on a partial verification method of a pair of contours without knowledge of the shape features of a piece.

Kong et. al. [67] approach the jigsaw problem in two stages: first, local shape matching aims to find likely candidate pairs for adjacent fragments. Second ambiguities resulting from local shape matching are resolved by a global solution. The matching is based on the notion of an alignment curve to represent a correspondence between two curves. They generalize the curve matching to 3D by computing a distance metric based on speed, curvature, and torsion. Experiments are shown, but no explanation of the accuracy and usability of the method are given.

2D Potsherd reconstruction based on shape similarities is presented by Kanoh et. al. [64]. In a first step they join potsherds in two dimensions. The contour of a potsherd is divided into sub-contours by salient points [104], and the matching of the sub-contours is performed by P-type Fourier descriptors. In the second phase, three dimensional shape is recovered by mapping the 2D points into the 3D coordinate system of a cone or a cylinder. They claim that their system only works for thin, moderately flat and small fragments, consequently their approach is limited to a very specific range of fragments. The computed 3D model only represents the real object if the shape of the real objects corresponds to a cone or cylinder.

Marques et al. [80] present a 2D object matching technique based on the comparison of a reference contour to the contours in the image partition. The comparison is based on a distance map that measures the Euclidean distance between any point in the image to the partition contours. The accepted transformations depend on the minimum of a given cost function.

H.C.G. Leitão introduced, in her PHD-thesis [72], a method for automatic reassembly of two-dimensional fragments. Together with Stolfi [73] she demonstrates a multiscale matching method based on the idea that the outlines of two matching fragments are two noisy copies of the same time-domain signal. They compute the curvature encoded fragment outlines in order to compare possible matching candidates. To reduce the cost of computing the optimum pairing for a candidate, they progressively increase scales of resolution. The implementation is restricted to flat objects, such as tiles and murals. For curved fragments the three-dimensional geometry of the fracture line must be recovered with fairly high resolution, so as to have a representation of the fracture line that is insensitive to the fragment's orientation in

three dimensions.

G. Papaioannou et. al. [91, 93] present a semi-automatic reconstruction of archaeological finds from a geometric point of view: they rely on the broken surface morphology to determine correct matches between fragments. In the first stage they estimate coarse surface regions (i.e. the fractured side of the fragment) by surface bumpiness estimation [92]. It is based on a region growing algorithm, which estimate the deviation of the surface normals from an average surface normal. If the deviation exceeds a certain threshold, a new region is defined. In the second stage, a matching error is calculated for all candidate regions of every possible pair of fragments. Minimizing the matching error through enhanced simulated annealing performs fragment matching. The third stage computes the final reconstruction by selecting those fragment combinations that minimize an overall error. The method was tested on up to 35 statuary fragments, of which 90 percent were matched correctly.

Summarizing existing techniques on the assemblage of virtual pots we observe a main focus on the analysis of the outline of the break curve: 2D outline matching is most common [73, 64, 67, 13, 68], but work on 3D outline matching exist [126]. Surface matching of fractured surfaces is proposed in [91]. So far, no complete system from acquisition to reconstruction has been described.

This chapter is organized as follows. In Section 5.1 we introduce the determination of the description language based on the work of Sablatnig [107] and Menard [85]. Then we present the fragment retrieval in order to get the optimal pairing of matching candidates (Section 5.2). Section 5.3 describes the algorithm for matching the oriented and classified fragments. The chapter concludes with a chapter summary.

5.1 Determination of Description

In order to reconstruct complete pots out of fragments, profiles with similar attributes are to be found in an archive database. Classification of newly found fragments of unknown type is performed by comparing the description of the new fragment with the description (see Section 4.1) of already classified

fragments. The fragment structure is formed by its *shape features* (or geometric features like the profile) and its *properties* (or material like clay, color and surface) as shown in Figure 5.1. The description of the fragment is structured in a description language consisting of primitives and relations. Primitives are a representation of shape features, relations represent the properties.

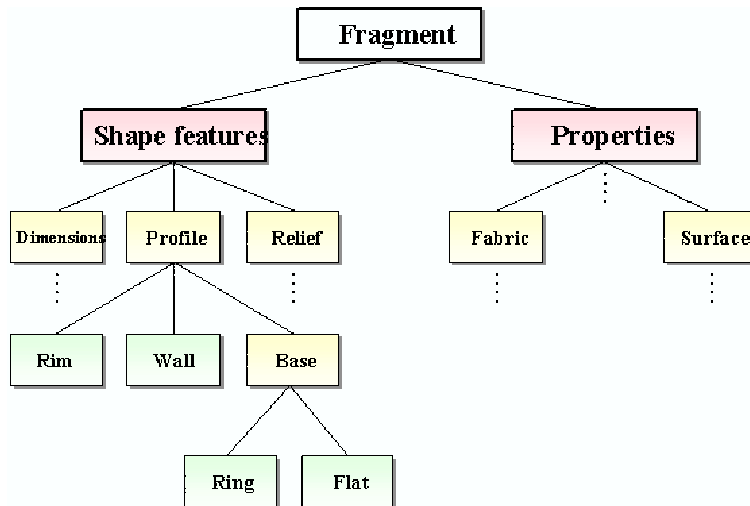


Figure 5.1: Fragment structure.

From the description language point of view, the modeling can be interpreted as a syntactic pattern recognition approach in which the primitives are transformed into the vocabulary and the relations are transformed into a grammar [29]. This approach makes use of the idea of shape decomposition; it divides complex shapes into simple elementary units, i.e. primitives. This can be seen as an application of semantic networks [17], because semantic networks are labeled, directed graphs whose nodes represent objects, sub-objects, or shape primitives and whose arcs represent relations between them. A set of attributes that describe different features is attached to each node; a set of attributes that describe different properties is attached to each arc. Once the fragment is transformed to this representation all operations for classification and reconstruction can be executed on this graph structure. The advantage of a description language lies in the uniqueness of representation, different fragments result in different descriptions, similar fragments result in similar descriptions [107].

The description language, which was originally designed to solve 2D automatic visual inspection problems [107], is applied and extended in order to solve the classification problems. The actual profile contains features, which are a representation of shape features. To accomplish classification, primitives are further subdivided into part-models (or part- primitives), the consistency between part-primitives is established by relations among part parameters.

Formally, the description language is a graph $G = \langle O, R \rangle$, where $O = \{m | 1 \leq m \leq n\}$ denotes the set of nodes and $R = \{\langle c, d \rangle | c, d \in O\}$ the set of arcs. A node O consists of different sub-objects or primitives. Each node has different attributes a , with weights w , and a tolerance $T(a)$ defined as

$$T(a) = \begin{cases} 1, & \text{if } |a^{db} - a^{nw}| \leq c, \text{ and} \\ \frac{1}{|a^{db} - a^{nw}|} & \text{otherwise} \end{cases} \quad (5.1)$$

where c is the allowed tolerance, a^{db} denotes the value of attribute a in the archive, and a^{nw} the value of the attribute a of the object.

Two nodes are in relation according to R . Each relation $\langle c, d \rangle$ is decomposed into k sub-relations between the same nodes, each with a weight v and a tolerance $T(r)$. Figure 5.2 shows the graph and the inner structure of nodes and arcs. The shape primitive $S1$ is subdivided into c different shape primitives (such as profile, diameter and the like). For each of these shape primitives n different sub-primitives (such as rim, wall and the like) are defined. Since the manual segmentation of the profile varies tolerances and weights are included in the description. Note that all attributes and relations contain numerical values.

The weights w and v are necessary for classification. Each property has a certain weight in order to verify the corresponding description to a given fragment. The verification of fragment to description consists of verifying whether the number and type of features and primitives are the same. Next, attributes and relations are checked to verify whether they match within given tolerances. Comparing all attributes of a node and its successors with the model carries out the verification process. The confidence for a node can be computed based on the result of the comparison:

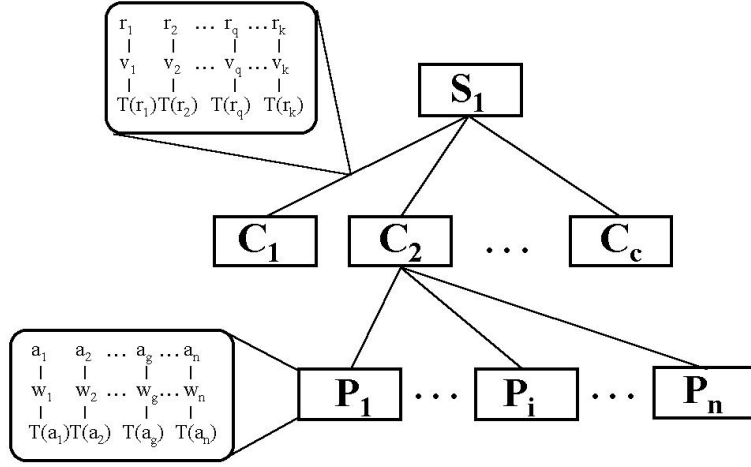


Figure 5.2: Description language graph.

$$conf(p) = \sum_{g=1}^n w_g * T(a_g) + \sum_{(p,q)}^m v_{(p,q)} * conf(q). \quad (5.2)$$

where w_g are the weights of the attributes of the nodes and $v_{(p,q)}$ the weights of the sub-relations of the arcs. Observe that n , the number of attribute values, and m , the number of arcs, depend on the node p . Moreover, for leaves we have:

$$conf(p) = \sum_{g=1}^n w_g * T(a_g). \quad (5.3)$$

This enables us to compute the confidence of a node by summing up the weighted tolerances of each attribute of the node and the overall confidence of the subgraph connected to this node. By computing the consistency for different descriptions, the one with the highest confidence value can be chosen if the confidence is above a certain threshold. For a given profile all primitives are represented in the description of the profile.

5.2 Fragment Retrieval

In order to describe a vessel or a fragment using the description language, primitives and attributes together with their weights have to be defined.

The optimal setting of the weights was found empirically. We defined the following primitives and attributes (Figure 5.3):

1. **Pot** P : a pot is a complete pottery object, which consists of one to many fragments. It is the reconstructed pot. It has its own coordinate system called the pot coordinate system.

Attributes:

- fabric ($f_P, w = 1$): the fabric defines the excavation site.
- Vessel coordinates ($v_P, w = 1$): The pot coordinate system defines the position of the fragments on the pot.

2. **Fragment** F : A fragment represents a piece of a pot and consists of many primitiva.

Attributes:

- Primitive ($pt_F, w = 0.9$): Rim, wall or base.
- Profile Line ($pl_F, w = 0.9$): Cross section of the fragment in the direction of the axis of rotation. The profile is used for classification.
- Height ($h_F, w = 0.5$): Height of the fragment.
- Characteristic ratio ($r_{chr_F}, w = 0.6$): The ratio between height and rim-diameter.
- Characteristic points ($ch_F, w = 0.7$): These points divide the profile line into its primitives.
- Color ($c_F, w = 0.9$): Color of the fragment.
- Position ($p_F, w = 0.9$): Bottom up or bottom down position of the fragment.
- Material ($m_F, w = 1$): Type of material of the fragment.
- Archaeological Editor ($ed_F, w = 1$): A person who found the piece.
- Archaeological Label ($lb_F, w = 1$): Specific archaeological label of the fragment.

- Prospectus Drawing ($dr_F, w = 1$): A drawing of the fragment, which may be used for archaeological publications.
- Date: ($dt_F, w = 1$): Finding date.

3. **Rim (R):** A rim is the upper part of a fragment.

Attributes:

- Rim Diameter ($rdm_R, w = 1$).
- Starting point ($sp_R, w = 1$).
- Orifice point ($op_R, w = 0.9$).
- Inflexion point ($ip_F, w = 0.9$).
- Local maximum ($ma_F, w = 1$).

4. **Wall (W):** A wall is the middle part of a fragment.

Attributes:

- Wall diameter ($wdm_W, w = 1$).
- Inflexion point ($ip_W, w = 0.8$).
- Local maximum ($ma_W, w = 0.8$).
- Local minimum ($mi_W, w = 0.8$).
- Corner point ($cp_W, w = 0.6$).
- End point ($ep_W, w = 1$).

5. **Base (B):** A base is the lower part of the fragment.

Attributes:

- Bottom diameter ($bdm_B, w = 0.8$).
- Local maximum ($ma_B, w = 0.8$).
- Local minimum ($mi_B, w = 0.8$).
- Base point ($bp_B, w = 0.9$).
- Corner point ($cp_W, w = 0.7$).
- Point of the axis of rotation ($rp_B, w = 1$).

Following the definition of primitives, relations between them complete the description.

- R1: $F = \{m \in P | 1 \leq m \leq n\}, v = 1$, A pot consists of one to many fragments.
- R2: $v = 1$, Rim fragments have an orifice plane.
- R3: $v = 0.8$, Wall fragments have neither an orifice plane nor bottom plane.
- R4: $v = 0.8$, Bottom fragments have a bottom plane.
- R5: $r_{chr_F} = 1 : 8, v = 0.6$, Defines a plate by its characteristic ratio.
- R6: Rim: $rdm_F = [16..34cm], v = 0.9$ Defines a plate by its rim diameter.
- R7: $r_{chr_F} = 1 : 2 - 1 : 4, v = 0.6$ Defines a bowl by its characteristic ratio.
- R8: Rim: $rdm_F = [10 - 16; 12 - 30cm], v = 0.8$ Defines a bowl by its rim diameter.
- R9: $r_{chr_F} = 1 : 1, v = 0.6$ Defines a beaker by its characteristic ratio.
- R10: Rim: $rdm_F = [8 - 16cm], v = 0.9$ Defines a beaker by its rim diameter.
- R11: Wall: $wdm_F = [5 - 14cm], v = 0.9$ Defines a beaker by its wall diameter.
- R12: $r_{chr_F} = 4 : 1 - 2 : 1, v = 0.6$ Defines a jug by its characteristic ratio.
- R13: Rim: $rdm_F = [6 - 14cm], v = 0.9$ Defines a jug by its rim diameter.
- R14: $r_{chr_F} = 1 : 1 - 3 : 1, v = 0.6$ Defines a pot by its characteristic ratio.
- R15: Rim: $rdm_F = [8 - 12; 12 - 16cm], v = 0.9$ Defines a beaker by its rim diameter.
- R16: Wall: $wdm_F = [15 - 25; 18 - 21cm], v = 0.9$ Defines a beaker by its wall diameter.

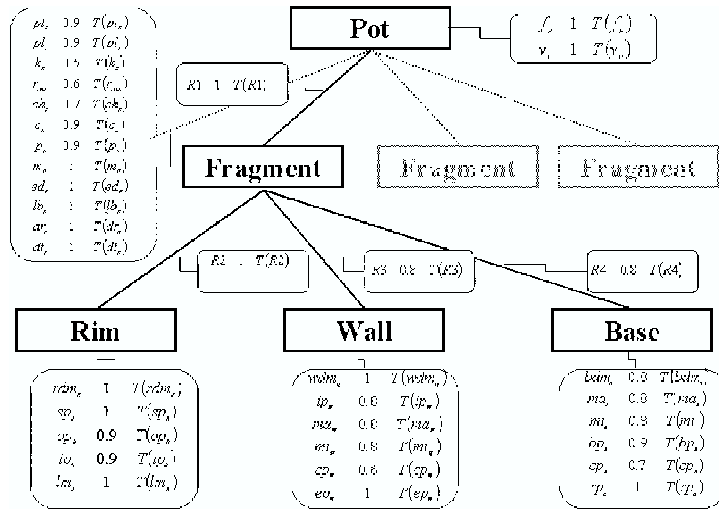


Figure 5.3: Description language for archaeological pottery.

Figure 5.4 describes an example for the retrieval. Each fragment has a unique number when archived. Together with all attributes the fragment is stored in the description. The left side shows a profile, which was classified as bowl and separated into edge (E048), border (B012), and ringbase (R145). These primitives are the basis for the classification and reconstruction process. On the right hand side a fragment, which is not yet classified is depicted, thus the type of the pot is not yet known. The profile is manually segmented into its primitives by an archaeologist and the corresponding attributes like color, surface, and dimensions are determined. In order to classify the fragment (find the pot in the database that matches the fragment) the generated description is compared with already existing descriptions. If the profile primitives of the fragment can be found in the description and other attributes match within a given tolerance, the type of the fragment can be classified as bowl. Furthermore, missing parts of the fragment (like the base in this case) can be reconstructed based on the already stored information.

5.3 Fragment Matching

The optimal pairing of matching candidates obtained as in from the previous section serves as input for the fragment matching part. Consequently we

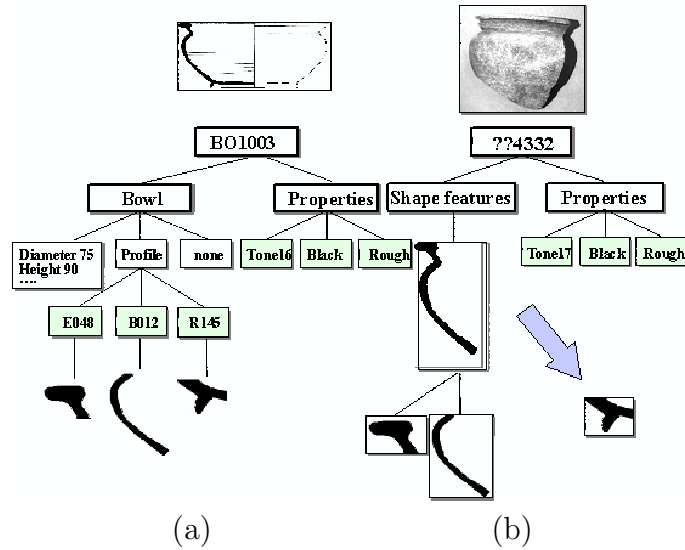


Figure 5.4: Retrieval of similar fragments: a) description of known bowl, b) description of fragment of unknown type.

know those pairs of fragments which were probably adjacent in the original object. We virtually glue two matching fragments together by computing the transformation parameters, which bring two candidate fragments into alignment.

In order to represent the matching of two fragments, G. Papaioannou et al. [91] describe seven pose parameters. In their approach the two fragments are first prealigned so that their broken facets face each other. In our case we know the orientation of a fragment, consequently we prealign two candidate fragments by simply aligning their axis of rotation. As a result, a two-degrees-of-freedom continuous search space is defined. The transformation which matches two candidate fragments consists of a translation along the z-axis with parameter T_z and a rotation around the z-axis with parameter R_z (see Figure 5.5).

The basic concept in our method for estimating R_z is that the best fit is likely to occur at the relative pose which minimizes the point-by-point distance between the facing outlines. For this reason, we introduce a matching error ϵ_M based on the mean Euclidian distance between the corresponding points of the outlines of the candidate fragments with points $X = (x, y)$ and

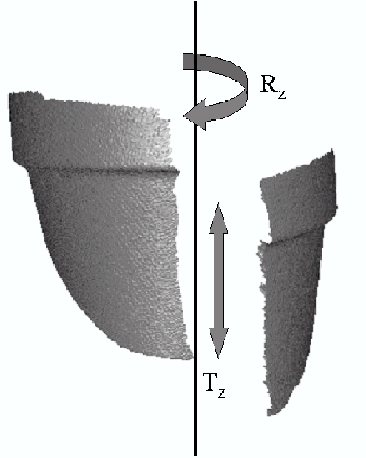


Figure 5.5: Fragment Matching with 2-degrees-of-freedom.

$X' = (x', y')$:

$$\epsilon_M = \frac{1}{N} \sum_{i=1}^N \sqrt{(x_i - x'_i)^2 + (y_i - y'_i)^2}. \quad (5.4)$$

where N is the number of data points used. The height of the fragment, which was estimated in Section 4.3 limits the length of the matching segments. Different fragments types lead to the following matching possibilities:

- A Rim fragments: first T_z is computed by aligning the rim along the orifice plane. Next R_z is estimated, so that the positioning transformation with the smallest matching error ϵ_M is considered to be the correct position. Figure 5.6 shows matching outlines of two rim-fragments.
- B Bottom fragments: first T_z is computed by aligning the bottom along the base plane. Next R_z is estimated in the same way as for rim fragments.
- C Wall fragments: Candidates are first aligned along their profile sections. Next R_z is estimated in the same way as for rim fragments. Since it is not clear whether a new candidate fragment is in bottom up or bottom down position, we have to compute R_z and T_z for both positions. The positioning transformation with the smallest matching error ϵ_M is considered to be the correct position.

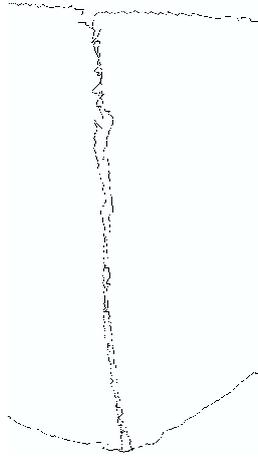


Figure 5.6: Matching outlines.

Matching algorithm

1. Define reference fragment F_{ref} with its axis of rotation ROT_{ref} : defines a new pot P , creates the pot coordinate system, ROT_{ref} is aligned to the z-axis.
2. Prealignment of the candidate fragment F_{cand} by its axis of rotation ROT_{cand} : ROT_{cand} is aligned to ROT_{ref} . This results in a two-degrees-of-freedom search space.
 - (a) translation T_z along the axis of rotation (up/down).
 - (b) rotation R_z around the axis of rotation.
3. Estimation of the translation parameter T_z : search for minimal distance d between all y-values (radius) of the profile of F_{ref} and the profile of F_{cand} .

Exception A: Rim fragments are aligned along the orifice plane.

Exception B: Bottom fragments are aligned along the base plane.

When the candidate fragment is a wall fragment, the minimal distance d is computed for both positions, and the one with the smaller is considered to be the correct position.

4. Estimation of the rotation parameter R_z by finding the position with the smallest matching error ϵ_M .

5.4 Chapter Summary

In this chapter we described the assembly of an object from pieces, which in our case means the reconstruction of a pot from its fragments, but also the reconstruction of a pot out of its profile section. In order to find the confidence between two fragments, a description language was applied. A vessel or fragment was transformed into the description language by defining primitives and attributes. In order to find the candidate fragments that could match a fragment the generated description is compared with already existing descriptions. Since we know the orientation of the candidate fragments we defined a two-degrees-of-freedom search space for representing the alignment of two fragments. A matching algorithm based on the minimal arc length between points of the fragment's outline was proposed.

Chapter 6

Reconstruction Results

This chapter presents the tests performed on the reconstruction method described in this work and analyzes their results. We have tested our reconstruction method on object models, both computer generated and 3D digitized models of real fragments. First we illustrate results on the reconstruction of profiles in Section 6.1. Then we present results and experiments for the reconstruction of fragments out of their profiles (Section 6.2). Results for the vessel reconstruction out of multiple fragments are shown in Section 6.3. In Section 6.4 an archaeologist comments the results of the thesis. Finally Section 6.5 concludes with a short summary.

6.1 Reconstruction of Profiles

We illustrate three reconstructed profiles which thereby represent further profile reconstructions from our pottery dataset. The x- and y axis denote the diameter and the height ($y = 0$ in the middle) of the fragment respectively. The area between the inner and outer profile is drawn black in order to have a similar representations as manual drawings. This automatically generated drawing is intended to use in archaeological publications.

Figure 6.1a shows the profile of fragment 1 from box 2 (Figure 6.1b) with an average inner diameter of 9.56 and an average outer diameter of 10.38. The computed average thickness is 0.81cm. The average height of the fragment is 6.5cm. The profile represents a wall fragment, which is indicated by the straight ending at the top of the profile.

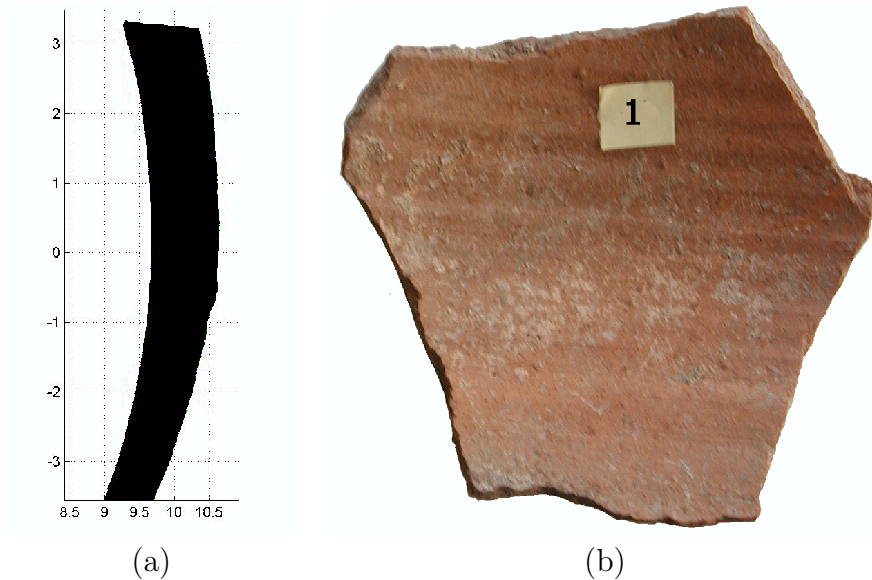


Figure 6.1: (a) reconstructed profile section and (b) Image of fragment 1 from box 2.

Figure 6.2a shows the profile of fragment 6 from box 2 (Figure 6.2b) with an average inner diameter of 2.01 and an average outer diameter of 3.04. The computed average thickness is 1.03cm. The average height of the fragment is 10.06cm. The profile represents a rim fragment, which is indicated by the curved ending at the top of the profile.

Figure 6.3a shows the profile of fragment 8 from box 1 (Figure 6.3b) with an average inner diameter of 15.58 and an average outer diameter of 10.97. The computed average thickness is 0.39cm. The average height of the fragment is 5.1cm. The profile represents a wall fragment, which is indicated by the straight ending at the top of the profile.

As discussed in Section 3.4 the evaluation of the profile reconstruction is rather complicated since ground truth is not available due to the fact that there is no 3rd dimension in archaeological archive drawings.

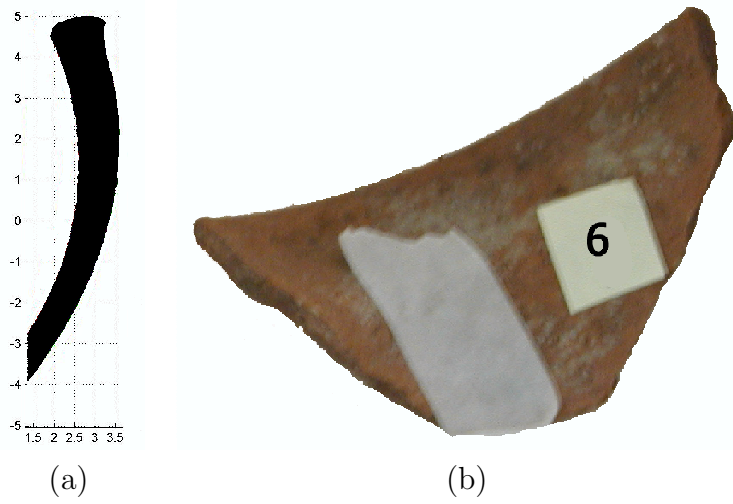


Figure 6.2: (a) Reconstructed profile section and (b) Image of fragment 6 from box 2

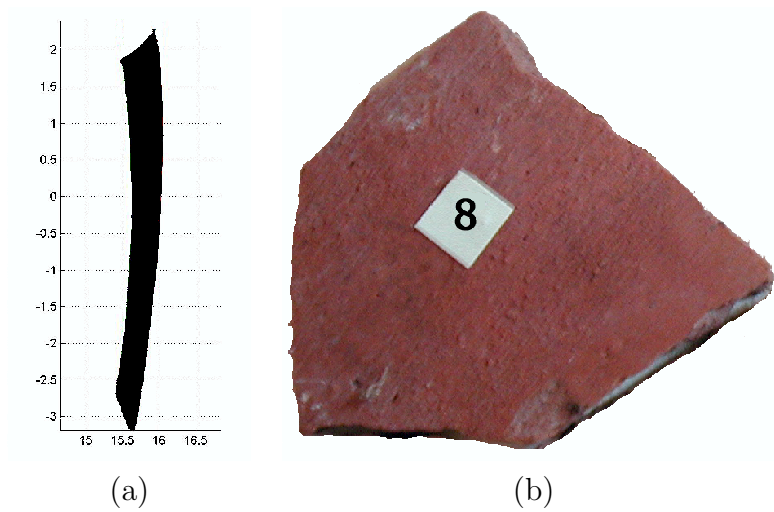


Figure 6.3: (a) Reconstructed profile section and (b) Image of fragment 8 from box 1

6.2 Reconstruction of Fragments out of their Profile

The rotation of the profile section along its axis of rotation leads to a virtual model of the fragment or the whole vessel. We construct the profile using methods described in Section 3.3. A computed profile and the axis of rotation are shown in Figure 6.4a. It was rotated 360 degrees around the axis of rotation in order to construct the vessel in 3D. Next the resulting 3D point cloud was triangulated and the acquired texture was mapped onto the triangulated mesh. Figure 6.4b shows the reconstructed pot.

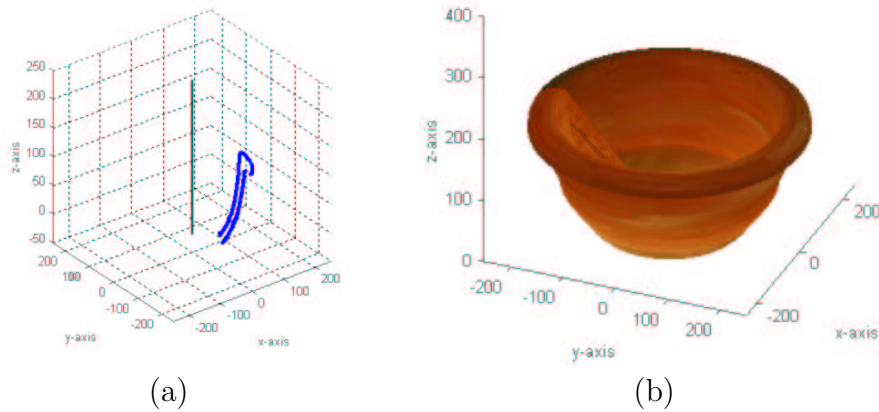


Figure 6.4: 3D profile section and 3D reconstruction out of the profile section.

In order to demonstrate the correctness of the computed profile lines, Figure 6.5 shows a recorded sherd (dark object) and its computed profile section (vertical line). The computation of the virtual fragment (grey object) is based on the profile section. One can see that the recorded fragment fits into the virtual fragment, which indicates that the computation is correct. Looking at multiple cross-sections along the perimeter of the virtual fragment (Figure 6.6a), one can observe hardly any deviation from the original fragment. Some deviations are caused by the bumpiness of the surface, because it is not exactly rotationally symmetric, since it is hand-made pottery.

If the fragment was not orientated correctly, the recorded fragment does not fit into the virtual object and multiple cross-sections along the perimeter

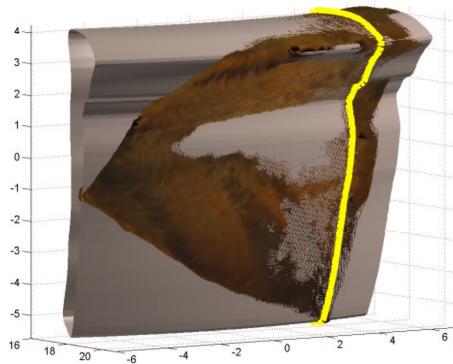


Figure 6.5: Reconstructed fragment, profile section and recorded fragment: correct reconstruction.

of the virtual fragment show large deviations from the original object (see Figure 6.6b).

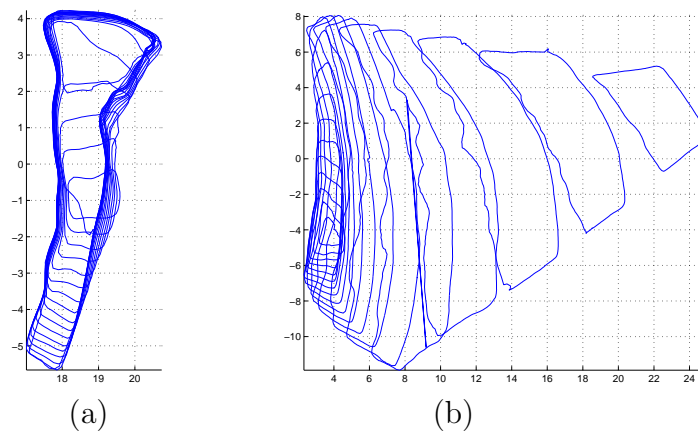


Figure 6.6: Multiple profile lines: (a) using a correct estimated rotational axis (b) using an incorrect rotational axis.

Figure 6.7 shows an incorrect reconstruction due to incorrect computation of the axis of rotation. It shows a recorded sherd (dark object) and its computed profile section (light line). The computation of the virtual fragment (grey object) is based on the profile section. One can see that the recorded fragment does not fit into the virtual fragment, which indicates that the computation is not correct.

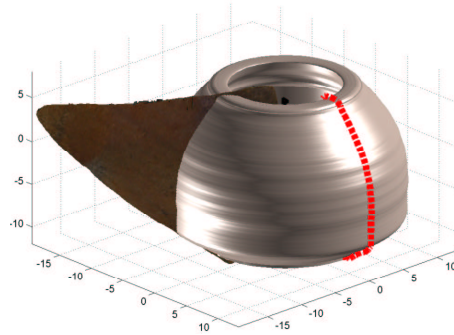


Figure 6.7: Reconstructed fragment, profile section and recorded fragment: incorrect reconstruction.

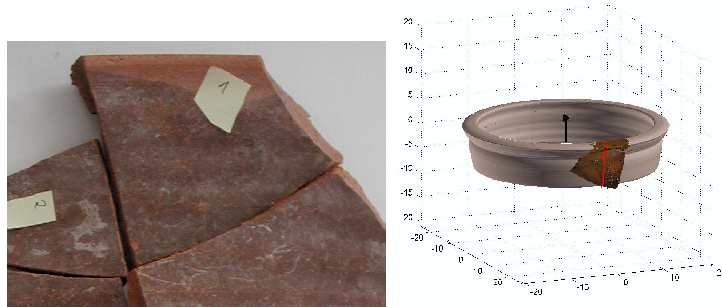


Figure 6.8: Reconstructed vessel piece 04-01: (a) image and (b) reconstruction.

Rotating the profile section 360 degrees around the axis of rotation leads to a virtual reconstruction of the vessel. The resulting virtual model visually gives an idea about the size and the shape of the object. It is not possible to say if the virtual model represents the real model correctly since ground truth is not available, e.g. if a feature like a handle is not present in the fragment data, it is also not present in the reconstruction. In order to overcome this drawback we need to find the fragment, which contains the handle of that specific vessel. Figure 6.8a shows an image of a rim fragment (piece01,box 4), and (b) the reconstructed vessel.

Two examples of wall fragments are presented in Figure 6.9a and b. As in the previous example, one gets an idea about the shape and the size of the

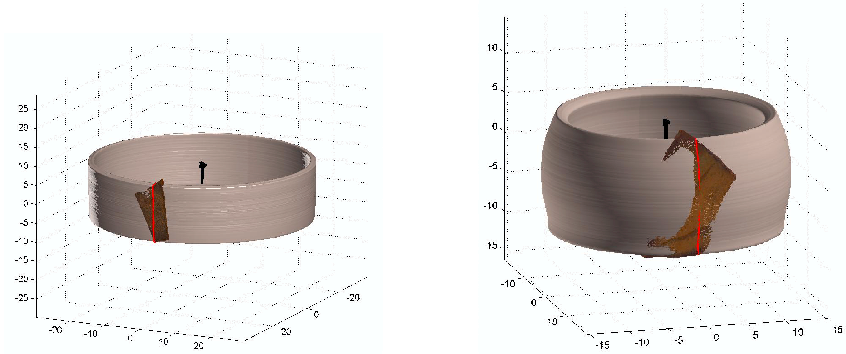


Figure 6.9: Reconstruction of a fragment out of its profile section ((a) piece04-09 and (b) piece04-07).

original vessel, but there is no indication of possible handles, for example.

6.3 Reconstruction of Vessels out of Multiple Fragments

A series of experiments were run upon synthetic 3D data, parts of commercially available flowerpots and fragments of our 3D pottery dataset. We present results on each type of experiments.

6.3.1 Synthetic Data

In order to evaluate the results we have tested our method on synthetic 3D data of three parts of a synthetic pot. Part 1 represents a rim fragment and contains 39559 points, part 2 represents a rim fragment too and contains 2700 points, and part 3 represents a wall fragment and contains 21750 points. The orientation of the fragments is defined, which leads to three perfect matching parts. Figure 6.10 and Figure 6.11a show the three parts as mesh plot together with their axis of rotation.

Starting with part one as reference fragment for each candidate the matching error was computed. Since the data provides perfect matches, a minimal value of the matching error $\epsilon_M = 0.00$ was found for both candidate fragments. No matching error between fragment two and three was computed

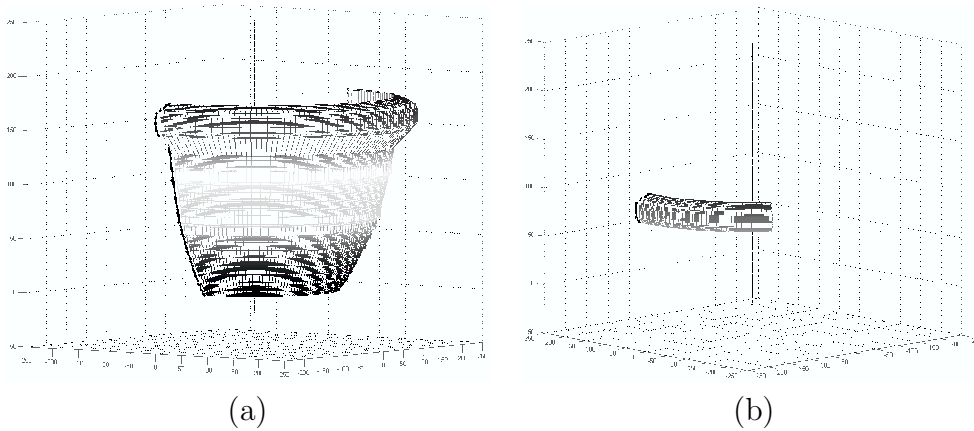


Figure 6.10: Synthetic 3D data: (a) part 1 and (b) part 2 of a synthetic pot.

because there was no alignment between their profile sections (i.e. part two is exactly above part three). Figure 6.11b shows the reconstructed object. Table 6.1 summarizes T_z , R_z and the matching errors for each possible candidate. RF_{nr} and CF_{nr} denote the number of the reference fragment and the number of candidate fragment respectively, and ϵ_M denotes the matching error. The experiment shows a 100% theoretical accuracy of the approach.

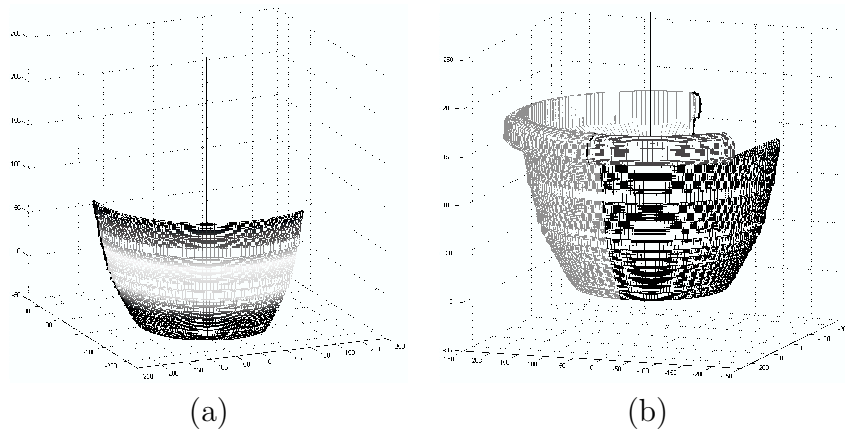


Figure 6.11: (a) part 3 of a synthetic pot and (b) Matching parts 1, 2, and 3.

To find out if the method is working on real data, we used a flowerpot with known dimension which is described in the next section.

$RF_{nr.}$	$CF_{nr.}$	T_z [mm]	R_z [deg]	ϵ_M
1	2	70	60	0.00
1	3	53	125	0.00
2	3	x	x	x

Table 6.1: Results of the matching process using synthetic 3D data.

6.3.2 Flowerpot

In order to get data of matching fragments of a whole pot, we broke a flowerpot into 5 parts (See Figure 6.12). We got three rim fragments, one wall fragment and one bottom fragment. Each part was digitized leading to a front and back view of each fragment. Table 6.2 shows the number of points and triangles computed. The biggest part (nr. 2) covers half of the pot and consists of 135070 triangles, whereas the smallest consists of 8210 triangles.



Figure 6.12: 5 parts of a flowerpot.

Next we computed the orientation of the fragments, which leads to four matching candidates and one not processable object: a large part of the bottom fragment (see Figure 6.13) consists of flat area. It was therefore excluded from further processing due to its curvature being too low.

Starting with part one as reference fragment for each candidate a matching error was computed. Next part two was defined as reference fragment and again for each remaining candidate a matching error was computed. This procedure was continued until no candidate remained. Table 6.3 summarizes

part nr	view	points	triangles
1	front	43045	85299
1	back	43169	85417
2	front	68185	135070
2	back	54640	106641
3	front	21713	42853
3	back	22729	44847
4	front	14715	28676
4	back	4234	8180
5	front	9378	18393
5	back	10031	19668

Table 6.2: Number of points and triangles.

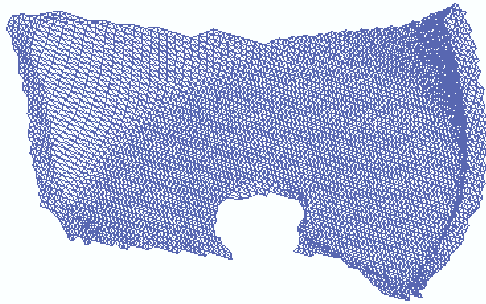


Figure 6.13: Part 4: bottom fragment.

T_z , R_z and the matching errors for each possible candidate. $RF_{nr.}$ and $CF_{nr.}$ denote the number of the reference fragment and the number of candidate fragment respectively, and ϵ_M denotes the matching error. The value of ϵ_M for correct matches ranges from 1.12 to 0.63, the combination of part 3 and 5 shows an incorrect match with an error ϵ_M of 12.92.

Figure 6.14a displays the resulting match of part 1 and part 3 as both parts are rim fragments, T_z was computed by alignment along the orifice plane (see Section 3.1.1). Figure 6.14b shows the resulting match of part 1 and part 5. Since part 5 is a wall fragment the ϵ_M was computed for both possible positions, and the position with lower ϵ_M was finally chosen.

Figure 6.15 shows the final reconstruction of the pot. Correct matches

$RF_{nr.}$	$CF_{nr.}$	T_z [mm]	R_z [deg]	ϵ_M
1	2	12.03	22.81	1.12
1	3	8.67	-41.29	0.81
1	5	9.34	73.21	0.63
2	3	-4.94	17.61	0.92
2	5	-10.02	-26.75	0.71
3	5	11.10	32.99	12.92

Table 6.3: Translation T_z in [mm], Rotation parameter R_z in [deg] and matching error ϵ_M of all candidate fragments.

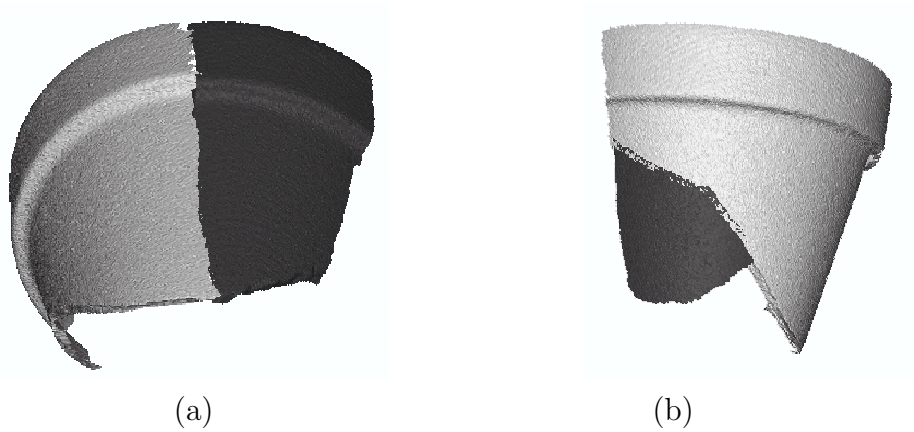


Figure 6.14: Matched parts: (a) part 1 and part 3 (b) part 1 and part 5.

for all four candidate fragments have been found. The missing bottom of the pot is due to part 4, not being processable because of its flat shape.

6.3.3 Archaeological Fragments

We applied our technique to real archaeological fragments (Nr: 319-71, 209-71 from the late Roman burnished ware of Carnuntum [33]), as shown in Figure 6.16. Both pieces are rim fragments. Each part was digitized leading to a front and back view of each fragment. Table 6.4 shows the number of points and triangles computed.

Next we computed the orientation of the fragments. The alignment along the orifice plane allowed the estimation of $T_z = 7.49\text{cm}$. The smallest $\epsilon_M = 0.31$ was found for $R_z = 3.35^\circ$. Figure 6.17a shows the matched

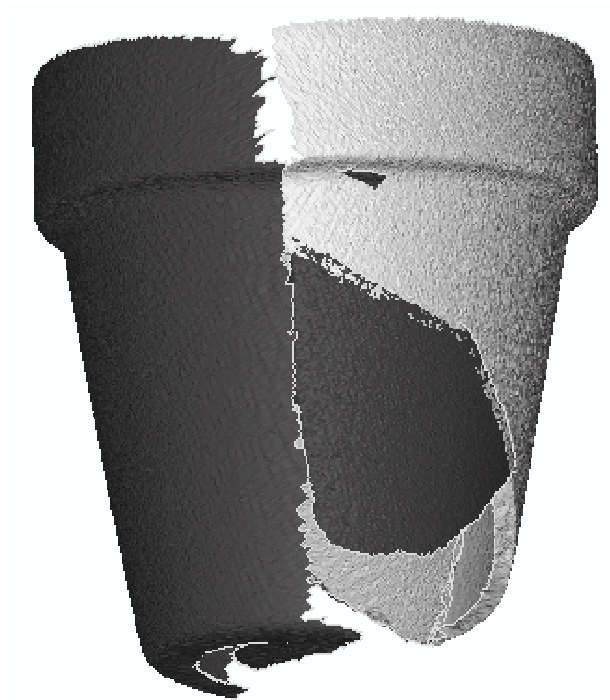


Figure 6.15: Matching parts 1, 2, 3, and 5

outlines of the two fragments and Figure 6.17b shows the final reconstruction. Due to the dense sampling and the non eroded fracture sides of the original fragments (the fragment was possibly broken during excavation) the reconstruction method managed to yield to a small matching error.

part nr	view	points	triangles
1	front	15248	26774
1	back	14979	25255
2	front	2526	3680
2	back	2836	4059

Table 6.4: Number of points and triangles.

Another example on real archaeological fragments is shown in Figure 6.18: (a) One rim and (b), (c) two wall fragments from the common ware of Sagalassos were recorded and their geometrical representation is shown.

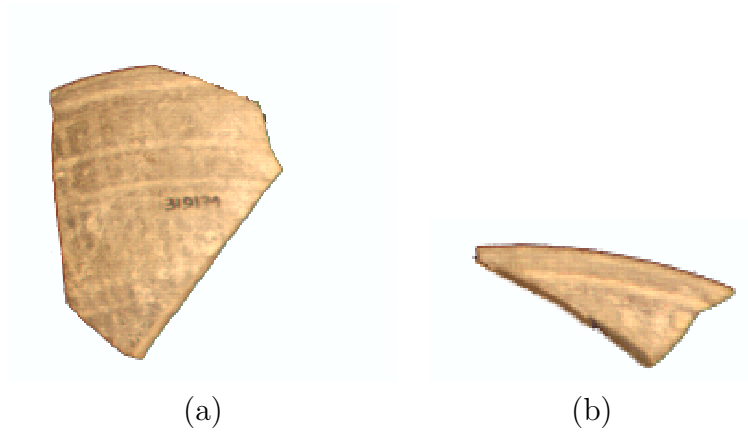


Figure 6.16: Archaeological rim fragments: (a) Part1, (b) Part 2.

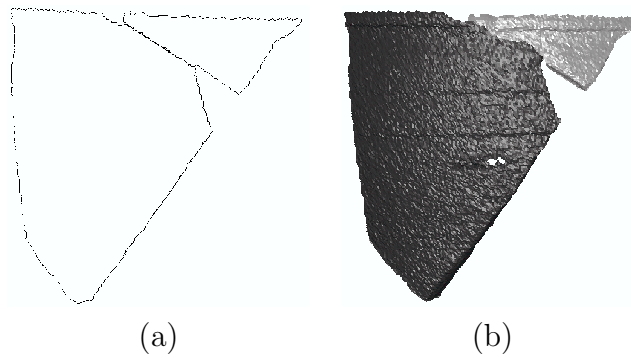


Figure 6.17: Archaeological rim fragments: (a) Matching outlines, (b) Matching parts.

The number of points and triangles of the front and back views are shown in Table 6.5.

After the estimation of the orientation we started with part one as reference fragment and computed for each candidate a matching error. Next part two was defined as reference fragment and again for each remaining candidate a matching error was computed. This procedure was continued until no candidate remained. Table 6.6 summarizes T_z , R_z and the matching errors for each possible candidate.

Correct matches were found between part one and part two ($\epsilon_M = 1.32$) and part two and part three ($\epsilon_M = 1.21$). No correct match was found

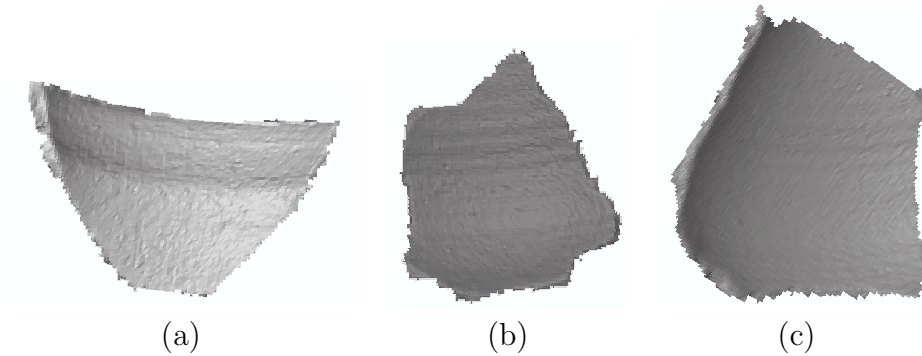


Figure 6.18: Archaeological rim fragments: (a) Part 1, (b) Part 2, (c) Part 3.

part nr	view	points	triangles
1	front	4770	9156
1	back	4800	9222
2	front	6575	12712
2	back	6685	12952
3	front	7720	14982
3	back	8566	16522

Table 6.5: Number of points and triangles.

between part one and part three ($\epsilon_M = 14.81$), because there was no alignment of the profile sections (part one is on top of part three). Nevertheless all three fragments were matched together, since the matching of part two succeeded for both candidates. Figure 6.19a shows the matched outlines of the fragment one and two and Figure 6.19b shows the final matching of three fragments. The reconstructed pot out of the combined profile sections of part one and part two together with its axis of rotation is shown in Figure 6.19c.

$RF_{nr.}$	$CF_{nr.}$	T_z [mm]	R_z [deg]	ϵ_M
1	2	-4.29	11.70	1.32
1	3	-1.61	7.59	14.81
2	3	-5.19	15.76	1.21

Table 6.6: Results of the matching process using archaeological data.

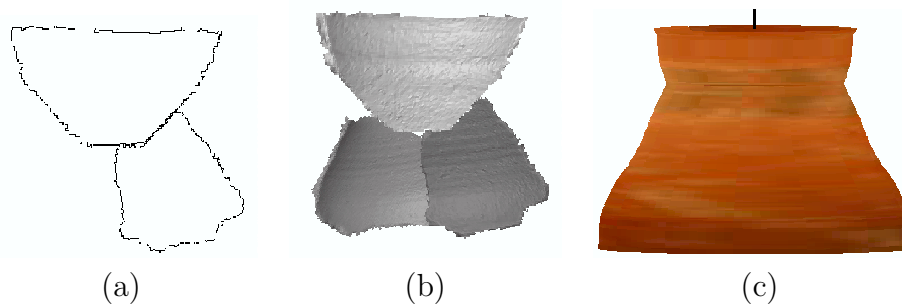


Figure 6.19: Archaeological rim fragments: (a) Matching outlines, (b) Matching parts, (c) Reconstruction out of the matched profile sections.

The results demonstrate the possibility of automatically matching adjacent fragments by our method. It works for fragments which can be orientated and classified by our approach with one exception: two adjacent fragments on top of each other cannot be matched by our method, because they do not have overlapping profile sections. Furthermore if the surface of the fragment is too flat or too small (see Section 3.1.1) or the classification is not known, the fragment is not considered for reconstruction.

6.4 Archaeological Point of View

In order to evaluate the relevance of the results to archaeology Kristina Adler, who is an archaeologist and member of our interdisciplinary project *Computer Aided Classification of Ceramics* (see Section 1.3) comments this thesis from an archaeological point of view:

“This thesis describes the automated documentation of archaeological pottery. It describes a complete system from data acquisition of pottery until the final drawing of a fragment. The referenced problems of the documentation of archaeological pottery are well known within archaeology.

This thesis represents a valuable contribution to decrease the amount of work necessary for the archival of pottery found on archaeological excavations. As an archaeologist, I identify the automatic and therefore objec-

tive generation of profiles and the implicit finding of the correct orientation of fragments as a major improvement with respect to archaeological documentation. Rather than having access to virtual reconstructions of pottery, speeding up the documentation process is of greatest importance for every ongoing excavation. The proposed solution for automatic classification is based on classification rules developed from archaeologists [2], which is not only of crucial importance for the correctness of the results, but also supports the acceptance of a new tool for archaeology. The final reconstructions and 3D models allow new perspectives to save Cultural Heritage such as those integrated in virtual museums. Fast access to the archived data may widen the scope of archaeological research.

The author exchanged and cross-checked his ideas on the topic with the associated archaeological community, which is expressed in a number of publications in conferences on Computer and Archaeology in recent years.

New technologies applied to archaeology often raise the problem of funding and are simply not affordable for archaeological research groups. Consequently I do hope that the very promising tool described in this thesis will be finally developed by a company and can prove its applicability on a wide range of excavations.”

Mag^a. Kristina Adler, City of Vienna, Department of Urban Archaeology.

6.5 Chapter Summary

In this chapter we showed results on the assembly of an object from pieces, which in our case means the reconstruction of a pot from its fragments, but also the reconstruction of a pot out of its profile section. First we showed results on the reconstruction of profiles. Then we presented results and experiments for the reconstruction of fragments out of their profiles. The outcome on vessel reconstruction out of multiple fragments was described by synthetic and real 3D data. Finally an archaeologist gave a statement on the results from her point of view.

Chapter 7

Conclusion and Outlook

In this thesis we have presented a complete archaeological data system that begins with scanning both the geometry and color of pottery fragments, and addresses the processing and classification of the acquired data in order to finally reconstruct the fragments into complete vessels. In this concluding chapter the feasibility of the methods presented is discussed (Section 7.1). Furthermore, the contributions of the thesis are summarized in Section 7.2 and an outlook on future work is given in Section 7.3.

7.1 Feasibility of the Approach

To meet the needs of archaeologists an automated fragment reconstruction system should include facilities for image acquisition and segmentation, visualization, and user interaction [91]. In order to discuss the feasibility of the complete pottery documentation and reconstruction system presented every phase of the approach needs to be examined.

For recording of pottery on site, a handheld device was presented. The quality in terms of usability of the acquired data depends on the experience of the user, consequently potential users have to be trained:

- Knowledge of the scanning equipment (features of the camera, placement of the object, lighting conditions, etc.).
- Knowledge of the objects to be scanned: which parts of the object are essential? Important parts (e.g. rim, texture, curvature, etc.) should

be recorded and therefore have to be known a priori.

- Knowledge of the scanning process: how to handle occlusions, reflections, etc.

From a practical point of view the acquisition task consists of various tasks like setting up the acquisition equipment, selecting the material, finding optimal lighting conditions and acquiring the data. In our approach it therefore represents the most time consuming part of the whole reconstruction process.

The processing of the acquired data is limited by symmetry constraints, i.e. if the surface of the fragment is too flat or too small. Similar to the manual documentation process, these fragments are preselected by the system and excluded from further processing (see Section 3.4 for a comparison of manual and automated processing).

Our reconstruction approach depends on the classification of qualitative features of the fragments and uses methods to explicitly define the structure of the final, complete object, which must be known a priori. The classification algorithm is not general and is applicable only to specific types of archaeological fragments that have to be labeled and categorized beforehand. From the reconstruction point of view, our approach lacks on general applicability, but from a practical or archaeological point of view, our approach leads to an automatic reconstruction and documentation system. Archaeologists benefit from a decrease in the amount of work needed for archival, and from having access to virtual reconstructions of pottery [2].

The system proposed does not yet provide a user interface, except for acquisition and processing. Our system will be integrated into the 3D-MURALE environment, for which a user interface will be developed [108]. Human intervention is not required but can clarify the final reconstruction result by interactively imposing restrictions on the final combinations of objects. Due to the deteriorated state of most archaeological finds, an automated procedure cannot always replace archaeological expertise. The methods proposed -with the exception of classification- are not limited to archaeological finds, as they do not rely on specific archaeological information and can therefore be applied in other 3D acquisition and modeling applications.

7.2 Thesis Summary

In this thesis, we have presented a solution for automatic documentation of archaeological pottery, which constructs a complete model of a vessel out of multiple fragments. After describing the archaeological background and stating the problem in the introduction (Chapter 1), 3D data acquisition with respect to archaeological requirements was demonstrated (Chapter 2).

We identified four different acquisition techniques, developed for the recording of profile sections, pottery fragments, complete vessels and color.

Chapter 3 addressed the processing of the recorded fragment data in order to compute their profile sections. First the orientation of the fragment was estimated by computing the axis of rotation. Based on the computed axis a model based registration technique was performed. Then the profile section was estimated which served as a basis for the documentation and subsequent classification.

The classification process described in Chapter 4 tries to find different fragments belonging to the same vessel. We determined shape characteristics by segmenting the profile section. A curvature based segmentation method based on B-splines was chosen. In order to generate primitives we applied a classification scheme on the basis of absolute measurements and ratios.

In Chapter 5 the reconstruction of a virtual vessel out of fragments was described. We proposed a description language in order to compute the confidence between two fragments. The matching between two candidate fragments is estimated by a two-degrees-of-freedom approach.

The applicability of the concept was demonstrated by various experiments described at the end of each chapter. The pottery dataset used for the experiments contained 70 fragments.

7.3 Future Work

In this work all necessary steps for automated reconstruction of archaeological pottery have been presented. Future work will be directed towards decreasing the limits and restrictions described in Section 7.1, and towards extending the scope of the algorithms presented so that they can be applied to other

fields of research (e.g. art restoration, failure analysis, handwritten numeral recognition, object recognition using shape context, ...).

In particular we will integrate our pottery tool into the 3D-MURALE system, which will then be linked to a user interface and a database. In order to set up a 3D pottery database with more than 1000 fragments, further recording of fragments is planned. We intend to use pottery from one excavation in order to test all steps of the reconstruction with the same pottery ware.

Another interesting challenge would be to combine the methods proposed with other, like the one listed in the introduction section, in order to investigate the possibility of a reliable and fully automated object reconstruction procedure.

Bibliography

- [1] W.Y. Adams and E.W. Adams. *Archaeological Typology and Practical Reality. A Dialectical Approach to Artifact Classification and Sorting*. Cambridge, 1991.
- [2] K. Adler, M. Kampel, R. Kastler, M. Penz, R. Sablatnig, and K. Hlavackova-Schindler. Computer Aided Classification of Ceramics - Achievements and Problems. In W. Börner and L. Dollhofer, editors, *Proc. of 6th Intl. Workshop on Archaeology and Computers*, pages 3–12, Vienna, Austria, 2001.
- [3] F.M. Andraschko, A. Krekeler, and N. Schliep-Andraschko. Terminologie, Klassifikation und computergestützte Bearbeitung der Keramik des 1. Jahrtausends v. Chr. vom Westkom auf Elephantine, Oberägypten. In W.R. Teegen F.M. Andraschko, editor, *Gedenkschrift für Jürgen Driehaus*, pages 327–338, 1990.
- [4] D.H. Ballard and C.M Brown. *Computer Vision*. Prentice Hall, 1982.
- [5] R. Baribeau, L. Godin, L. Cournoyer, and M. Rioux. Color three-dimensional modeling of museum objects. In *British Museum Occasional Papers, Imaging the past*, number 14 in 1, pages 199–209, 1996.
- [6] J.R. Bennett and J.S. MacDonald. On the Measurement of Curvature in a Quantized Environment. *IEEE Transactions on Computers*, 24:803–820, 1975.
- [7] J.A. Beraldin, F. Blais, M. Rioux, and L. Cournoyer. Portable digital 3D imaging system for remote sites. In *Proceedings of the IEEE Inter-*

national Symposium on Circuits and Systems (ISCAS '98) Conference, pages 488–493, Monterey, CA, May 31–June 3 1998.

- [8] J.A. Beraldin, C. Atzeni C., G. Guidi, M. Pieraccini, and S. Lazzari S. Establishing a Digital 3d Imaging Laboratory for Heritage Applications: First Trials. In *Proceedings of the Italy-Canada 2001 Workshop on 3D Digital Imaging and Modeling Applications*, Padova, 2001. on CD-ROM.
- [9] R. Bernbeck. *Theorien in der Archäologie*. Tübingen and Basel, 1997.
- [10] P.J. Besl. Active, optical range imaging sensors. *Machine Vision and Applications*, 1(2):127–152, 1988.
- [11] L.R. Binford. Archaeological Systematics and the Study of Cultural Process. *American Antiquity*, 31:203–210, 1965.
- [12] F. Blais. A Review of 20 Years of Range Sensor Development. In *SPIE Proceedings, Electronic Imaging*, volume 5013, pages 62–76, 2003.
- [13] G. C. Burdea and H. J. Wolfson. Solving Jigsaw Puzzles by a Robot. *IEEE Transactions on Robotics and Automation*, 5(5):752–764, 1989.
- [14] D. Cooper, A. Willis, Y. Cao, D. Han, F. Leymarie, F., X. Orriols, and D. Mumford. Assembling Virtual Pots from 3D Measurements of their Fragments. In D. Arnold, editor, *Proceedings of the International Symposium on Virtual Reality, Archaeology and Cultural Heritage, Athens*, pages 241–253, 2001.
- [15] J. Cosmas, T. Itagaki, D. Green, E. Grabczewski, L. Van Gool, A. Zalesny, D. Vanrintel, F. Leberl, M. Grabner, K. Schindler, K. Karner, M. Gervautz, S. Hynst, M. Walkens, M. Pollefeys, R. DeGeest, R. Sablatnig, and M. Kampel. 3D MURALE: A Multimedia System for Archaeology. In *Proc. of Intl. EuroConference on Virtual Reality, Archaeology and Cultural Heritage*, pages 297–305, Athens, Greece, Nov. 28–30 2001.

- [16] W. Czysz and W. Endres. *Archäologie und Geschichte der Keramik in Schwaben*. Neusädt, 1991.
- [17] A.M. Darwish and A.K. Jain. A Rule-based Approach for Visual Pattern Inspection. *IEEE Transactions Pattern Analysis and Machine Intelligence*, 10(1):56–58, 1988.
- [18] C. de Boor. *A Practical Guide to Splines*. Springer Verlag, 1978.
- [19] R. Degeest. The Common Wares of Sagalassos. In M. Walkens, editor, *Studies in Eastern Mediterranean Archaeology*, III, 2000.
- [20] F.W. DePiero and M.M. Trivedi. 3D Computer Vision using Structured Light: Design, Calibration, and Implementation Issues. *Advances in Computers*, 43, 1996.
- [21] R. DeVore and G. Lorentz. *Constructive Approximation*. Springer, 1993.
- [22] C. Dorai, G. Wang, A.K. Jain, and C. Mercer. Registration and Integration of Multiple Object Views for 3D Model Construction. *IEEE Transactions Pattern Analysis and Machine Intelligence*, 20(1):83–89, January 1998.
- [23] M.K.H. Eggert. *Prähistorische Archäologie. Konzepte und Methode*. Tübingen and Basel, 2001.
- [24] S. F. El-Hakim, J. A. Beraldin, and M. Picard. Detailed 3D Reconstruction of Monuments using multiple Techniques. In W. Boehler, editor, *Proceedings of ISPRS-CIPA Workshop on Scanning for Cultural Heritage Recording*, pages 13–18, Corfu, 2002.
- [25] W. Erdmann, H.J. Kühn, and H. Lüdtkke. *Rahmenterminologie zur mittelalterlichen Keramik*, 1984.
- [26] D. Copper et al. Bayesian pot-assembly from fragments as problems in perceptual-grouping and geometric-learning. In R. Kasturi, D. Laurendeau, and C. Suen, editors, *Proc. of 16th International Conference*

- on *Pattern Recognition, Quebec City*, volume 1, pages 297–302. IEEE Computer Society, 2002.
- [27] F. Leymarie et al. The shape lab. - New Technology and Software for Archaeologist. In Archaeopress, editor, *Computing Archaeology for Understanding the Past (CAA 2000)*, BAR International Series 931, pages 79–89, Oxford, UK, 2000.
- [28] M. Levoy et al. The Digital Michelangelo Project: 3D Scanning of Large Statues. In *Proceedings of SIGGRAPH*, New Orleans, 2000.
- [29] K.S. Fu. Syntactic Pattern Recognition. In T.Y. Young and K.S. Fu, editors, *Handbook of Pattern Recognition and Image Processing*, pages 84–117. Academic Press, 1986.
- [30] V. Gassner. Zur Entstehung des Typus der ionisch- massiliotischen Amphoren. *Fremde Zeiten. Festschrift für Jürgen Borchhardt*, pages 165–176, 199.
- [31] I. Gathmann. ARCOS, ein Gerät zur automatischen bildhaften Erfassung der Form von Keramik. *FhG - Berichte*, 1(2):30–33, 1984.
- [32] M. Gruber and E. Schindler-Kaudelka. Stempelidentifikation norditalienischer Modelkeramik mit photogrammetrischen Methoden. In H. Vettters and G. Picottini, editors, *Die Ausgrabungen am Magdalensberg 1975-1979*, pages 451–455, Klagenfurt, 1996.
- [33] M. Grünewald. Ausgrabungen im Legionslager von Carnuntum (Grabungen 1969-1977). *Der römische Limes in Österreich*, 34:10–11, 1986.
- [34] M.B. Hagstrum and J.A. Hildebrand. The two-curve Method for Reconstructing Ceramic Morphology. *American Antiquity*, 55(2):388–403, 1990.
- [35] R. Halíř. Estimation of Rotation of Fragments of Archaeological Pottery. In W. Burger and M. Burge, editors, *Proc. of the 21st Workshop of the Austrian Association for Pattern Recognition (ÖAGM)*, pages 175–184, Hallstatt, Austria, May 1997.

- [36] N.S. Hall and S. Laffin. A Computer Aided Design Technique for Pottery Profiles. In S. Laffin, editor, *Computer Applications in Archaeology*, pages 178–188. Computer Center, University of Birmingham, Birmingham, 1984.
- [37] R. M. Haralick and L. G. Shapiro. Glossary of Computer Vision Terms. *Pattern Recognition*, 24(1):69–93, 1991.
- [38] J. W. Hayes. Recent Work on Roman Imported and Local Pottery from the Athenian Agora and the Isthmian Sanctuary. In *Hellenistische und kaiserzeitliche Keramik des östlichen Mittelmeergebietes, Kolloquium Frankfurt*, pages 7–17, 1995.
- [39] M. Hoffelder, K. Sauer, and J.K. Rigby. A Hough Transform Technique for Detection of Rotationally Invariant Surface Features. In *2nd. International Conference on Image Processing, Washington DC*, pages 944–948, 1994.
- [40] K. Hori, M. Imai, and T. Ogasawara. Joint Detection for Potsherds of Broken Earthenware. In *IEEE Computer Society Conference on Computer Vision and Pattern Recognition (CVPR '99)*, volume 2, pages 440–445, June 1999.
- [41] Z. Hu and S.D. Ma. The Three Conditions of a Good Line Parameterization. *Pattern Recognition Letters*, 16:385–388, 1995.
- [42] P.J. Huber. *Robust Statistics*. Wiley, New York, 1981.
- [43] J. Trimble and M. Levoy. Stanford digital forma urbis romae project. <http://formaurbis.stanford.edu/docs/FURproject.html>, 2002.
- [44] M. Kampel. Tiefendatenregistrierung von rotationssymmetrischen Objekten. Master's thesis, Technical University of Vienna, Austria, 1999.
- [45] M. Kampel and C. Liska. Zwei computerunterstützte Methoden zur bildhaften Erfassung archäologischer Fundstück. *Forum Archaeologia*, III(6), 1998. <http://farch.net>.

- [46] M. Kampel, C. Liska, and S. Tosovic. Adaptive 3D Reconstruction of Archaeological Pottery. In *Proc. of IS&T/SPIE Symposium on Machine Vision Applications in Industrial Inspection IX*, volume 4301, pages 42–51, San Jose, CA, 2001. SPIE.
- [47] M. Kampel and R. Sablatnig. A Model-based Approach to Range Image Registration. In Markus Vincze, editor, *Robust Vision for Industrial Applications 1999, Proc. of the 23rd Workshop of the Austrian Association for Pattern Recognition (ÖAGM)*, volume 128 of *OCG Schriftenreihe*, pages 109–117. Oldenbourg Wien, München, 1999.
- [48] M. Kampel and R. Sablatnig. On 3D Modelling of Archaeological Sherds. In N. Sarris and M.G. Strinzis, editors, *Proc. of Intl. Workshop on Synthetic-Natural Hybrid Coding and Three Dimensional Imaging*, pages 95–98, Santorini, Greece, 1999.
- [49] M. Kampel and R. Sablatnig. Color Classification of Archaeological Fragments. In A. Sanfeliu, J.J. Villanueva, M. Vanrell, R. Alquezar, A.K. Jain, and J. Kittler, editors, *Proc. of 15th International Conference on Pattern Recognition, Barcelona*, volume 4, pages 771–774. IEEE Computer Society, 2000.
- [50] M. Kampel and R. Sablatnig. Color Classification of Ceramics using Spectral Reflectance. In *First International Conference on Color in Graphics and Image Processing*, pages 323–327, Saint-Etienne, France, October 2000.
- [51] M. Kampel and R. Sablatnig. Automated 3D Recording of Archaeological Pottery. In D. Bearman and F. Garzott, editors, *Proceedings of the International Conference on Cultural Heritage and Technologies in the Third Millennium, Milan*, volume 1, pages 169–182, 2001.
- [52] M. Kampel and R. Sablatnig. Automated Segmentation of Archaeological Profiles for Classification. In R. Kasturi, D. Laurendeau, and C. Suen, editors, *Proc. of 16th International Conference on Pattern Recognition, Quebec City*, volume 1, pages 57–60. IEEE Computer Society, 2002.

- [53] M. Kampel and R. Sablatnig. Automated Archivation System of Pottery. In T. Wittig, editor, *Amman Cultural Heritage Conference, Multimedia for Cultural Heritage*, pages 39–43, 2002.
- [54] M. Kampel and R. Sablatnig. Computer aided classification of ceramics. In F. Niccolucci, editor, *Virtual Archaeology, Proceedings of the VAST2000 Euroconference, Arezzo*, pages 77–82, Oxford, 2002. Archaeopress.
- [55] M. Kampel and R. Sablatnig. An automated pottery archival and reconstruction system. *Journal of Visualization and Computer Animation*, 14, 2003. in press.
- [56] M. Kampel, R. Sablatnig, and H. Mara. Automated documentation system of pottery. In N. Magnenat-Thalmann and J.H. Rindel, editors, *Proc. of 1st International Workshop On 3D Virtual Heritage, Geneva, Switzerland*, pages 14–20, 2002.
- [57] M. Kampel, R. Sablatnig, and H. Mara. Profile Segmentation Scheme for Automated Classification of Archaeological Sherds. In *Proc. of CAA2002: Computer Applications and Quantitative Methods in Archaeology Conference: The Digital Heritage of Archaeology, Heraklion*, page in press, 2002.
- [58] M. Kampel, R. Sablatnig, and S. Tosovic. Volume based reconstruction of archaeological artifacts. In W. Boehler, editor, *Proc. of Intl. Workshop on Scanning for Cultural Heritage Recording*, pages 76–83, 2002.
- [59] M. Kampel and S. Tosovic. Turntable calibration for automatic 3D-reconstruction. In *Applications of 3D-Imaging and Graph-based Modelling, Proceedings of the 24th Workshop of the Austrian Association for Pattern Recognition (ÖAGM)*, pages 25–31, 2000.
- [60] M. Kampel, S. Tosovic, and R. Sablatnig. Octree-based fusion of shape from silhouette and shape from structured light. In G.M. Cortelazzo and C. Guerra, editors, *Proc. of 1st IEEE Intl. Symposium on 3D*

- Data Processing Visualization and Transmission, Padova*, pages 754–757, 2002.
- [61] U. Kampffmeyer. *Untersuchungen zur rechnergestützten Klassifikation der Form von Keramik. Arbeiten zur Urgeschichte des Menschen, 11*. Frankfurt am Main, 1987.
- [62] Y. Kanazawa and K. Kanatant. Reliability of Fitting a Plane to Data. *Transaction on Informations and Systems*, E78-D(12), 1995.
- [63] M. Kandler, F. Schloegelhofer, J. Tschannerl, and P. Waldhaeusl. Die photogrammetrische Dokumentation von Ziegelstempeln. In M. Kandler, editor, *Lebendige Altertumswissenschaft: Festgabe zur Vollendung des 70. Lebensjahres von Hermann Vetters dargebracht von Freunden, Schülern und Kollegen*, pages 428–430, Wien, 1985.
- [64] M. Kanoh¹, S. Kato, and H. Itoh. Earthenware reconstruction based on the shape similarity among potsherds. *Society for Science on Form*, 16(1):77–90, 2001.
- [65] P.M. Kenrick. *Rim-forms of some Relief-decorated Vessels in Italian Terra Sigillata*. *Conspectus formarum terrae sigillatae italico modo confectae*. Bonn, 1990.
- [66] R. Klette, A. Koschan, and K. Schlüns. *Computer Vision - Räumliche Information aus digitalen Bildern*. Vieweg, 1996.
- [67] W. Kong and B.B. Kimia. On solving 2D and 3D puzzles using curve matching. In *IEEE Computer Society Conference on Computer Vision and Pattern Recognition (CVPR '01)*, volume 2, pages 583–590, 2001.
- [68] D.A. Kosiba, P. M. Devaux, S. Balasubramanian, T.L. Gandhi, and R. Kasturi. An Automatic Jigsaw Puzzle Solver. In *Proc. of the 12th IAPR International Conference on Pattern Recognition, Jerusalem*, volume 1, pages 616–618. IEEE-Computer Society Press, 1994.
- [69] K.N. Kutulakos and S.M. Seitz. A theory of shape by space carving. *International Journal of Computer Vision*, 38(3):197–216, July 2000.

- [70] Langenscheidt. *Langenscheidts Fremdwörterbuch*. Friedhelm Hübner, 1989.
- [71] R. L. Lee. Colorimetric calibration of a Video Digitizing System. *Colour Research and Application*, 13(3):180–186, 1988.
- [72] H. C. G. Leitão. *Reconstrução Automática de Objetos Fragmentados*. PhD thesis, Inst. of Computing, Univ. of Campinas, 1999.
- [73] H. C. G. Leitão and J. Stolfi. A Multiscale Method for the Reassembly of Two-Dimensional Fragmented Objects. *IEEE Trans. on Pattern Analysis and Machine Intelligence*, 24(9):1239–1251, 2002.
- [74] C. Liska. Das Adaptive Lichtschnittverfahren zur Oberflächenkonstruktion mittels Laserlicht. Master’s thesis, Vienna University of Technology, Institute of Computer Aided Automation, Pattern Recognition and Image Processing Group, Vienna, Austria, April 1999.
- [75] U. Lübbert and U. Kampffmeyer. Forschungsprojekt ARCOS: Ein Rechner und Programmsystem für die Archäologie. *Archäologie in Deutschland*, 1(89):36–40, 1989.
- [76] M. M. Greenspan and G. Godin. A Nearest Neighbor Method for Efficient ICP. In *Proc. of the 3rd IEEE Intl. Conference on 3-D Digital Imaging and Modeling, Quebec*, pages 161–168, 2001.
- [77] P.L. Main. Accessing Outline Shape Information Efficiently within a large Database. In S. Laflin, editor, *Computer Applications in Archaeology*, pages 73–82. Computer Centre, University of Birmingham, Birmingham, 1986.
- [78] L. T. Maloney and B. A. Wandell. Colour Constancy: A method for recovering surface spectral reflectance. *Journal of the Optical Society of America*, 3(1):29–33, 1986.
- [79] H. Mara, M. Kampel, and R. Sablatnig. Preprocessing of 3D-data for Classification of Archaeological Fragments in an Automated System.

- In F. Leberl and F. Fraundorfer, editors, *Vision with Non-Traditional Sensors, Proc. of the 26th Workshop of the Austrian Association for Pattern Recognition (ÖAGM)*, volume 160 of *Schriftenreihe der OCG*, pages 257–264, 2002.
- [80] F. Marques, , M. Pardis, and R. Morros. Object matching based on partition information. In *IEEE Computer Society International Conference on Image Processing*, volume 2, pages 829–832, 2002.
- [81] D. Marr. *Vision*. Freeman, 1982.
- [82] P. Martinez. Digital Realities and Archaeology: A difficult relationship or a fruitful marriage. In D. Arnold, editor, *Proceedings of the International Symposium on Virtual Reality, Archaeology and Cultural Heritage, Athens*, pages 9–15, 2001.
- [83] J. Matas, Z. Shao, and J.V. Kittler. Estimation of Curvature and Tangent Direction by Median Filtered Differencing. In *8th International Conference on Image Analysis and Processing*, pages 83–88, 1995.
- [84] C. S. McCamy, H. Marcus, and J. G. Davidson. A Colour-Rendition Chart. *Journal of Applied Photographic Engineering*, 2(3):95–99, 1976.
- [85] C. Menard and R. Sablatnig. On finding archaeological fragment assemblies using a bottom-up design. In W. Burger and M. Burge, editors, *Proc. of the 21st Workshop of the Austrian Association for Pattern Recognition (ÖAGM), Hallstatt*, pages 203–208. Oldenbourg Wien, München, 1997.
- [86] C. Menard and I. Tastl. Automated Color Determination for Archaeological Objects. In *Is&T Fourth Color Imaging Conference, Scottsdale*, pages 160–163, 1996.
- [87] C.A. Micchelli, T.J. Rivlin, and S. Winograd. The Optimal Recovery of Smooth Functions. *Numerische Mathematik*, 26:191–200, 1976.
- [88] E. Oja. *Subspace Methods of Pattern Recognition*. John Wiley, 1983.

- [89] C. Orton. *Mathematics in Archaeology*. Wm Collins & Sons & Co, Cambridge, 1980.
- [90] C. Orton, P. Tyers, and A. Vince. *Pottery in archaeology*. Cambridge University Press, Cambridge, 1993.
- [91] G. Papaioannou, E.A. Karabassi, and T. Theoharis. Virtual archaeologist: Assembling the past. *IEEE Computer Graphics*, 21(2):53–59, March-April 2001.
- [92] G. Papaioannou, E.A. Karabassi, and T. Theoharis. Segmentation and Surface Characterization of Arbitrary 3D Meshes for Object Reconstruction and Recognition. In *IEEE Int. Conference on Pattern Recognition*, pages 734–737, September Barcelona, 2000.
- [93] G. Papaioannou, E.A. Karabassi, and T. Theoharis. Automatic Reconstruction of Archaeological Finds- a Graphics Approach. In *Proc. 4th Intern. Conf. in Computer Graphics and Artificial Intelligence*, pages 117–125, May Limoges, 2000.
- [94] H.v. Petrikovits. Taxonomie und Beschreibung römischer Gefäßkeramik. In *Novaesium V. Die römische Keramik aus dem Militärbereich von Novaesium, Limesforschungen 11*, Berlin, 1972.
- [95] J. Poblome. Sagalassos Red Slip Ware. In M. Walkens, editor, *Studies in Eastern Mediterranean Archaeology*, II. Brepols, 1999.
- [96] J. Poblome, J. van den Brandt, B. Michiels, G. Evsever, R. Degeest, and M. Walkens. Manual Drawing versus Automated Recording of Ceramics. In M. Walkens, editor, *Sagalassos IV, Acta Archaeologica Lovaniensia Monographiae 9*, pages 533–538, Leuven, 1997.
- [97] M. Potmesil. Generating octree models of 3D objects from their silhouettes in a sequence of images. *Computer Vision, Graphics, and Image Processing*, 40:1–29, 1987.
- [98] H. Pottmann, S. Leopoldseder, J. Wallner, and M. Peternel. Recognition and reconstruction of special surfaces from point cloud. In *International Archives of the Photogrammetry, Remote Sensing and Spatial*

- Information Sciences*, volume XXXIV of *Commision 3a*, pages 271–276, 2002.
- [99] K. Pulli. *Surface Reconstruction and Display from Range and Color Data*. PhD thesis, University of Washington, 1997.
- [100] K. Pulli. Multiview registration for Large Data Sets. In *Proc. of 2nd Intl. Conf. on 3D Digital Imaging and Modeling, Ottawa*, pages 160–168, 1999.
- [101] P.M. Rice. *Pottery Analysis: A Sourcebook*, 1987.
- [102] M. Rioux, A. Beraldin, G. Godin, F. Blais, and L L. Cournoyer. High resolution digital 3D imaging of large structures. In *SPIE Proceedings, 3D Image Capture*, volume 3023, pages 109–118, San Jose, CA, February 1997.
- [103] P.K Tam R.K Yip, W.C Lam and D.N Leung. A Hough Transform Technique for the Detection of Rotational Symmetry. *Pattern Recognition Letters*, 15(9):919–928, 1994.
- [104] A. Rosenfeld and E. Johnston. Angle detection on digital curves. *IEEE Transactions on Computers*, 22:875–878, 1973.
- [105] A. Rosenfeld and A. Nakamura. Local Deformations of Digital Curves. *Pattern Recognition Letters*, 18(7):613–620, July 1997.
- [106] S. Rusinkiewicz and M. Levoy. Efficient Variants of the ICP Algorithm. In *Proc. of the 3rd IEEE Intl. Conference on 3-D Digital Imaging and Modeling, Quebec*, pages 145–152, 2001.
- [107] R. Sablatnig. *A Highly Adaptable Concept for Visual Inspection*. PhD thesis, Vienna University of Technology, Inst. of Computer Aided Automation, Pattern Recognition and Image Processing Group, 1997.
- [108] R. Sablatnig and M. Kampel. The Virtual Reconstruction of an Archaeological Site - An Overview of the MURALE Project. In B. Likar, editor, *Proc. of 6th Computer Vision Winter Workshop 2000*, pages 60–70, February 2001.

- [109] R. Sablatnig and M. Kampel. Model-based registration of front- and backviews. *Computer Vision and Image Understanding*, 87(1):90–103, Sep. 2002.
- [110] R. Sablatnig and C. Menard. Computer based Acquisition of Archaeological Finds: The First Step towards Automatic Classification. In P. Moscati and S. Mariotti, editors, *Proceedings of the 3rd International Symposium on Computing and Archaeology, Rome*, volume 1, pages 429–446, 1996.
- [111] R. Sablatnig, S. Tosovic, and M. Kampel. Combining shape from silhouette and shape from structured light for volume estimation of archaeological vessels. In R. Kasturi, D. Laurendeau, and C. Suen, editors, *Proc. of 16th International Conference on Pattern Recognition, Quebec City*, volume 1, pages 364–367. IEEE Computer Society, 2002.
- [112] R. Schreg. *Keramik aus Südwestdeutschland. Eine Hilfe zur Beschreibung, Bestimmung und Datierung archäologischer Funde vom Neolithikum bis zur Neuzeit*. Tübingen, 1978.
- [113] A.O. Shepard. *Ceramics for Archaeologists*. Washington (9th reprint 1976), 1956.
- [114] Y. Shirai. *Three-Dimensional Computer Vision*. Springer-Verlag, 1987.
- [115] A. Shoukry and A. Amin. Topological and Statistical Analysis of Line Drawings. *Pattern Recognition Letters*, 1:365–374, 1983.
- [116] J. L. Simonds. Application of characteristic vector analysis to photographic and optical response data. *Journal of the Optical Society of America*, 53:968–974, 1963.
- [117] C.M. Sinopoli. *Approaches to Archaeological Ceramics*. New York, 1991.
- [118] C. Steckner. SAMOS: Dokumentation, Vermessung, Bestimmung und Rekonstruktion von Keramik. *Akten des 13. internationalen Kongresses für klassische Archäologie - Berlin*, pages 631–635, 1988.

- [119] C. Steckner. Das SAMOS Projekt. *Archäologie in Deutschland*, 1(Heft 1):16–21, 1989.
- [120] M. Stricker and A. Leonardis. Exsel++: A general framework to extract parametric models. In V. Hlavac and R. Sara, editors, *Proceedings of the 6th International Conference on Computer Analysis of Images and Patterns, CAIP'95*, pages 90–97, Prague, Czech Republic, September 6-8 1995. IAPR, Springer.
- [121] R. Szeliski. Rapid octree construction from image sequences. *CVGIP: Image Understanding*, 58(1):23–32, July 1993.
- [122] R. Szeliski. Image Mosaicing for Tele-Reality Applications. In *2nd. Workshop on Applications of Computer Vision, Sarasota*, pages 44–53, 1994.
- [123] J. Taylor, G. Forester, F. Livingstone, and R. Baribeau. Amuse: 3D colour imaging, remote access and display. In *Electronic Imaging and the Visual Arts, EVA '96 London Conference Proceedings*, pages 9.1–9.10, 1996.
- [124] S. Tosovic. Adaptive 3D Modeling of Objects by Combining Shape from Silhouette and Shape from Structured Light. Master's thesis, Vienna University of Technology, Institute of Computer Aided Automation, Pattern Recognition and Image Processing Group, Vienna, Austria, February 2002.
- [125] S. Tosovic and R. Sablatnig. 3D modeling of archaeological vessels using shape from silhouette. In *Proc. of the 3rd International Conference on 3D Digital Imaging and Modeling, Quebec City*, pages 51–58, May 2001.
- [126] G. Üçoluk and H. Toroslu. Automatic Reconstruction of Broken 3D surface objects. *Computers and Graphics*, 23(4):573–582, 1999.
- [127] B.C. Vemuri and J.K. Aggarwal. 3D Model Construction from Multiple Views using Range and Intensity Data. In *Proceedings of IEEE Conference on Computer Vision and Pattern Recognition*, pages 435–437, 1986.

- [128] P. Waldhaeusl and K. Kraus. Photogrammetrie für die Archäologie. In Kandler M., editor, *Lebendige Altertumswissenschaft: Festgabe zur Vollendung des 70. Lebensjahres von Hermann Vetters dargebracht von Freunden, Schülern und Kollegen*, pages 423–427, Wien, 1985.
- [129] G. Webster. Romano-British Coarse Pottery: A Students Guide. Technical Report Research Report 6, Council for British Archaeology, 1964.
- [130] J. Williams and M. Bennamoun. A Multiple View 3D Registration Algorithm with Statistical Error Modeling. *IEICE Trans. Inf. and Syst.*, E83-D(8):1662–1670, 2000.
- [131] G. Wyszecki and W.S. Stiles. *Color Science: Concepts and Methods, Quantitative Data and Formula*. John Wiley and Sons, 2nd. edition, 1982.
- [132] L. Xu, E. Oja, and C.Y Suen. Modified Hebian Learning for Curve and Surface Fitting. *Neural Networks*, 5(3):441–457, 1992.
- [133] N. Yokoya and M.D. Levine. Volumetric Descriptions of Solids of Revolution in a Range Image. In *10th. International Conference on Pattern Recognition, Atlantic City, NJ*, pages 303–308, 1990.
- [134] N. Yokoya and M.D. Levine. Volumetric Shapes of Solids of Revolution from a Single-View Range Image. *International Journal of Computer Vision, Graphics and Image Processing*, 59(1):43–52, 1994.

Martin Kampel

Date of Birth: Sept. 02, 1968
Citizenship: Austria
Address: Favoritenstr. 89/10
A-1100 Wien
e-mail: kempel@prip.tuwien.ac.at



Research

Since 1996 he is working at the Pattern Recognition Image Processing Group of the Vienna University of Technology, engaged in research, teaching and administration. His research interests are 3D-Vision, Computer Graphics and Color. He is a member of the IAPR and the IEEE and author and co-author of numerous scientific papers presented at several international conferences and workshops.

Education

M.S. Computer Science: Vienna University of Technology, 1994-1999.

Data Technologies: Vienna University of Technology, 1990-1994.

Erasmus Exchange Program: Rijksuniversiteit te Leiden, The Netherlands, 1994.

AHS (Highschool): AHS Steyr Werndlpark, graduated in 1987.

Visiting positions: Eidgenössische Technische Hochschule Zürich, Feb. 03
Universita degli studi di Pavia, May 01

Institut National des Sciences Appliquées de Lyon, Oct. 00

Budapest University of Technology, May 98

Employment

Vienna University of Technology: Research assistant since 2000 and lecturer (Programming of Image Processing Systems) since 2002.

Independent contractor: IT-Consultant, since 1996.

Austrian Science Fund (FWF): Research assistant, 1996-2000.

Institute for Advanced Studies, Vienna: Scholarship from 1996-1998.